Proceedings of:

Precision Interferometric Metrology

1992 Spring Topical Meeting

April 7-9, 1992

Westward Look Resort

Tucson, Arizona

The American Society for Precision Engineering (ASPE) is a multidisciplinary professional and technical society concerned with research and development, design, manufacture and measurement of high accuracy components and systems. ASPE activities encompass relevant aspects of mechanical, electronic, optical and production engineering, physics, chemistry, and computer and materials science. Membership is open to anyone interested in any aspect of precision engineering.

Founded in 1986, ASPE provides a new focus for a diverse but important community. Other professional organizations have covered aspects of precision engineering, always as a sideline to their principal goals. ASPE is based on the core of generic concepts necessary to achieve precision in any application; independent of discipline, ASPE intends to be the focus for precision technology — and to represent all facets from research to application.

ASPE — The American Society for Precision Engineering
401 Oberlin Road, Suite 108
P.O. Box 10826
Raleigh, NC 27605-0826
Phone (919) 839-8444 Fax (919) 839-8039

Preface

This meeting will cover new developments in interferometric metrology, with emphasis on closing the gap between high resolution and absolute accuracy. Interferometric measurements to nanometer accuracies are crucial to the next generation of precision machine tools, profilers, lithographic systems, and astronomical instruments. Of special importance are techniques to correct for systematic errors in phase measuring interferometer systems, high-accuracy displacement/absolute distance interferometry, and the reduction of limits imposed by atmospheric and environmental disturbances. In addition to the traditional use of HeNe laser sources, the rapid pace of photonics development is creating new opportunities where laser diodes and fiber optics can offer cost and performance advantages in precision metrology.

Topics include: Limits to accuracy, interferometric coordinate metrology for machine motion control, techniques for minimizing environmental effects, phase measuring interferometry for surface figure and finish, photonics in metrology, and techniques for phase measurement and resolution extension.

ISBN 1-887706-07-0

1992 Spring Topical Meeting

Organizing Committee

Co-Chairs:

Norman Bobroff, IBM Thomas J. Watson Research Center
W. Tyler Estler, National Institute of Standards and Technology

Members:

Katherine Creath, University of Arizona
Robert Parks, University of Arizona
Gary Sommargren, Lawrence Livermore National Laboratory

Cooperating Sponsors

Optical Society of America
SPIE (The International Society for Optical Engineering)

1992 Spring Topical Meeting

Contents

Preface — Organizing Committee ii

Contents iii

Program iv

Technical Paper Index 1-2

Technical Papers 5-97

Author Index 99

1992 Spring Topical Meeting

Program

Tuesday, April 7		Wednesday, April 8	Thursday, April 9	Friday, April 10
	7:30	CONTINENTAL BREAKFAST		
	8:30	TECHNICAL	SESSIONS	TECHNICAL VISITS
	10:00			
		BREAK		
	10:30	TECHNICAL	SESSIONS	
	12:00			
		LUNCH		
	1:30	TECHNICAL	SESSIONS	
	3:00			
		BREAK		
ON-SITE REGISTRATION	3:30	TECHNICAL	SESSIONS	
	5:00			
INVITED PAPER	7:00	INVITED PAPER	INVITED PAPER	
BUFFET RECEPTION	8:00	DINNER	DINNER	

Technical Paper Index

Evening Session

Tuesday, April 7, 7:00 p.m.

Invited Paper — Sub-nanometer Metrology for Space-based Stellar Interferometry
M. Shao (Jet Propulsion Laboratory) ..... page 5

Session I
Surface Finish and Texture

Wednesday, April 8, 8:30 - 10:00 a.m.

1. ***Interferometric Metrology of Surface Finish Below 1 Angstrom RMS***
J. A. Meiling (Micromap Corporation) ..... page 7
2. ***Interferometry Combined with a Mechanical Probe, The New Atomic Force Microscopes***
M. R. Rodgers and V. B. Elings (Digital Instruments Inc.) ..... page 11
3. ***Laser Doppler Displacement Meter for Surface Figure and Finish Measurement***
C. P. Wang (Optodyne, Inc.) ..... page 14

Session II
High Resolution Phase Measurement

Wednesday, April 8, 10:30 a.m. - 12:00 p.m.

1. ***Enhancing Fiber Optic Interferometer Precision Using Electro-optic Feedback and Common-mode Compensation***
B. H. Tyrone, Jr. (University of Texas) and A. J. Seltzer and A. B. Buckman (University of Texas and Research Applications, Inc.) ..... page 18
2. ***Direct Optical-to-Electrical Phase Conversion in a Fiber Optic Interferometer***
L. C. Giulianelli and A. B. Buckman (University of Texas and Research Applications, Inc.) ..... page 22
3. ***Homodyne High Resolution Axial Interferometer***
M. Hercher and G. Wyntjes (OPTRA, Inc.) ..... page 27

Session III
New Interferometric Sensors

Wednesday, April 8, 1:30 - 3:00 p.m.

1. ***An Interferometric Sensor for Absolute Position Metrology***
J. D. Blum and C. F. Ferrara (W. J. Schafer Associates) ..... page 31
2. ***Qualification and Performance Analysis of an Interferometric Sensor***
T. A. Sebring, C. F. Ferrara (W. J. Schafer Associates) and D. Youden, M. Gershman (Rank Taylor Hobson) ..... page 35
3. ***A DMI System with Advancements for Measurement and Control of Moving Stages***
A. H. Field (Zygo Corporation) ..... page 40

Session IV
Accuracy Limits of Distance Measuring Interferometry

Wednesday, April 8, 3:30 - 5:00 p.m.

1. ***Invited Paper — Some Contributions to Interferometric Length Measurement with High Resolution and High Accuracy***
G. Wilkening (Physikalisch-Technische Bundesanstalt) ..... page 44
2. ***Sub-Nanometer Metrology for X-ray and Gamma-ray Wavelength Measurements***
E. G. Kessler, Jr. (Nat'l Institute of Standards and Technology) ..... page 49
3. ***Elimination of Polarization Mixing Errors in Single Frequency Distance Measuring Interferometers***
W. Augustyn (CMX Systems, Inc.) and P. Davis (Worcester Polytechnic Institute) ..... page 53

Evening Session
Wednesday, April 8, 7:00 p.m.

Invited Paper — Research on Laser Length Standards in the Precision Engineering Division, NIST
J. A. Stone (Nat'l Institute of Standards and Technology), S. Zushan (Shanghai Institute of Metrological Technology), and A. Stejskal (Institute of Scientific Instruments, Czechoslovakia) ..... page 57

Session V
On-Line Figure Metrology
Thursday, April 9, 8:30 - 10:00 a.m.

1. ***Interferometric Measurement of Rotating Test-pieces***
A. E. Gee (Cranfield Institute of Technology) ..... page 61
2. ***Differential Interferometry for On-Process Aspheric Metrology***
L. C. Maxey (Oak Ridge National Laboratory) ..... page 65

Session VI
Figure Metrology for Optical Systems
Thursday, April 9, 10:30 a.m. - 12:00 p.m.

1. ***Invited Paper — Precision Figure Metrology for Fabrication of the AXAF Mirrors***
D. A. Zweig (Hughes Danbury Optical Systems, Inc.) ..... page 68
2. ***Interferometric Metrology in Optics****
R. P. Grosso and F. Zernike (SVG Lithography Systems, Inc.)
3. ***Environmental Effects of the Testing of Large Astronomical Mirrors***
H. M. Martin, J. H. Burge and S. C. West (University of Arizona) ..... page 72

Session VII
Figure Metrology for Aspheric Optics
Thursday, April 9, 1:30 - 3:00 p.m.

1. ***Status of the NIST Program in Optical Figure Metrology****
C. J. Evans and W. T. Estler (Nat'l Institute of Standards and Technology) and R. E. Parks (University of Arizona)
2. ***Analysis of Cone Error in Off-axis Optics***
R. E. Parks (University of Arizona) and L-Z. Shao (Tucson Optical Research Corp.) ..... page 76
3. ***Testing Cylindrical Surfaces: Alignment Considerations***
K. Creath (University of Arizona) and J. C. Wyant (WYKO Corporation) ..... page 80

Session VIII
Aspheres and Scale Encoders
Thursday, April 9, 3:30 - 5:00 p.m.

1. ***An Interferometer for Aspheric Testing: Calibration and Error Compensation***
S. M. Arnold (APA Optics, Inc.) ..... page 83
2. ***Invited Paper — Aspects of Scale Encoders Based on Grating Interferometer Technology***
A. Teimel (Dr. Johannes Heidenhain GmbH) ..... page 87

Evening Session
Thursday, April 9, 7:00 p.m.

Invited Paper — Precision Measurement of Particle Size Using Bright Field Interferometry
J. S. Batchelder and M. A. Taubenblatt (IBM T. J. Watson Research Center) ..... page 94

*Paper not available at press time.

Technical Papers

Subnanometer Metrology for Space Interferometry

M. Shao

Summary

We are currently developing metrology technology for an Orbiting Stellar Interferometer, (OSI) that is designed to make ultra precise measurements of the angle between stars. To achieve a precision of of 1 microarcsec with a 20 meter baseline interferometer requires the laser metrology to monitor the position of the optics to an accuracy of a few 10's of picometers.

Introduction

OSI is a triple interferometer, three interferometers with colinear baselines, where two of the interferometers look at bright guide stars to obtain attitude information and the third looks a the science targets to measure their position. Laser metrology is used in several places. A laser optical truss is needed to measure the relative positions of the baseline vector with 3D accuracy of ~0.5 nanometers. In other locations the translation of mirror that moves a few meters must be measured with an accuracy of a few 10's of picometers.

We have somewhat arbitrarily divided the metrology of OSI into two catagories, one dimensional and three dimensional metrology. 1D metrology is the measurement of length. Three dimensional metrology is the location in 3D of an optical fiducial such as a corner cube. The types of systematic errors associated with each of these types of metrology are different and the major activity of our work is to eliminate, or calibrate these errors.

One Dimensional Metrology

For mostly historical reasons, we have chosen to use a polarization heterodyne interferometer for length measurements. In the measuring the translation (in the laser beam direction) of a mirror, this type of interferometer has several well known errors. One is the cyclic error due to polarization leakage of imperfect interferometer components. A second is what is often refered to as the cosine error, the fact that the laser beam is not exactly parellel to the direction we wish to measure. The third is due to the fluctuations of the laser wavelength or frequency.

On the ground, the atmosphere severly limits the achievable accuracy of a laser interferometer unless it is in a vacuum. In space the variation of laser wavelength is due to instability of the laser. However, for an astrometric interferometer, the angle between stars is always derived by a ratio of lenghts measured by various interferometer and to first order the laser wavelength is not important if the same laser is used for all the interferometers. However since many of the interferometers are of unequal path (~10m) the laser line width should be moderately narrow if frequency jitter is not to cause fluctuations in the instantaneous length. To keep jitter to 1nm for 10m path, the laser line width should be 10**-10 or 30Khz for a 1um laser.

The cosine error can be quite serious when 10's of picometer accuracy is desired. In OSI the lasers operate at an IR wavelength so that scattered light will not affect the visible light starlight detectors. The stellar interferometer has a star-tracker that keeps the light from the two arms of the interferometer aligned. The IR laser shares the optics with the starlight. Coalignment of the IR laser with the stellar beam is done by feeding the IR light through a single mode fiber and on occasion, pulsing visible light into the fiber and using the star tracker to provide an error signal to co-align the stellar beam and laser beam.

The cyclic error due to imperfect polarization components has been extensively studied. We know of two techniques for reducing this source of error. One is cyclic averaging. In some situations, it is possible to modulate the path being measured by 1 wave. Because the polarization error is cyclic with a wavelength, averaging the data as the path is changed by 1 wave will eliminate the cyclic error. Another technique is to monitor both the amplitude and phase of the heterodyne signal. The phase error occures when an unwanted signal at the heterodyne carrier frequency is added to the correct signal. In addition to changing the phase of the signal, this unwanted signal also changes the amplitude. The cyclic phase error is accompanied by a cyclic amplitude change.

Three Dimensional Metrology

Three dimensional metrology is fundamentally different. The basic approach is to set up a laser interferometer optical truss with retroreflectors at the vertices. If any vertex of the optical truss moves, the laser readings can be converted into x,y,z motion of the vertex element that moves. In order to convert the relative laser measurements into x,y,z one must have a model of the truss geometry, in terms of the angles of the various laser beams. One way to determing the angles of the laser beams is to use absolute metrology. If the absolute lengths of the arms of a triangle are known the angles are also known. The accuracy requirement of the absolute metrology is related to the dynamic range of the motion of the optical truss. Typically, the ratio of the motion of the truss to the size of the truss (eg. 1mm motion of a 10m truss is 10**-4) has to be roughly equal to the ration of the accuracy of the absolute metrology to the accuracy of the relative metrology. In the example above, if the relative metrology is accurate to 100 picometer, the accuracy of the absolute metrology must be ~1um if the error in truss geometry is not to totally dominate the error budget.

Another major source of error at sub-nm levels in 3D metrology comes from the fact that as the vertices of the optical truss move the retroreflectors that is the vertex may rotate. Because the optical surfaces are not accurate at sub-nm levels, the laser beams will show a different path length when different parts of the retroreflectors are interogated by the laser.

The final goal of metrology for OSI is to enable the instrument to measure the angle between two stars ~1 degree apart to 1 micro-arcsec (5 picoradians) and the angle between stars 30 degrees apart with 10 uas accuracy (50 picoradian).

INTERFEROMETRIC METROLOGY OF SURFACE FINISH BELOW 1 ANGSTROM RMS

John A. Meiling
Micromap Corporation
Tucson, AZ, USA

INTRODUCTION

This paper reviews the current status of ongoing work at Micromap Corporation to improve the absolute height accuracy of our phase measurement microscope profiler.

We have observed three systemic errors in measurements of surface finishes near and below 1 Angstrom rms:

Random electronic noise.

Bands parallel to the interference pattern.

Surface shape changing with focus.

Measurements illustrating these errors are shown in Figures 1 through 3. All of the measurements were obtained using a Nikon interference microscope with 2/3" CCD video camera. Interferograms were acquired and averaged by an 8-bit frame grabber with on-board Digital Signal Processor.

ELECTRONIC NOISE

Using a camera with 56dB signal-to-noise, we obtained electronic noise for single measurements of 2 Angstroms rms on reflective samples, and 3 Angstroms rms on uncoated glass. To reduce the measurement noise by averaging, we implemented interferogram and phase averaging on a TMS320C30 Digital Signal Processor. The interferogram averaging time for a measurement of 640x480 data points is 1.2 seconds, significantly faster than performing this operation on a 486 computer. With a practical limitation of 5 to 10 minutes of averaging, we obtain 0.15 Angstroms to 0.4 Angstroms rms electronic noise depending on sample reflectivity and the number of data points in the measurement.

Figure 1 shows random electronic noise (left) and the corresponding surface profile measurements (right) for an average of 4 measurements (top) and 200 measurements (bottom). The electronic noise was measured by taking the difference of two measurements at the same location.

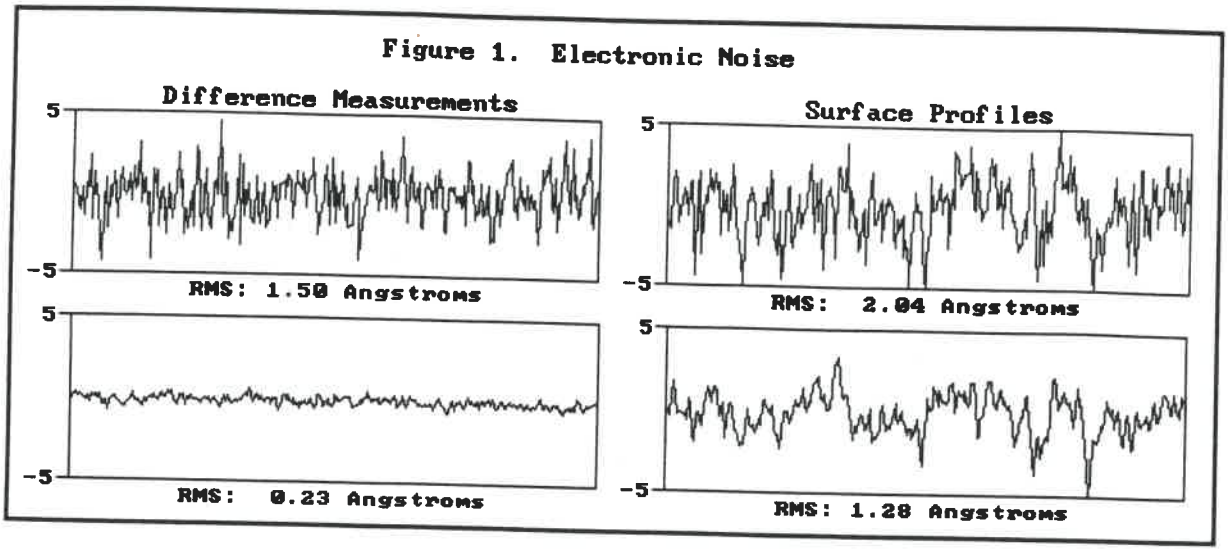

Figure 1. Electronic Noise

BAND ERRORS

Band errors are roughly sinusoidal in profile, and run parallel to the interferogram fringes. The most common band errors have periods 1/2 and 1/4 of the interferogram period, and are sometimes called "2-omega" and "4-omega" errors.

Phase-shift errors cause 2-omega bands. Because most phase measurement instruments use a pzt to step the phase, systemic phase-shift errors are frequently called pzt calibration errors. 2-omega bands also result from the random phase-shift errors caused by vibration or air currents.

Camera detector nonlinearity causes 4-omega bands, and weaker 1-omega and 8-omega bands. We have noted that the 1-omega errors may vary widely for different camera designs.

2-omega and 4-omega errors frequently dominate the measurements of smooth spheres. Figure 3 (left) shows a typical combination of 2-omega and 4-omega errors we observed with the standard 5-frame phase equation[1] before we spent considerable effort to eliminate these errors. By reducing the acquisition time, averaging measurements, and replacing the 5-frame phase equation, we have substantially improved the quality of our measurements (Figure 3, right).

SHAPE ERRORS

We have observed that small changes in tilt and focus alignment affect the measured shape of the sample. Figure 3 illustrates the characteristic change in sample shape measured at 10X (N.A. 0.25) for one fringe change in focus alignment.

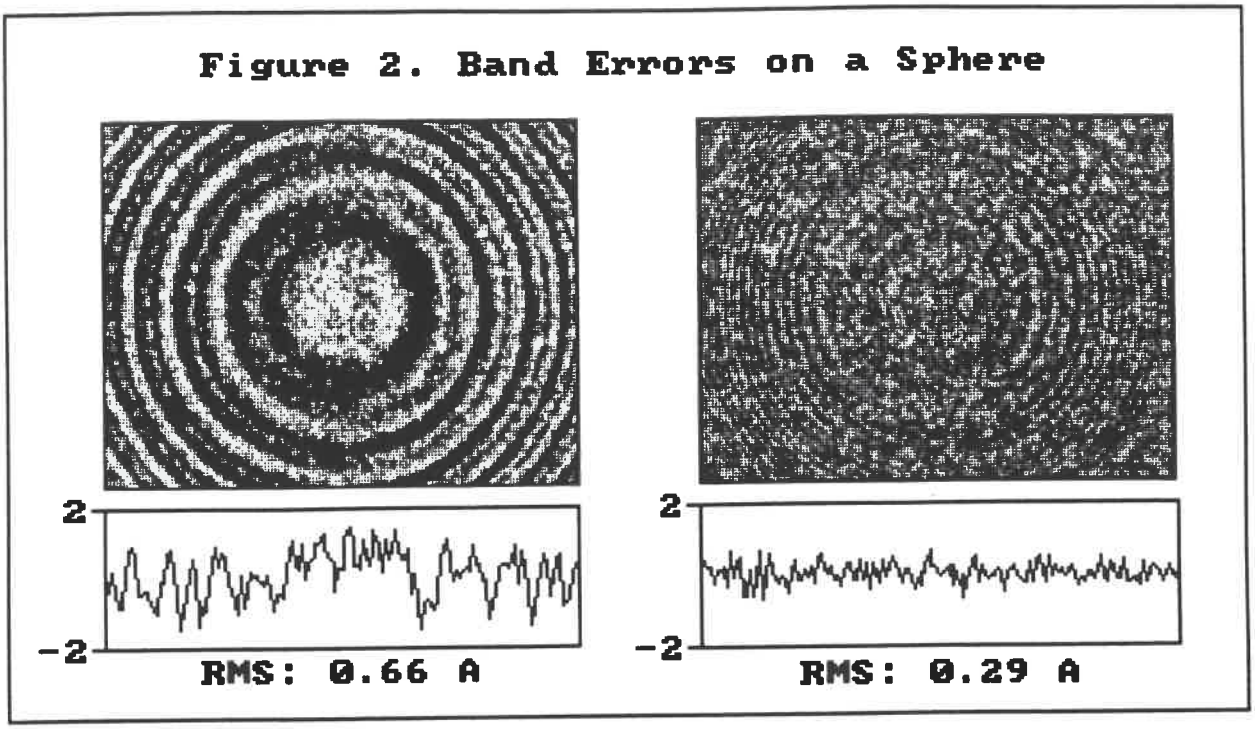

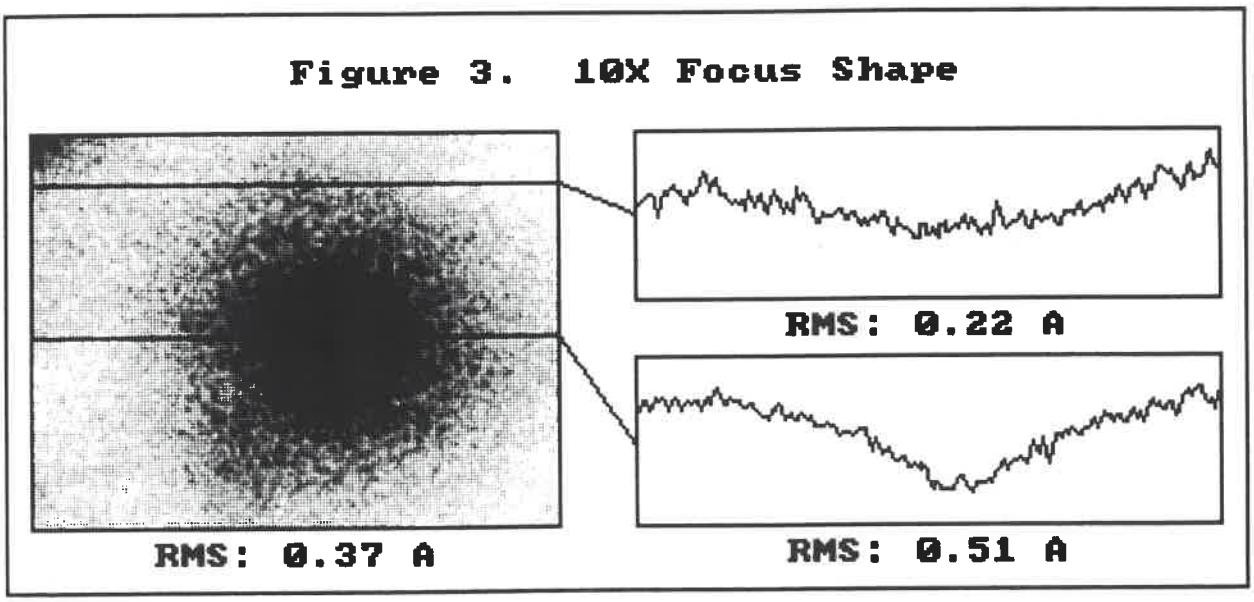

At higher magnifications, the primary shape error for a focus change is 2nd order curvature. A change in the x-tilt alignment induces a focus change proportional to x, so the measured error shape is dominated by a "coma" cubic.

Some shape errors are irregular, and cannot be removed by a least squares fit to a simple polynomial. We make a standard practice of minimizing shape errors by consistent alignment of the sample to the white light interference pattern.

The presence of focus-dependent shape errors complicates the requirement of subtracting an accurate "reference measurement" of the internal reference mirror from the sample measurements to obtain true surface profiles. We have found the usual method of generating a reference on a smooth flat before measuring the sample to be completely useless for measuring surface finishes below 1 Angstrom rms. To produce a reference measurement that accurately reflects the focus alignment of the sample measurements, we have adopted a "self referencing" measurement technique which uses the sample measurements to generate the reference. Take for example a group of 11 measurements having no reference subtracted. Create a "group reference" by summing all of the measurements, and then dividing the sum by 10. A surface profile is calculated by subtracting the group reference from 1.1 times the sample measurement. In this example the rms calculated for each surface profile is about 5% higher than the true profile rms due to the rms of the group reference.

CONCLUSION

Using a self-referencing measurement technique, improved phase calculation, and measurement averaging, we have reduced systemic errors to below 0.2 Angstroms rms on flats, and to 0.2 to 0.4 Angstroms rms on spheres. 1-omega band errors and focus-dependent shape errors can be controlled on flats, but sometimes remain a problem when measuring spheres.

ACKNOWLEDGMENTS

We thank Norm Brown for proposing the self-referencing measurement technique.

REFERENCES

1. P. Hariharan, B. F. Oreb, and T. Eiju, "Digital phase-shifting interferometry: a simple error-compensating phase calculation algorithm," Appl. Opt. **26**, 2504-2505 (1987).

INTERFEROMETRY COMBINED WITH A MECHANICAL PROBE, THE NEW ATOMIC FORCE MICROSCOPES

Mark R. Rodgers
Virgil B. Elings
Digital Instruments, Inc.
6780 Cortona Drive
Santa Barbara, CA 93117
Tel: 805-969-8116
Fax: 805-968-6627

Abstract

Optical Interferometric Metrology has the advantage of extremely high height resolution, but has two major drawbacks. First, the lateral resolution is determined by the dimensions of the diffraction limited spot. In actual practice, this resolution is greater than 100 nanometers, which is too low for many applications. Secondly, an optical interferometer is affected by the optical properties of the sample surface, which can cause distortions in topography measurements.

The lateral resolution limitation is becoming more and more of an issue for several important measurements. For example, we have been asked to measure surface roughness on cleaned and polished bare silicon wafers. The areas we have been asked to observe are as small as one micron square. The major contribution to the roughness over small areas is surface granularity with lateral dimensions of less than 100 nm, and vertical heights of a few angstroms. We have been told that this roughness is significant to gate oxide integrity for small geometry circuit production. Clearly such roughness cannot be measured by optical interferometry. Another class of samples we have been asked to examine are optical elements for x-ray, UV, and high-power applications. Conventional interferometry is not capable of adequately characterizing x-ray or UV optics. For high-power optics, surface irregularities or defects smaller than can be measured with conventional interferometry may provide sites for destructive local heating. Optics and semiconductor wafers are applications where optical interferometry is commonly used, but where its lateral resolution is increasingly inadequate for advanced devices.

The fact that optical interferometers are affected by the optical properties of the surface is the subject of considerable analysis and interpretation. We use interferometric microscopes internally on optically complex surfaces, the results can be quite ambiguous. Yet many optical surfaces are insulators, and must be measured non-destructively as part of relatively large objects. Thus other high resolution techniques such as electron microscopy and scanning probe microscopy have been inappropriate.

Scanning probe microscopy (SPM) addresses both of the drawbacks of optical inteferometry while retaining high height resolution. Up to very recently, however, SPM's have had their own limitations which prevent them from being used for applications that have in the past been the in the domain of interference microscopy. Many surfaces of interest are insulators, which dictate the use of an Atomic Force Microscope (AFM). Existing AFM's are constructed with a height detection system that is sufficiently large that the detection system and probe are generally fixed, and the sample is scanned under the probe. The sample attached to a three axis piezoelectric scanner. Scanners with the required precision and frequency response are not capable of carrying much mass, so AFM's have not had much flexibility in sample configuration. Generally, to achieve good imaging performance, samples have been limited to a few grams, which typically requires that the sample be broken into pieces of small size. Thus although an AFM has lateral and vertical resolution in the angstrom range, and is usually unaffected by optical properties of the scanned surface, for most samples of interest in optics and semiconductor application, breaking the sample has been a requirement to use an AFM.

Very recently new AFM's have been developed which dramatically broaden the range of samples which may be imaged with this scanning probe technology. The new AFM's are a combination of an interferometer and a AFM Probe, configured such that the probe is in contact with the surface and the interferometer measures the deflection of the probe as the surface is scanned. The combination has been miniaturized such that the entire interferometer and probe is very light and may be attached to a scanner, and the height of the unit may be adjusted during scanning to maintain constant probe deflection and therefore achieve ultra-low contact forces. The lateral resolution becomes limited by the size of the probe tip, which may be as small as a few angstroms, and the system is not affected by reflectivity or transmissivity variations of the sample surface. These new AFM's may be used with arbitrarily large samples, eliminating a major limitation of existing AFM's. The new AFM's are particularly useful for semiconductor, storage, and optics applications.

So far the new design AFM has been produced in two forms. One form is a stand-alone device which consists of the scanner, detector, probe and associated electronics packaged together in a unit about the six of a 12 oz. soft drink can. This StandAlone AFM is designed to be placed directly on a sample, or built into a fixture to fit the user's needs. Prototypes have been successfully used for truly novel measurements. One user constructed a fixture to mount the AFM onto a diamond turning machine, and he periodically stops machining and checks the surface finish with nanometer resolution. Another researcher is placing the AFM directly on non-active regions of entire finished sections of the Keck telescope mirror, to measure surface finish. Yet another user has devised a method for holding the AFM in place while microspheres are rotated underneath the probe on an air bearing. Wafers and disk storage media have been measured both with the AFM resting

directly on the sample and suspended over the sample on a fixture. This configuration AFM is relatively inexpensive and extremely versatile.

The new AFM has also been configured in a more complex form that is a legitimate alternative to high-end interference microscopes and has superior measurement performance. The AFM is mounted on a highly rigid bridge structure, suspended over a motorized x-y or R-theta translation stage. Also mounted on the bridge is a high power optical microscope. This system allows the user to view any part of a large (up to 14" diameter) sample either optically or with the AFM, under computer control. Thus areas of interest may be identified visually and then scanned with the AFM at higher resolution, or a sequence of locations may be scanned automatically. Semiconductor wafers, photomasks, storage media, and optical components may be examined non-destructively with unprecedented three dimensional resolution.

The new AFM is an interferometer base measurement system without the disadvantages of interference microscopy. Beyond the resolution and optical interaction issues, scanning probes have other advantages. SPM's generally are straightforward to calibrate and the calibration and accuracy can be specified over a wide range. Other parameters than topography can be measured with variations of AFM's such as surface friction, magnetic field distribution and surface stiffness. Of course, scanning probes have their own inherent disadvantages. Data acquisition times are long compared to optical methods and the probe shape can affect the measurements as well. It is possible to damage a surface with a probe, which is not a consideration with optical systems. However scanning probe microscopy, and in particular the AFM, is well suited for many of the applications currently utilizing interferometry.

The theory and operation of the new AFM's will be presented. A variety of results that are of interest to the interference measurement community will be shown and discussed.

The new interferometer AFM's have been used for applications that are normally in the domain of optical interferometers. Optical components, such as mirrors and lenses, storage media, and semiconductor wafers have been examined for roughness and topography. The operation, accuracy, potential applications, and results for this new use of interferometry will be presented.

Laser Doppler Displacement Meter for Surface Figure and Finish Measurement

Charles P. Wang
Optodyne, Inc.
1180 Mahalo Place
Compton, CA 90220
Tel: 310-635-7481
Fax: 310-635-6301

I) Introduction

A non-contact, high-sensitivity Laser Doppler Displacement Meter (LDDM) is developed for the measurement of surface figure and finish. The displacement resolution is 2.5 nm and the spot size with a focal lens is 10 μm. The surface figure is measured by scanning the surface across the laser beam and the surface profile or roughness data is stored in a computer. The sampling rate can vary from 6250 data/sec up to 800,000 data/sec. The surface roughness can be viewed on the computer monitor or plotted out by a printer. This LDDM can also be applied for vibration measurement in microelectronics, computer disk-drives, precision engineering, automotive and aerospace industries, and research and development laboratories. It can also be used for high accuracy, non-contact, non-intrusive, high-frequency, and complex motion measurement.

II) Theory of Operation and Comparison to LDV Vibrometers

The Laser Doppler Displacement Meter (LDDM) is a precision displacement measurement

instrument based on the principle of Dopplometry[1]. Briefly, when a laser beam is reflected from a moving target, the Doppler frequency shift f_D is

$$f_D = f_L \cdot (2v/c) \tag{1}$$

Where f_L is the laser frequency, c is the speed of light and v is the target velocity parallel to the laser beam. Since frequency is the change of phase Φ with respect to time and velocity is the change of displacement x with respect to time, after one integration, equation 1 becomes:

$$(\Phi/2\pi) = 2(f_L/c) \cdot (x-x_o) \tag{2}$$

where Φ is the phase angle, x is the position and x_o is the initial position. Hence displacement x can be determined by measuring the phase angle Φ. When the phase changes more than 2π, a counter is used to keep track of how many 2π's.

The LDDM has an electro-optical device and phase-demodulator to measure the Doppler phase shift caused by the displacement of the target.

As compared to a Laser Dopplometry Vibrometer (LDV), based on Equation 1, the target velocity can be determined by measuring the frequency shift f_D. Any target with a rough surface or a diffusive reflector will scatter light back with the Doppler shift caused by the target velocity. The electro-magnetic field at the detector is the sum of light scattered by many scatter centers. As shown by Wang[2]:

$$E(t) = \sum_{P=1}^{n} A_P \cdot \exp\{-i2\pi \cdot (f_D + f_L)t + i\Phi_P\} \tag{3}$$

where E(t) is the electro-magnetic field at the detector from n scatter centers, A_P is the amplitude, f_L is the laser frequency, f_D is the Doppler frequency shift and Φ_P is the phase angle. After mixing with a local oscillator on a square law detector, the output spectral density has a term with the Doppler frequency shift, f_D, and certain broadening. Because the light is scattered back, there is Doppler ambiguity[3], which broadens the frequency shift, f_D, and limits the detection to be above a certain minimum velocity of the target. Hence for LDV, the signal-to-noise ratio is low, a long averaging time is needed, and there is a minimum target velocity.

The major features of the LDDM are:

* Non-contact and high-sensitivity
* Absolute displacement, velocity and acceleration
* Large dynamic range and wide bandwidth
* High resolution, high repeatability, high data rate, high optical efficiency and high signal to noise ratio
* No calibration factor, no interference, no minimum velocity, no non-linear effect, and no range switch
* Computer data storage and data processing.

III) Experimental Measurement

A LDDM system was set up for the measurement of a computer hard disk drive. A Lens was used to focus the laser beam to a spot diameter of 10 μm. The disk was rotating at 3600 rpm. The surface profile data at r = 15 mm was collected at 800,000 data/sec, or 150

data/mm. A typical plot of surface roughness is shown in Fig. 1. The peak to peak variation is 40 nm and a typical spatial frequency is about 15 cycles per mm. With a raster scan over the surface, a two-dimensional surface roughness can be obtained.

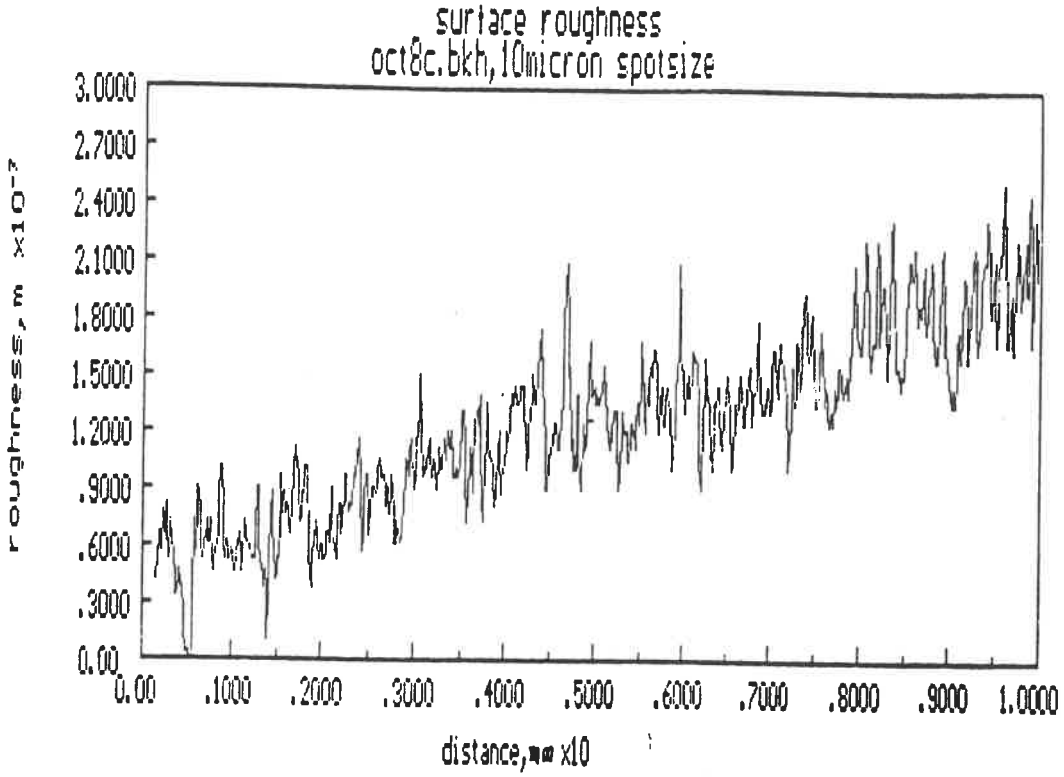

References

1) C. P. Wang,"Laser Doppler Displacement Measurement", Laser and Optronics, 6, p. 69-71, (Sept., 1987).

2) C. P. Wang,"A Unified Analysis on Laser Doppler Velocimeter", J. Phys. E, 5, p. 763, (1972).

3) C. P. Wang,"Effect of Doppler Ambiguity on the Measurement of Turbulence Spectra by Laser Doppler Velocimeter", Appl. Phys. Lett. 22 (4), p. 152, (Feb., 1973).

Enhancing Fiber Optic Interferometer Precision Using Electro-optic Feedback and Common-mode Compensation

B.H. Tyrone, Jr.*, A.J. Seltzer*†, and A.B. Buckman*†
Electrical and Computer Engineering Department - University of Texas*,
and Research Applications, Inc.†, Austin TX.

To achieve wider application, fiber optic interferometers need better supression of environmental perturbations as well as increased measurand sensitivity. In earlier work, we analyzed and demonstrated an enhanced, common-mode compensated fiber interferometer [1-3] with two new features: 1) one additional pair of optical paths to compensate for laser phase noise, spatially uniform temperature variation, and other common-mode environmental fluctuations; and 2) electro-optic feedback (EOF) to enhance sensitivity to small phase shifts in a selected optical path [2,3]. This paper reports a direct experimental comparison of minimum detectable phase shifts for an enhanced and a conventional fiber interferometer operated with the same signal processing electronics and under the same environmental conditions.

For this comparison, we implemented a phase-tracking control system for the enhanced Mach-Zehnder sensor[2] shown schematically in Fig. 1. Couplers C1, C2, and C3 are single-mode evanescent 3dB couplers, while C4 couples only a very small fraction of the power incident in path r to the detector as the control signal, X(t).

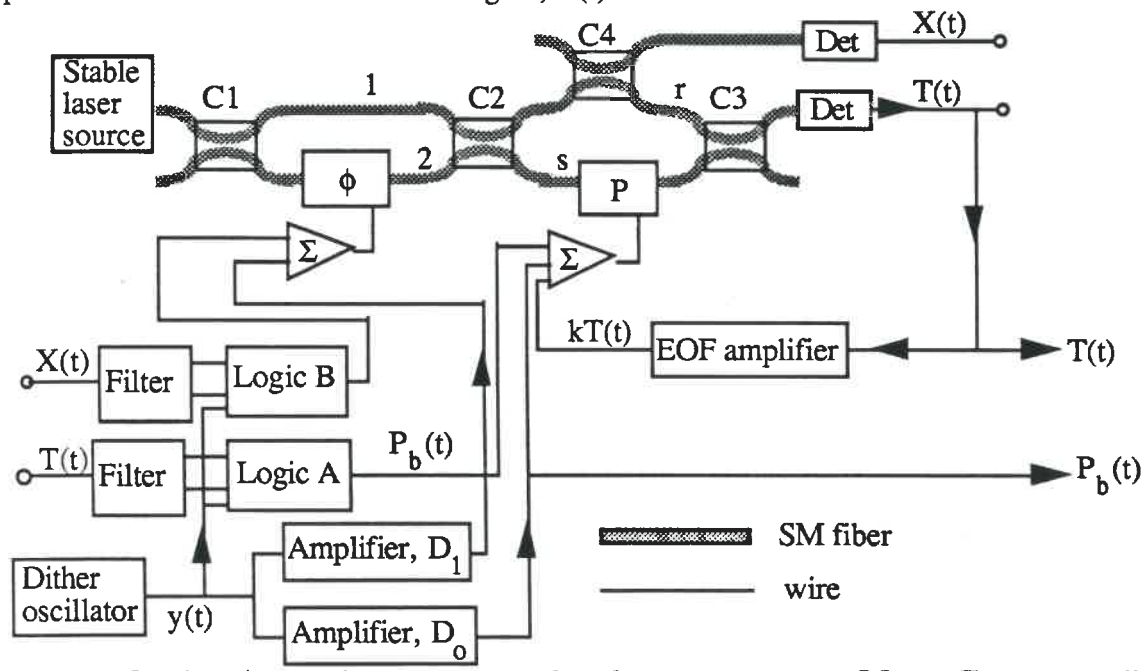

Fig.1. Optical/electrical schematic for enhanced Mach-Zehnder fiberoptic interferometer.

For phase tracking, both phase shifts, ϕ and P, must be controlled at preset values with feedback loops. The system in Fig.1 accomplishes this by applying a "pseudo-common-mode dither" to the interferometer. This dither signal can be generated by modulating the laser wavelength, or as in this experiment, by supplying two small sinusoidal phase shifts of amplitudes D_1 and D_o, at the dither frequency $\omega_d/2\pi$, to the piezos which control ϕ and P. If the ratio of these two amplitudes obeys the relation,

$$\frac{D_0}{D_1} = \frac{L_s - L_r}{L_2 - L_1} \qquad (1)$$

where the L's are the lengths of the designated paths in Fig. 1, then the resulting perturbation affects the transmittance in the same way as a common mode perturbation. Thus, when the phase biases and electro-optic feedback parameter are set for common-mode compensation, the dither component in T(t) vanishes. To set the ratio of amplitudes in (1), only the ratio of the length differences needs to be accurately known. Since the path length differences are of the order mm to cm, this ratio can be determined accurately.

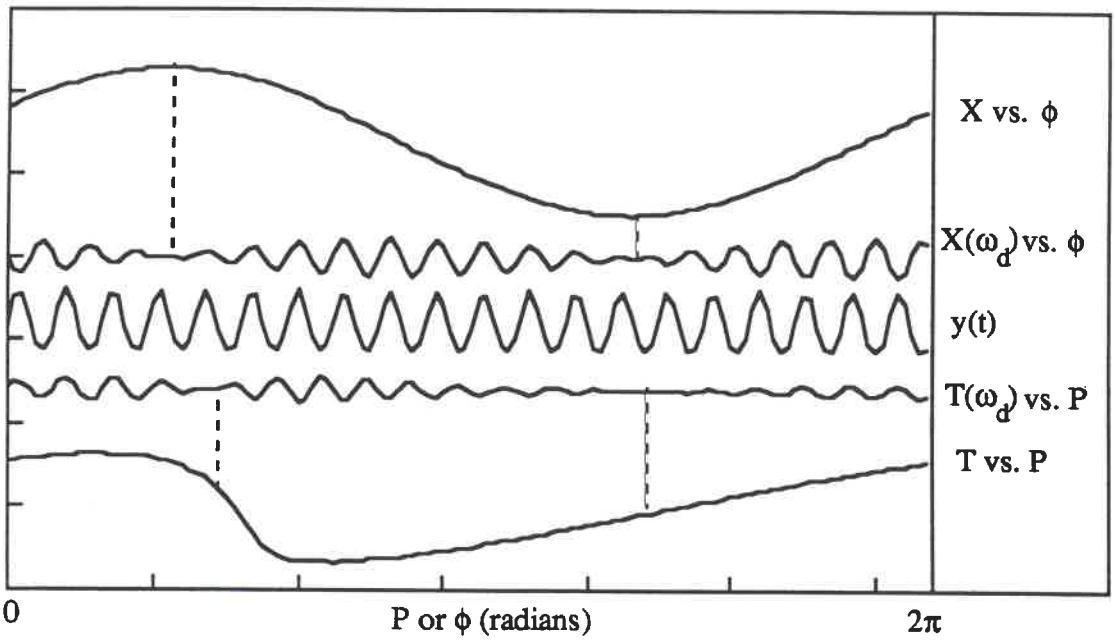

Fig. 2. Signal components from Fig.1 as ϕ or P is swept through 2π over a time corresponding to many oscillations of y(t), for k = 3.

Figure 2 shows a numerical simulation of the quasi-dc and dither frequency components of X(t) and T(t) for k = 3, as ϕ or P is swept through 2π radians in a time corresponding to many oscillations of the dither signal, y(t). The common-mode compensation point in the high-sensitivity region is the point on the T vs. P curve that coincides with the first vanishing of $T(\omega_d)$, at the first vertical dashed line. Logic unit B in Fig.1. controls ϕ by comparing the quasi-dc value of X and the phase of $X(\omega_d)$ to their values at the designed phase bias for ϕ, and applying a correction signal to the ϕ-piezo. The inputs to this logic unit are X and $X(\omega_d)$, filtered from X(t). Logic unit A controls P for phase tracking in a similar manner, using $T(\omega_d)$ and T filtered from T(t).

For this experiment, the time constants in the electronic feedback loops controlling ϕ and P are set much longer than that of the EOF amplifier loop. Under these conditions, slow changes in P appear at the electrical output, $P_b(t)$ at the right of Fig. 1, while more rapid changes appear at the detector output T(t). For comparison purposes, a second experiment with the light input at coupler C2 instead of C1 and the feedback parameter k set to zero in Fig. 1 converts the system into a conventional Mach-Zehnder sensor whose optical path difference is the same as $L_s - L_r$ in the enhanced one.

The system described above was implemented with readily available electronic components, mounted on an unshielded board using wirewrapping. The dither frequency for this system was 10.5 kHz, and a calibration signal equivalent to 125 μradians at 16.5 kHz was applied to path s. The path length differences were 98 mm for L_2 - L_1 and 1 mm for L_s - L_r. A He-Ne laser with stable intensity, but no frequency stabilization, excited the sensor. No extraordinary measures were taken to minimize the environmental or electronic noise, so these results are typical of wire-wrapped, unshielded electronics, with the fiber optics in closed, unevacuated containers, in a laboratory setting.

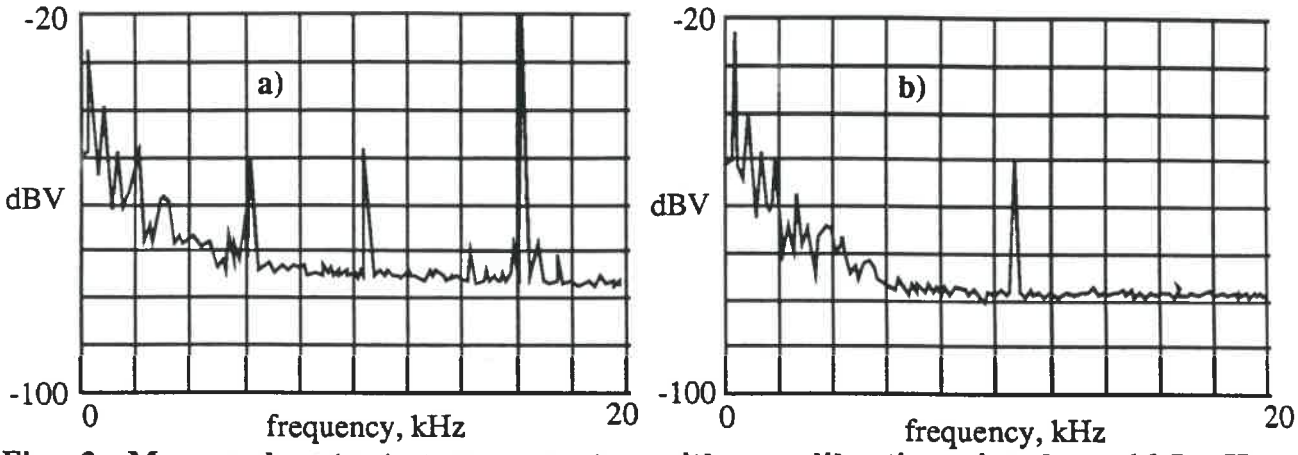

Fig. 3. Measured output power spectra with a calibration signal at 16.5 kHz applied to the phase shifter, P, in Fig. 1: a) enhanced sensor ; b) equivalent conventional interferometer.

The measured power spectrum for the enhanced sensor of Fig. 1 is shown in Figure 3a), indicating the 1/f noise, the oscillations around the preset phase bias, the dither frequency, and the calibration signal. Figure 3a) shows a minimum detectable phase shift of 200 nradians/√Hz, an order of magnitude lower than typical reported results for interferometers with non-zero path differences [4-6]. Figure 3b) shows the measured power spectrum for the equivalent conventional Mach-Zehnder optical circuit which yields a minimum detectable phase shift of 50 μradians/√Hz with the same applied calibration signal used to obtain Fig. 3a).

The enhanced optical circuit lowered the minimum detectable phase shift by a factor of over 100, compared to an *equivalent* conventional interferometer. This result suggests that common-mode compensation combined with electro-optic feedback may be particularly useful for providing high sensitivity under very noisy operating conditions. The minimum detectable phase shift is among the lowest reported, and was achieved without using near-zero path differences[7], frequency-stablized laser sources, or extensive electrical, mechanical or thermal shielding.

This work was supported at the University of Texas by the Texas Advanced Technology Program, and at Research Applications, Inc. by a SBIR contract with the U.S. Naval Sea Systems Command.

References

1. A. B. Buckman, *Analysis of a novel optical fiber interferometer with common-mode compensation*, IEEE J. Lightwave Technol., **7**, 151-157 (1989).

2. A. B. Buckman, D. G. Pritcvhett, and K. Park, *Sensitivity-enhanced, common-mode compensated Mach-Zehnder fiber optic sensor circuit with electro-optic feedback*, Opt. Lett., **14**, 886-888 (1989).

3. A. B. Buckman, *General sensitivity-enhancement and common-mode compensation principle for interferometric fiber-optic sensors,* IEEE J. Lightwave Technol., **8**, 1456-1460 (1990).

4. D. M. Dagenais, F. Bucholtz, K. P. Koo, and A. Dandridge, *Demonstration of 3pT/√Hz at 10 Hz in a fiber-optic magnetometer*, Electron. Lett., **24**, 1422-1423 (1988).

5. K. P. Koo, F. Bucholtz, and A. Dandridge, *Synchronous sampling demodulation scheme for nonlinear fiber-optic sensors*, Opt. Lett., **11**, 683-685 (1986) .

6. D.A. Brown, T. Hofler, S. L. Garrett, *High-sensitivity, fiber-optic, flexural disk hydrophone with reduced acceleration response*, Fiber and Integrated Optics, **8**, 169-191 (1989) .

7. A. Dandridge, *Zero path-length difference in fiber-optic interferometers,* IEEE J. Lightwave Tech., **1**, 514-516 (1982) .

Direct Optical-to-Electrical Phase Conversion in a Fiber Optic Interferometer

Lisa C. Giulianelli*† and A.B. Buckman*
Department of Electrical and Computer Engineering - University of Texas
and Research Applications, Inc.†, Austin TX 78712

In this work, we model and demonstrate an optical circuit modification to the conventional fiber Mach-Zehnder interferometer that maps optical phase shifts into phase shifts in the fundamental and second harmonics of an imposed modulation frequency. The modification of the optical circuit allows simple electronics to obtain these phase shifts, which are shown numerically to be linear, opposite in slope, and in phase quadrature with each other. Many signal-processing schemes for recovering the measurand phase shift information from the interferometer output have been implemented with interferometric fiber optic sensors. In most cases, the desired output is a linear function of phase shift. Phase tracking schemes [1] use a feedback signal to keep the sensor phase-biased in a region where transmittance versus phase is linear. Wavelength modulation of the source provides an output proportional to the time-derivative of the phase shift, which may then be integrated [2]. The synthetic heterodyne approach [3] adds a modulation at ω to the measurand and then electronically mixes the first two harmonics of the output with signals at ω and 2ω to produce a signal at 3ω whose phase shift is the same as the optical phase shift in the interferometer. Our method, Direct Phase, results in a heterodyne signal similar in form to the synthetic heterodyne signal, but the phase shift is obtained directly from the phase of the first and second harmonics of the output, thereby eliminating the electronic mixer. In addition, neither a feedback signal [1] nor an integrator [2] is needed. Thus, the optical modification reduces the complexity of the electronic signal processing in this method .

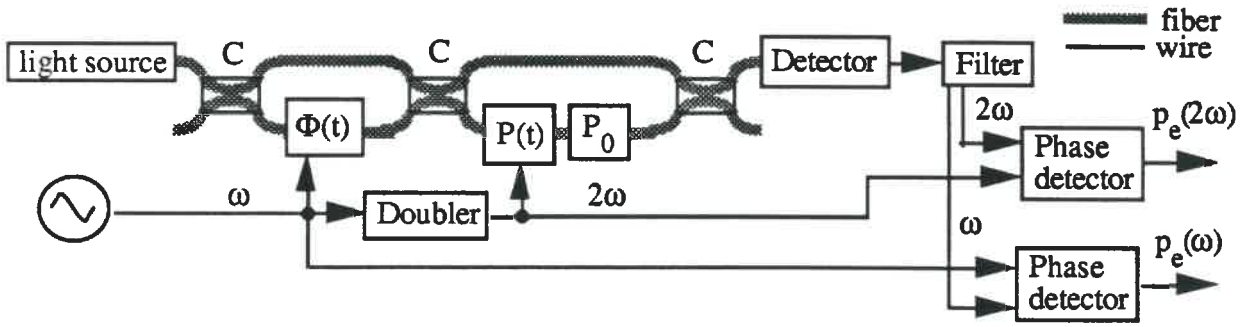

Fig. 1. Optical circuit and signal processing for direct phase conversion. The C are 3dB single-mode evanescent couplers.

The optical ciruit for this interferometer is similar to those recently investigated for sensitivity enhancement and common-mode compensation [4,5]. It is shown schematically,

together with the signal processing required for direct phase conversion, in Fig. 1. The optical transmittance has been shown [4,5] to be

$$T = \frac{1}{2}\left[1 + \sin \Phi(t) \sin P(t) \right] \qquad (1)$$

For the sensor of Fig. 1, the phase shifts in (1) depend on time as

$$\Phi(t) = \Phi_0 + \Phi_1 \sin \omega t \qquad (2)$$

$$P(t) = P_0 + P_1 \sin 2\omega t \qquad (3)$$

where Φ_0 is a dc phase bias and P_0 is the phase shift to be measured by the sensor. Using (2) and (3) in (1) results in a product of two series representations of sin Φ and sin P which have the form,

$$C f_1(m\omega t)\, f_2(2n\omega t),$$

where C is a product of two Bessel functions whose arguments are proportional to Φ_1 and P_1, m and n are integers, and f_1 and f_2 are sines and/or cosines. Since the product $f_1 f_2$ will contain sum and difference frequencies $(m \pm 2n)\omega/2\pi$, the representation of even a single frequency component of T(t) in (1) will be an infinite series.

Therefore, we obtained the magnitudes and phases of the fundamental and second harmonics of T(t) by numerically calculating a Fourier transform for given values of Φ_0, Φ_1, P_0 and P_1. For direct phase conversion, we seek a set of phase modulation amplitudes, Φ_1 and P_1, which yield a linear mapping of P_0 into the electrical phases, $p_e(\omega)$ and $p_e(2\omega)$, of the first and second harmonics of the interferometer output in Fig. 1. A trial and error numerical optimization yields the results shown in Figs. 2 and 3. For $\Phi_0 = 3.9$, $\Phi_1 = 1.6$ and $P_1 = 1.3$ radians, the detected phases are approximately linear in P_0, opposite in slope, and in phase quadrature with each other, as shown in Fig.2.

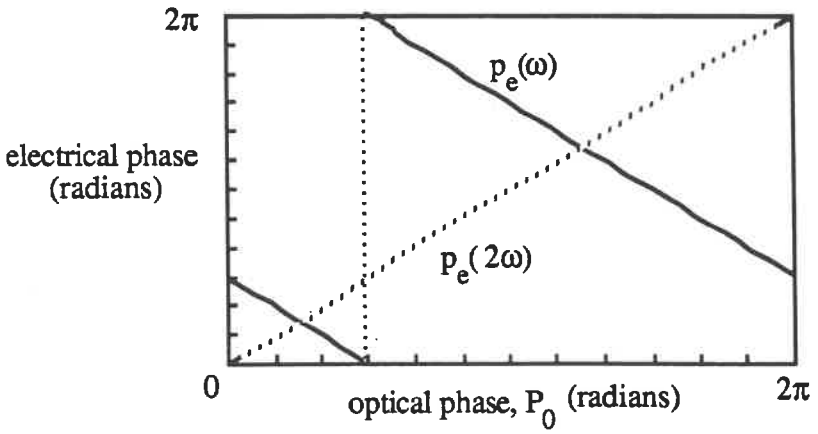

Fig. 2. Dependence of first and second harmonic phases on optical phase shift for optimum phase modulation amplitudes.

The corresponding amplitudes for the two harmonics are shown in Fig. 3. For phase modulation amplitudes near the optimum values, both amplitudes depend only very weakly on measurand phase, P_0. Consequently, relatively simple phase detector circuits

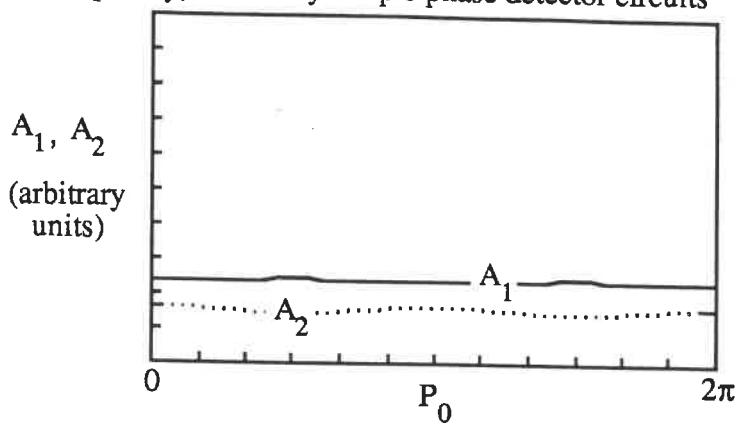

Fig.3. Amplitudes of the first (A_1) and the second (A_2) harmonics of the interferometer output vs. P_0 for the same conditions as in Fig. 2.

can be employed to obtain $p_e(\omega)$ and $p_e(2\omega)$. The numerical analysis also shows that deviations of the phase modulation amplitiudes on the order of 0.1 radian from their optimum values produce very little change in the linearity of the phase shifts shown in Fig.2.

Small changes in the phase bias, Φ_0, do not affect the phase curves in Fig.2, but do change the relative amplitude levels in Fig. 3. For larger drifts in Φ_0, A_1 passes through zero with an accompanying phase reversal (shift by π) in $p_e(\omega)$, as Φ_0 passes through $\pi/2$ and $3\pi/2$. A similar effect is seen in $p_e(2\omega)$, as Φ_0 passes through 0 and π.

As a simple demonstration of the linearity of the direct phase conversion process, we tested an optical circuit similar to Fig. 1, with an impressed phase shift amplitude of $\pi/2$ radians at a frequency of 550 Hz applied via an electrically driven piezo. The modulation frequency, $\omega/2\pi$, for the experiment was 5 KHz. The phase detector circuit consisted of two comparators for signal and reference, followed by an XOR whose output was then low-pass filtered. The impressed phase shift amplitude of $\pi/2$ radians is sufficient to drive the interferometer transmittance through extrema and produce a highly distorted output in T(t) in (1). Figure 4 shows the 550 Hz drive and the outputs of the phase detectors for the first and second harmonics. The filter design should yield approximately equal phase shifts for the first and second harmonics. The sinusoudal drive is reproduced with good linearity in both channels, and the phase quadrature of the outputs is evident from a comparison of traces b) and c). The ripple in trace b) arises from incomplete suppression of the 5 KHz modulation frequency.

HOMODYNE HIGH RESOLUTION AXIAL INTERFEROMETER

Michael Hercher, Geert Wyntjes
OPTRA, Inc.
66 Cherry Hill Drive
Beverly, MA 01915
✆508-921-2100

Summary

In the first part of the paper we describe a precision axial interferometer for metrology based on a stabilized laser diode. Precision phase measurements are made using a spatial heterodyne technique which eliminates the effects of both changes in laser intensity, and cross-talk (common-mode modulation of both interfering beams.) In the second part of the paper we describe a technique for fully compensating for measurement errors due to turbulence and changes in the temperature and pressure of the atmosphere. This technique uses a frequency-doubled beam derived from the main measurement laser; we show that the power in the frequency-doubled beam can be much less than that in the primary beam without affecting measurement accuracy.

Laser Diode Homodyne Interferometer

The 2-frequency HeNe laser commonly used for precision axial metrology has two critical properties: (1) it can be operated at a stable and known vacuum wavelength, and (2) heterodyne detection can be used, thereby allowing the rejection of low-frequency intensity modulation which might otherwise introduce measurement inaccuracies. Laser diode technology is rapidly approaching the point where laser diodes can be locked to atomic or molecular absorption lines, or to stable optical resonators, in order to achieve the sort of wavelength stability ($\sim$1 part in 10^8 or 10^9) needed for measurements at the microinch level or better. Such a laser because of its small size, low power dissipation, and potentially low cost, would make an attractive replacement for the 2-frequency HeNe laser currently in use. We describe below a spatial heterodyne technique which can be used with a laser diode to achieve all of the benefits of temporal heterodyning, with the added bonus that cross-talk (common-mode modulation at the fringe frequency) is eliminated.

Figure 1 below shows a conventional laser interferometer of they type used with 2-frequency laser for precision axial metrology. It is illuminated by a linearly polarized laser diode beam whose polarization vector is roughly at 45° to the axes of the polarizing beamsplitter. Quarter-waveplates serve to direct the return beams towards the detector as shown. These two beams have linear orthogonal polarizations. A weak Wollaston prism serves to introduce a small, carefully controlled divergence angle Θ between the two beams, and a linear polarizer at 45° mixes the two beams so that they can interfere with one another.

The angle Θ is chosen so that the interference fringes formed by the two beams have a spacing of 75 $\pm$ 0.8 microns. This can easily be achieved in practice by adjusting the tilt of the Wollaston prism to fine-tune the angle between the beams (for a 830 nm laser diode, the angle between the beams is about 0.634°). A special silicon PIN-diode detector is used to dectect this interference. It is comprised of an approximately 2 mm x 2 mm array of parallel elements, each 2 mm long and on 25 micron centers. There is a total of 90 such elements, and every third one is wired in parallel. There are thus three outputs from the detector, which we call R, S and T. The detector elements are aligned paralllel to the interference fringes. There are three detector

elements for each fringe, so that when the fringes move (as they will when the optical path in the interferometer changes) the sinusoidal signals from the three channels will be precisely 1/3-cycle out of phase with one another. The three signals can be written:

$$R = I_1 + I_2\cos(\Phi),\ S = I_1 + I_2\cos(\Phi+2\pi/3),\ \text{and}\ T = I_1 + I_2\cos(\Phi+4\pi/3). \quad (1)$$

I_1 and I_2 are the DC light level and the fringe amplitude respectively, and in precision interferometry they should be regarded as variables. In temporal heterodying, it is I_1 that is eliminated by high-pass filtering and it is I_2 that carries cross-talk. In the multiphase detection implied by equation (1) above there are three equations and three variables – I_1, I_2 and Φ. In principle, and in practice, the equations can be rigorously solved for Φ. We have described elsewhere some practical techniques for solving these equations with update rates to 10 MHz.[1] Another useful technique is to generate quadrature signals X and Y from:

$$X = (\sqrt{3}/2)\cdot(S - T),\ \text{and}\ Y = R - (1/2)\cdot(S + T). \quad (2)$$

After digitization, X and Y can be used as input to a 16-bit Pythagorean processor, which solves for Φ:

$$\Phi = \arctan(Y/X). \quad (3)$$

An arithmetic Logic Unit (ALU) and Multiply and Accumulate unit (MAC) can be used to process the phase data and keep track of the total number of cycles. Using this technique we have been able to measure interferometric phase with a precision of better than 12-bits with a 1 MHz measurement bandwidth. This corresponds to a displacement precision of about 0.1 nm.

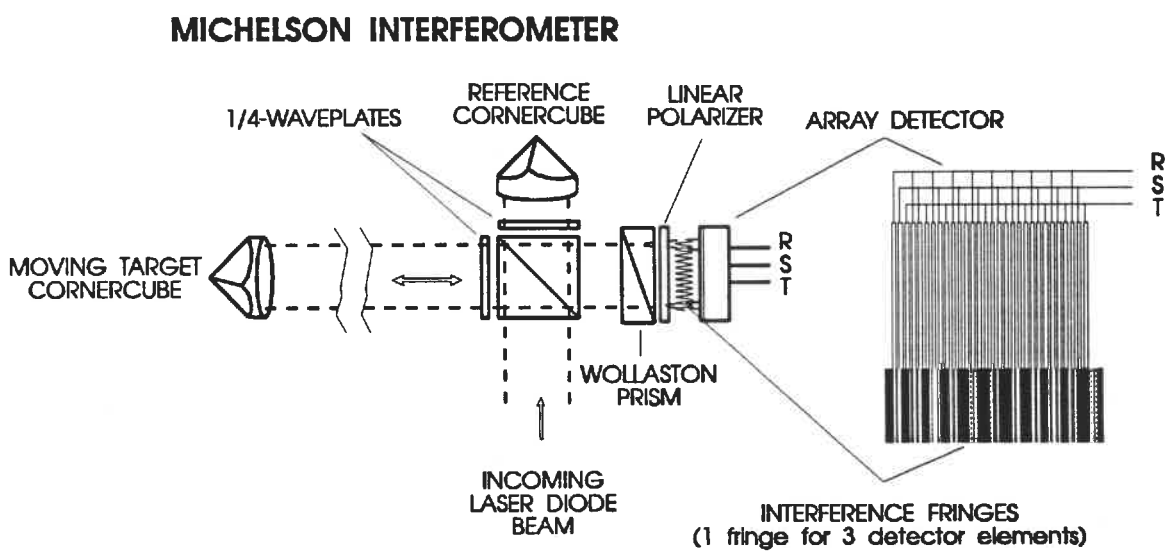

Figure 1

---

1 Michael Hercher & Geert Wyntjes, "Laser Diode Interferometry," Proc. 33rd Annual International Symposium on Optical & Optoelectronic Applied Science and Engineering, 1989.

Correcting for turbulence and atmospheric variations

Statement of the problem: In conventional interferometric metrology, a Michelson configuration is used. One arm of the interferometer contains a fixed reference mirror, and the other has a moving mirror. As the mirror moves the detector signal is modulated. If the mirror moves a distance x, then the change in interferometric phase (measured in cycles) is given by:

$$\Phi(x) = 2xn/\lambda_o, \tag{4}$$

where λ_o is the vacuum wavelength of the source and n is the mean refractive index of the air along the path defined by the displacement x.

The interferometric measurement of the distance x involves (1) measurement of the number of cycles, $\Phi(x)$, (2) knowledge of the source vacuum wavelength, λ_o, and (3) knowledge of the mean refractive index, n(x).

In general, laser sources can be stabilized so that their vacuum wavelength is defined with high precision. Measurements made with such lasers in a vacuum are capable of very high precision – at least 1 part in 10^9. Measurements made in air are a different story. Such measurements require correction for (a) the mean refractive index of the air, and (b) fluctuations in the mean refractive index (along the path of the light) due to turbulence. The refractive index of air at STP is 1.00028. The quantity (n-1) is proportional to the density of the air, which can change by roughly ±5% due to atmospheric pressure and temperature changes. Such a variation causes a corresponding ±0.0015% change in $\Phi(x)$. Without correction for atmospheric pressure and temperature, the measured value of x would be in error by this amount. Our observations of turbulence in a quiet laboratory indicate that over a 30 cm path length there are turbulence-induced mean refractive index fluctuations with an rms magnitude of about 1×10^{-7}, and with a time constant on the order of 0.5 to 1 sec.[2] Any activity in the laboratory (people moving etc.) causes the rms amplitude to increase by 2 or 3 times. Rapid movement of the interferometer mirror causes even larger increases in the turbulence.

Solution: dual-wavelength measurement: For gases at near-atmospheric pressure, and at wavelengths not close to absorption bands, the quantity $[n(\lambda)-1]$ is real and proportional to the density (molecules/cm^3) of the gas. Thus for 2 different vacuum wavelengths λ_1 and λ_2 we can write:

$$n_1 = n(\lambda_1) = 1 + k_1 \rho, \text{ and } n_2 = n(\lambda_2) = 1 + k_2 \rho, \tag{5}$$

where ρ is a normalized measure of the air density (at STP $\rho = 1$) and k is wavelength dependent constant of the atmosphere. (In fact, k varies with humidity and factors such as CO_2 concentration). It is the value of ρ that changes due to both turbulence and macroscopic changes in the atmosphere (temperature and pressure).

For a mirror displacement x, the measureable changes in phase produced at the two wavelengths are:

$$2m_1(x)/\lambda_1 = x(1 + k_1 \rho) \text{ and } 2m_2(x)/\lambda_2 = x(1 + k_2 \rho). \tag{6}$$

Clearly we can solve these two equations for x, thereby eliminating the effect of ρ on the measurement. A particularly attractive case is where $\lambda_1 = 2\lambda_2$ (an approach also suggested by Ishida[3]: this is achieved in practice by frequency doubling in a non-linear crystal. In this case it is straightforward to show that:

---

2 *See also* Norman Bobroff, "Residual errors in laser interferometry from air turbulence and non-linearity," Appl.Opt.**26**, 2676-2682, 1987.

3 Akira Ishida, "Elimination of Air-Turbulence-Induced Errors for Nanometer Laser Interferometric Measurements," to be published.

$$x = m_1(\lambda_1/2) - \Delta m(\lambda_1/2)(k_1/\Delta k), \quad (7)$$

where $\Delta k = (k_2 - k_1)$ and $\Delta m = [(m_2/2) - m_1]$. For an 830nm laser diode source, the values of k_1 and Δk are 0.000275 and 7.13×10^{-6} respectively. For a nominal displacement x of 30 cm, m_1 would be on the order of 723,000, Δm would be roughly 5.15, and $k_1/\Delta k$ would be 38.6. Under these circumstances, the precisions with which we would need to know the critical parameters in order to achieve a measurement accuracy of 1 microinch (25 nm) – in a 30 cm measurement – are roughly as follows:

$\partial\lambda/\lambda_1$	$\pm 2.2 \times 10^{-8}$
∂m_1	$\pm$ 0.03
$\partial(\Delta m)$	$\pm$ 0.001
$\partial(k/\Delta k)$	0.005

In arriving at these numbers we have assumed that the errors are all present at the same time, giving rise to an rms measurement error of ±1 microinch.

Note that the precision required in monitoring Δm is higher than that required for monitoring m_1. This of course means that both m_1 and m_2 have to be monitored with the precision needed for the Δm measurement. In practice, the m_2 measurement can be made with significantly less power than the m_1 measurement because it can be made with a reduced measurement bandwidth: m_1 needs a high bandwidth because of the need to keep track of the integral number of fringes. There is no such need in the case of m_2 – only the fractional phase has to be measured, since the proper value of the integer part of the phase can be inferred from the measured value of m_1. There is, in fact, no need to measure Δm (or, equivalently, m_2) until a measurement is required (m_1 has to be measured continuously in order to keep track of the fringe count).

AN INTERFEROMETRIC SENSOR FOR ABSOLUTE POSITION METROLOGY

J.D. Blum, Dr. C.F. Ferrara
W.J. Schafer Associates
Rome, New York

ABSTRACT: An interferometric sensor is described which is capable of measuring absolute position over a range exceeding 10 microns with an accuracy of 5 nanometers and which can be used as an absolute distance reference (ADR) for machine tool coordinate system initialization. The device is a white-light Michelson interferometer which incorporates new and innovative hardware and software techniques for increasing absolute accuracy. An algorithm is described which will locate the "achromatic fringe" in a single video frame to sub-pixel accuracy by locating the point of maximum local contrast within the fringe packet. An athermal design of the interferometer hardware is presented along with self-calibration and absolute image location referencing techniques. Together these allow correlation of the point of maximum local contrast with the absolute position of a remote target mirror. Performance data of a laboratory prototype is presented.

BACKGROUND: In recent years there have been advances in the state-of-the-art in a number of areas which may now make it possible to find new, practical, cost effective uses for long established, well understood scientific devices.

- Glass materials have been developed which exhibit nearly zero thermal expansion over useful ranges (Corning ULE and Schott ZERODUR). These materials make it possible to build opto/mechanical systems of high dimensional stability.
- Image based sensors have been developed which are being inexpensively mass-produced and which provide huge volumes of digital image intensity data.
- Personal computers have become so fast and powerful that manipulating the huge volume of data from an image based video sensor is now possible with hardware that costs a few thousand dollars.

As part of the WJSA MIST (Monolithic Interferometric Sensor Technology) program these three technology advances as being applied to the development of a new family of scientific measurement instruments based on the fundamental concept of the Michelson Interferometer.

The MIST concept is for a generic group of sensors based on a small Michelson Interferometer constructed from the "zero expansion" materials which would operate in "white light fringe" mode. The sensor would be designed and constructed so that every optically significant dimension would be long term invariant except for the optical path length in one of the interferometer arms. This one path length would be designed to vary only as a continuous function of the one parameter which the sensor was intended to measure. Computerized image processing techniques would be applied to extract measurement data from the location of the interference fringe packet within the image.

A Brassboard Proof-of-Principle experiment in 1990 resulted in the definition of a new algorithm for locating the achromatic fringe by determining the point of maximum local contrast. This algorithm was successfully applied in a laboratory demonstration of the ADR concept which yielded 0.01 micron resolution over a 10.0 micron range.

Recent work has been to refine and optimize the contrast determination algorithm, develop "self-calibration" techniques (involving both hardware and software) and design and fabricate of an athermal interferometer prototype.

SELF-CALIBRATION TECHNIQUES:

Absolute Image Location

Even though it may be reasonable to construct an interferometer from zero expansion materials which is insensitive to temperature change, it is not reasonable to expect similar dimensional stability from a commercial CCD camera.

In order to overcome this potential limitation the reference arm mirror in the interferometer was fabricated to include a unique and easily recognized opaque fiducial pattern. Since this fiducial is actually incorporated into the construction of the athermal part of the interferometer, (coated onto the mirror surface of production models, bonded to the surface of the prototype) its location with respect to the interferometer itself is invariant.

Figure 1 shows this pattern. Image analysis software was written which locates this fiducial pattern in the image and corrects the measured fringe location for any changes in the location of the fiducial.

Figure 1 MIST Reference Mirror Format

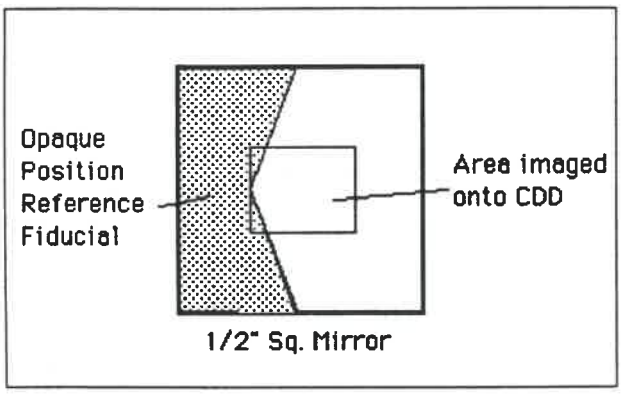

Wedge Angle Calibration: In order to relate movement of the fringe with respect to the fiducial to actual movement of the target mirror it is necessary to accurately know the wedge angle between the target mirror and the image of the reference mirror as seen through the beamsplitter cube. In order to measure this angle a portion of the light source is viewed through a narrow band dielectric filter of well known central wavelength. This produces a continuous set of fringes across the full width of the interferometer.

Software has been written which performs a Fourier Transform to determine the frequency of the fringes in the pattern. This frequency is combined with the knowledge of the absolute wavelength to convert the motions of the white light fringes into measured displacements of the mirror.

Figure 2: MIST ADR Fringe Pattern

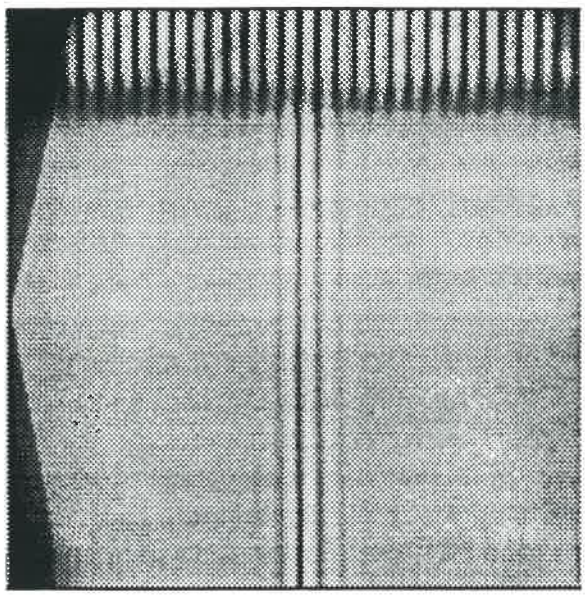

The top portion of Figure 2 shows the actual calibration fringes obtained from the prototype.

Fringe & Image Distortion: Our discussion so far has made the assumption that the reference and target wavefront are perfectly flat and that the geometrical imaging onto the CCD is without distortion. However, when we need flatness of a few nanometers and distortion of less than 0.1%, perfection cannot be assumed.

Surface curvature and geometrical distortion will result in a nonlinear relationship between fringe and mirror position. An algorithm has been developed to determine the magnitude of these nonlinear terms by measuring their effect on the calibration fringes.

Figure 3 Simulated Effect of Power and Distortion

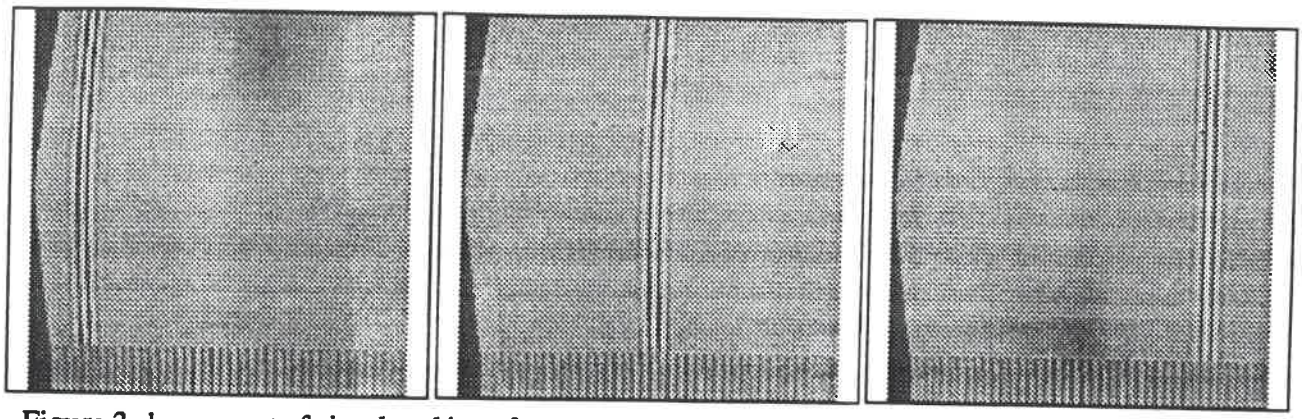

Figure 3 shows a set of simulated interferograms with exaggerated amounts of surface curvature and distortion.

Interpreting these interferograms with the assumption of perfect surfaces and imaging led to an error of 200 nanometers. Application of this correction algorithm reduced this to 12 nanometers.

Figure 2 shows actual fringes from the MIST ADR prototype. They exhibit no curvature or distortion which can be discerned by eye. The correction algorithm finds a small amount resulting in a maximum correction of 15 nanometers in a 5,000 nanometer reading.

INTERFEROMETER DESIGN:

Optical Considerations

Figure 4 shows the optical design of the interferometer.

This differs from the classic Michelson Interferometer in several ways. The extended light source normally used has been replaced by a collimated source created by placing a small incandescent lamp at the focus of an achromatic doublet.

A split aperture filter was added in the source arm. One section of the aperture was an narrow band interference filter centered at 0.670 microns. The remainder of the aperture was a 2.0 neutral density filter.

The fringes appear in the plane of the target and reference mirrors as seen through the cube. The imaging lens is positioned to focus this plane onto the CCD with a magnification of 1.25. The fiducial mask is located of the surface of the reference mirror and therefore is in focus on the CCD.

Figure 4 MIST ADR Optical Layout

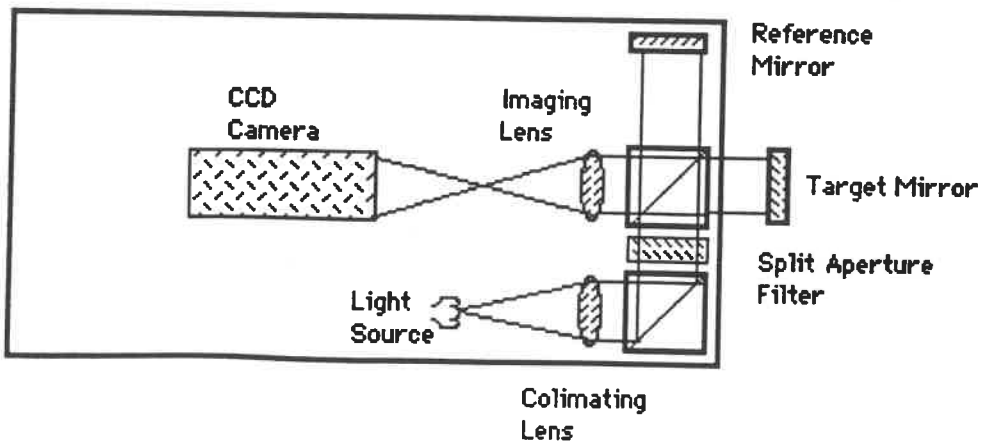

A second beamsplitter cube is used in the source arm to allow for the injection of a laser alignment beam used in initial set-up. Figure 5 is a photograph of the actual prototype with its cover removed.

Thermal Mechanical Considerations: Utility of the interferometer as a long term absolute reference will depend of the stability of the optical path length defining the reference arm and on the stability of the spatial relationship between the interferometer front cube face and its mounting attachment point. The relationship between this mounting point and the target mirror is also critical but clearly that is an application dependent consideration which must be addressed by the user.

In order to insure a stable reference arm we chose to make the beamsplitter cube from BK7, the reference mirror from fused silica and to hold them in a fixed relationship by bonding them to a bar of ULE.

The ULE bar carrying the beamsplitter and the reference mirror was then mounted to a larger ULE plate which would provide an attachment surface for the other components and give the needed thermal stability to the mounting points for the unit as a whole.

Figure 6 is a bottom view of the MIST ADR prototype in which the mounting technique can been seen.

A 3-point kinematic mount is used. Precision steel half-balls are mounted to ULE interferometer base plate. One ball is directly below beamsplitter cube and the other two are positioned to place the center of gravity of the unit in the center of the triangle formed by the balls.

The ULE interferometer base plate was mounted into an aluminum frame and held in place by RTV rubber. The frame was positioned so that it sits 0.01" above the surface which is defined when the three balls are properly seated. The frame is then drawn against the mounting surface by its screws applying a well controlled load through the rubber in the direction pressing the balls into their seats.

EXPERIMENTAL RESULTS: The completed prototype was taken to Rank Taylor Hobson, Inc. and installed on a Nanoform 600 diamond turning machine for testing. The results of this testing are detailed in a separate paper by T.A. Sebring, which is included in the proceedings of this conference.

Figure 5 MIST ADR Prototype

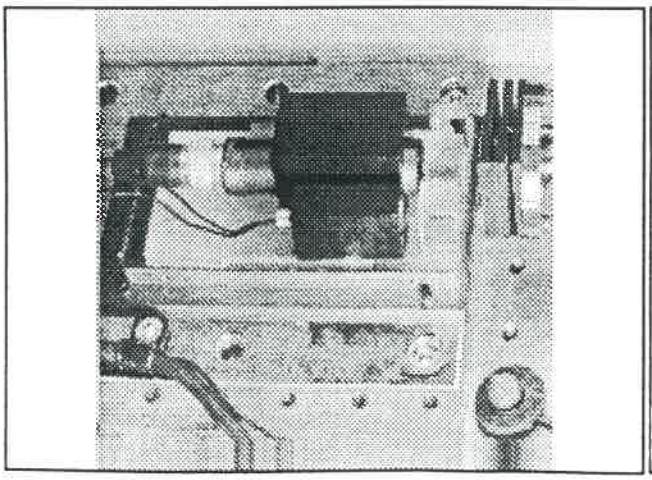

Figure 6 MIST ADR Kinematic Mount

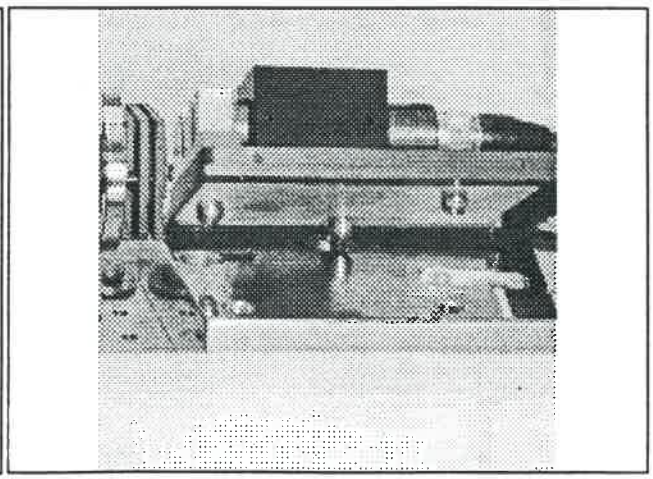

QUALIFICATION AND PERFORMANCE ANALYSIS OF AN INTERFEROMETRIC SENSOR

T.A. Sebring, Dr. C.F. Ferrara
W.J. Schafer Associates
Rome, New York
D. Youden, M. Gershman
Rank Taylor Hobson
Keene, New Hampshire

Background: On 16 December 1991 testing of the MIST ADR was performed at Rank Taylor Hobson, in Keene New Hampshire. RTH has agreed to support WJSA in development of MIST in the expectation that the gages developed through this effort will result in enhancement of their products. No concessions or promises have been made to RTH by WJSA, though they have been extremely generous with their time in reviewing gaging concepts and applications.

Setup: The machine used as a testbed was the Nanoform 600, RTH's premier and newest SPDT lathe. The machine utilizes hydrostatic bearings and is close loop position controlled using a Zygo Axiom heterodyne interferometer to measure linear position. This measurement system is reputed to exhibit accuracies of as good as 2.5 nanometers in this application.

Figure 1 shows the location of the MIST ADR on the Nanoform 600 as well as the position of the Zygo system and a third displacement measurement system (a capacitance probe) which was also installed. Note that there are approximately 18 inches separating the axis on which the Zygo system measures linear position and the machine workpiece spindle. Since position control is closed about the Zygo, variations in spacing at the workpiece spindle (which the MIST ADR was set up near) can occur, particularly if the temperature varies. The capacitance gage was much closer to the ADR, only about 6-8 inches away.

Tests Performed: A series of tests were performed. These consisted of a Drift Test, Incremental Positioning Tests, Full Range Test, and a Repeat Initial Position test. The intent was to demonstrate that the MIST ADR agreed with the Zygo System to better than 10 nanometers, was capable of stable operation over extended periods of time, and could reproduce a specific initial position even after large excursions outside the range of the sensor when returned to within range.

Data: Data was recorded directly on the MIST computer for the ADR position and the temperature at the ADR sensor (as sensed by a 0.01 degree C resolution thermistor.) A second com-

Figure 1: Configuration of Sensor on Nanoform 600

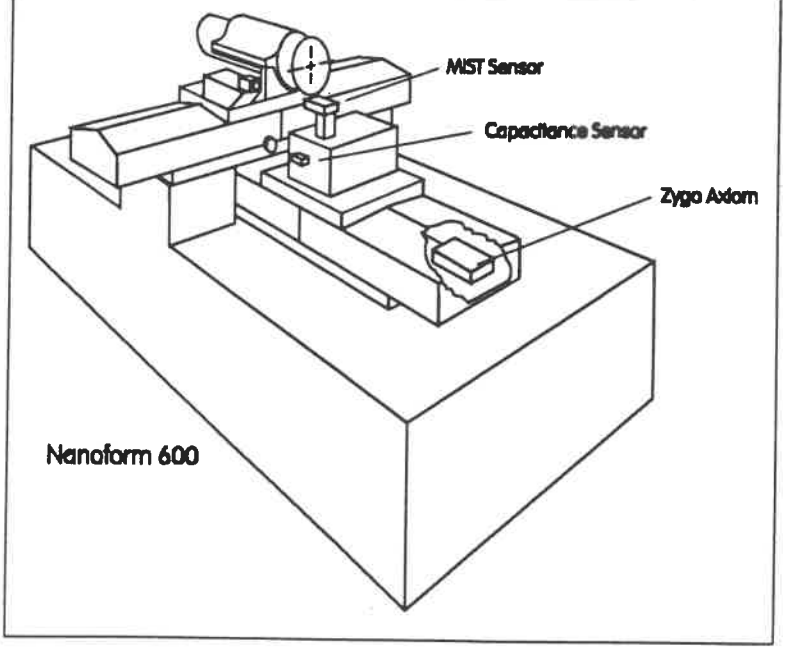

puter recorded the Zygo Position data. The clocks of the two computers were synchronized and all measurements made on a common time base for later comparison. The output of the capacitance gage was recorded on a strip recorder and later digitized by hand and input to support data analysis. Additional observation of the temperature of the air shower which surrounded the Nanoform 600 was made via the RTH thermal control system, but was not recorded. Full range observed was on the order of 0.3 degrees C during any of the test runs.

Analysis: The following sequential analysis was performed.

Step Test: During this test linear position was varied by 10 nanometers per step. Each position was maintained for 30 seconds during which data was acquired by all systems. Six steps were made in one direction and then retraced back to the original position. Figure 2 illustrates the position recorded by each sensor.

Figure 2: Position vs Time for All Sensors

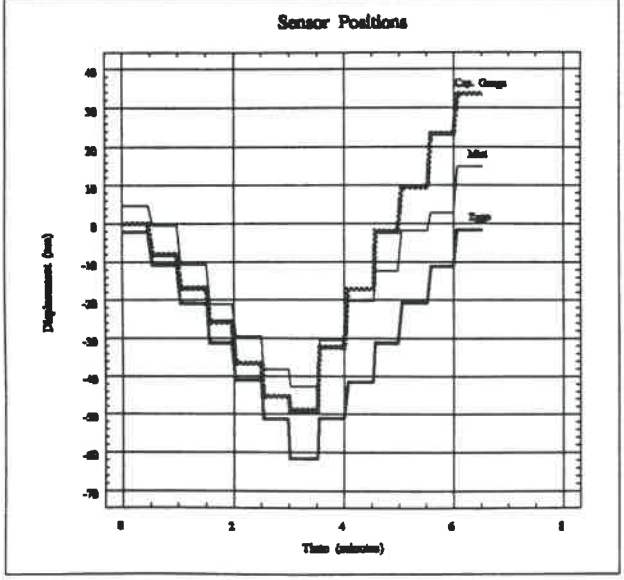

Figure 3 illustrates the difference between each of the sensors. Maximum deviation between the MIST sensor and the Zygo was approximately 12 nm forgiving initial offset. The Zygo to capacitance gage difference was approximately 34 nm. Note that the maximum difference between the MIST and Zygo systems is smaller than the accuracy specified by RTH for positioning of the Nanoform 600 by RTH.

Figure 3: Differences Between Sensors vs Time

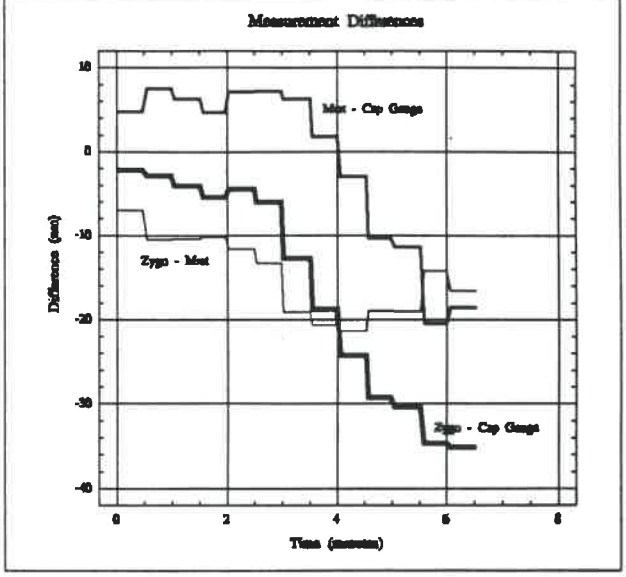

Figure 4 shows the correlation between the MIST ADR and the Zygo gage. The correlation Coefficient is high, 0.973, showing excellent performance of the MIST sensor.

Figure 4 Correlation Between MIST Sensor & Zygo Measurements

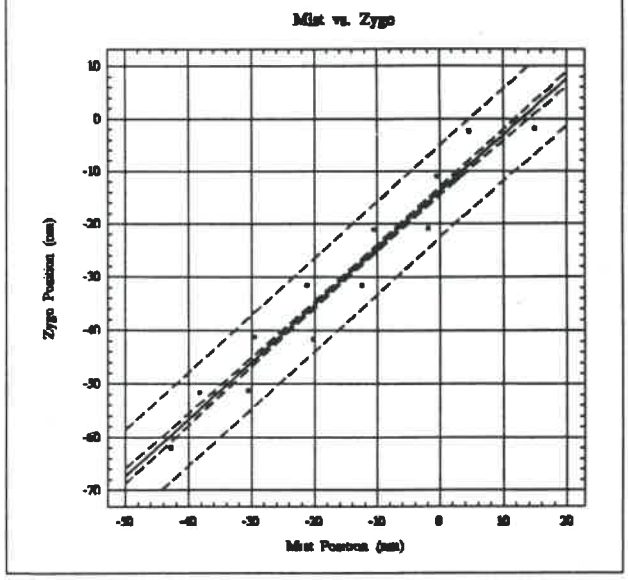

Figure 5 shows correlation between the Zygo and the capacitance gage. The correlation coefficient of 0.868 shows a lower degree of correlation than between the ADR and the Zygo.

Figure 5: Correlation Between Cap Gage & Zygo Measurements

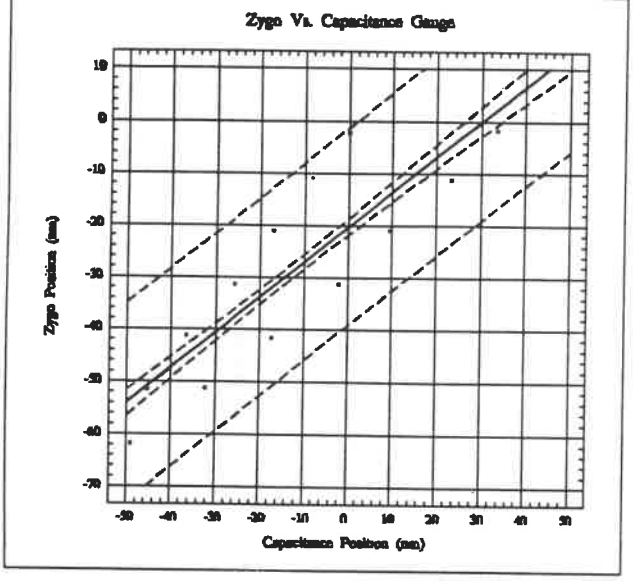

Figure 6 illustrates the correlation between the MIST and the capacitance sensor.

Figure 6: Correlation Between MIST Sensor & Cap Gage Msmts

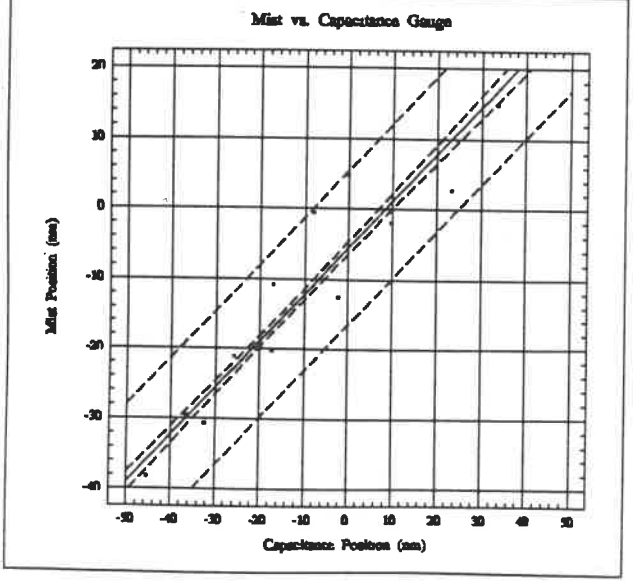

Figure 7 is a plot of the temperature at the MIST sensor during the test period. Multiple readings were averaged for each time period. The magnitude of the temperature variation during the entire test was approximately 0.7 degrees C.

Figure 7: Temperature Vs Time During Test

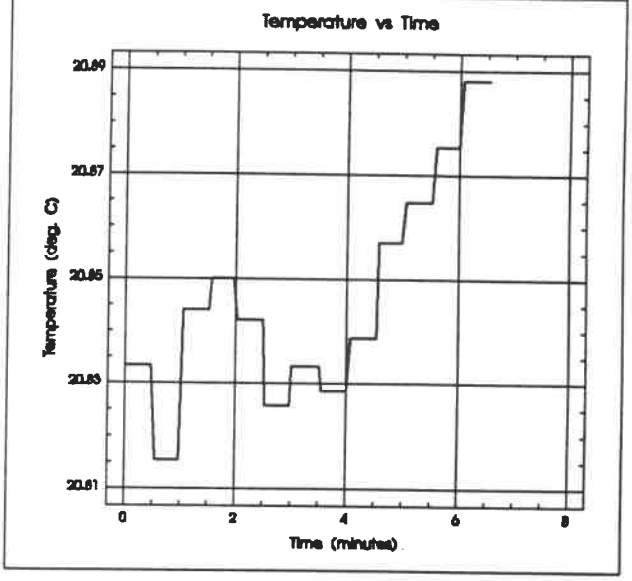

Figure 8 illustrates the correlation of the difference between the MIST sensor and the Zygo with temperature. The relatively low correlation (0.208) shows that the MIST sensor is relatively little affected by temperature.

Figure 8: Correlation Of MIST Difference To Temperature

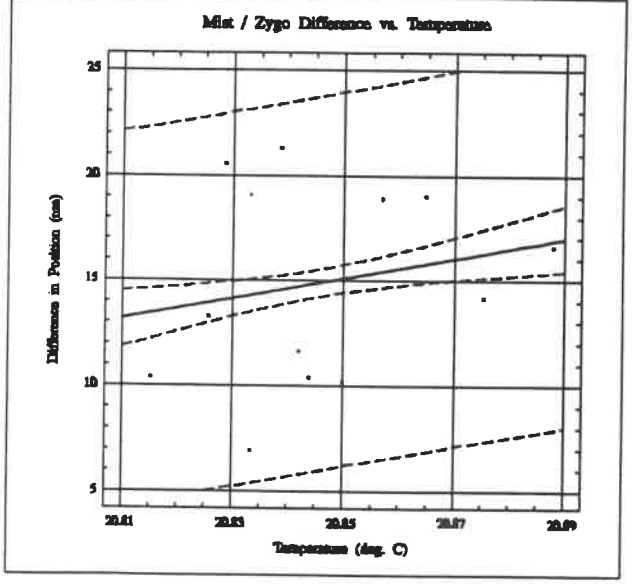

Figure 9 shows the much higher degree of correlation between the difference between the Zygo and the capacitance gage to temperature.

Figure 9: Correlation Of Cap Gage Difference To Temperature

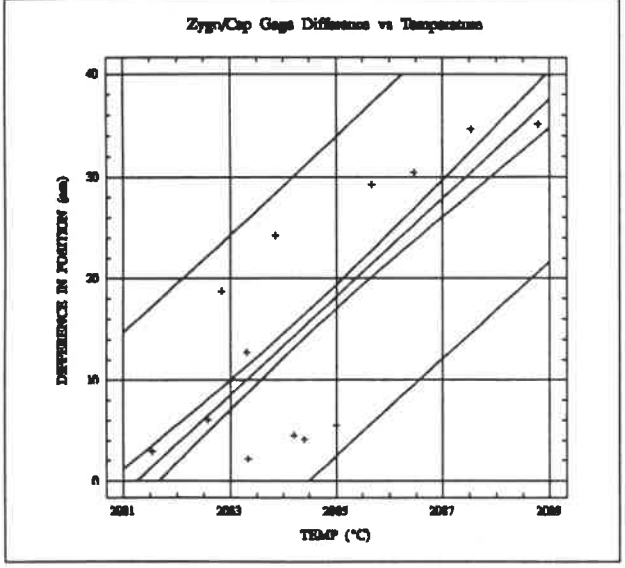

Full Range Test: In this test the position was changed incrementally in 500 nm steps to explore linearity of the MIST sensor over it's full range Figure 10). As can be seen in Figure 11, the difference between the MIST ADR readings and the Zygo appear functional in nature and can be shown to have a functional dependence as shown by the 4th order polynomial fit.

Figure 10: MIST & Zygo Position Over 6 Microns

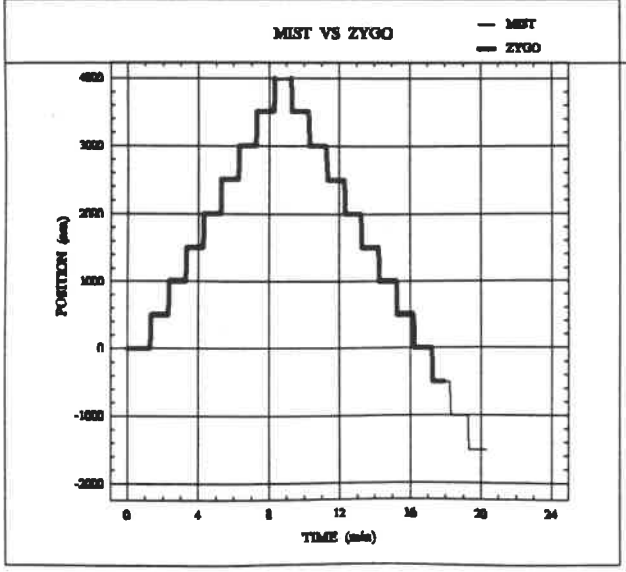

Figure 11: MIST/Zygo Difference Vs Position

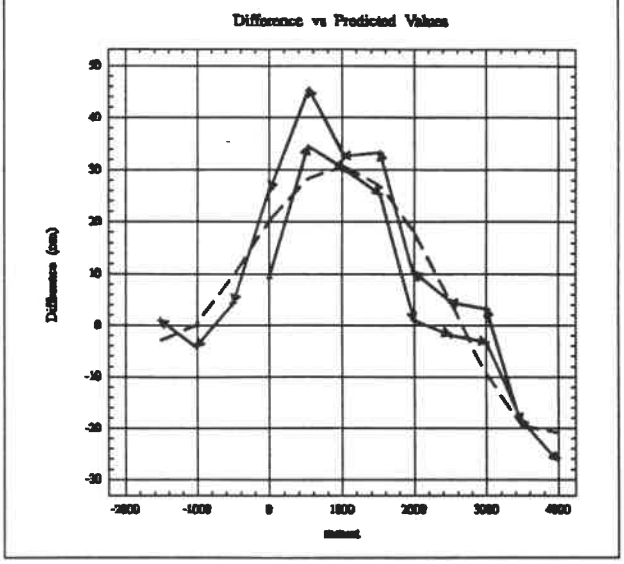

Drift Test: In this experiment, position remained steady in closed loop fashion about the Zygo Axiom. MIST position was monitored, and as can be seen in Figure 12, the MIST sensor shows a nearly linear drift over 30 minutes. the monotonic nature of change of MIST sensed position is in contrast to the temperature sensed at the MIST sensor by the thermistor, which rose and fell several times during the test.

Figure 12: Position & Temperature Vs Time

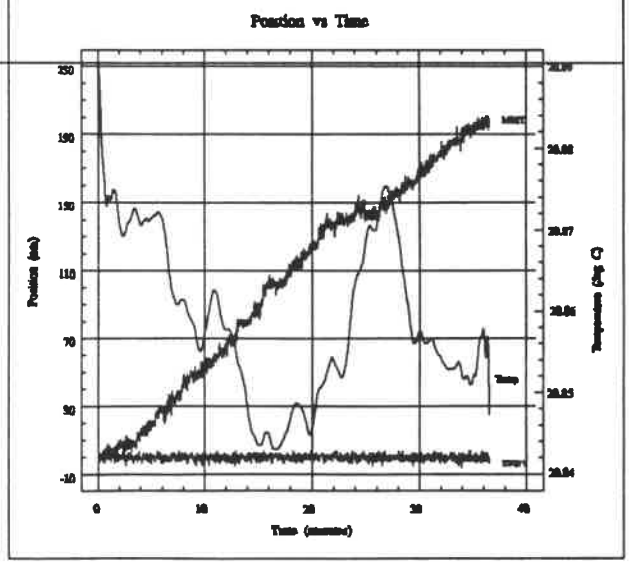

Repeatability of Position Test: An initial position was established and maintained within the MIST capture range for several minutes. Subsequently, the carriage was translated far beyond the capture range of the MIST sensor and then returned. The object was to determine whether the MIST sensor would return to the same position as the Zygo indicated and hence determine it's capability as an initialization sensor. Figure 13 shows the substantial drift which occurred during the replications of this test.

Figure 13: Errors In Achieving Repeated Initial Positioning

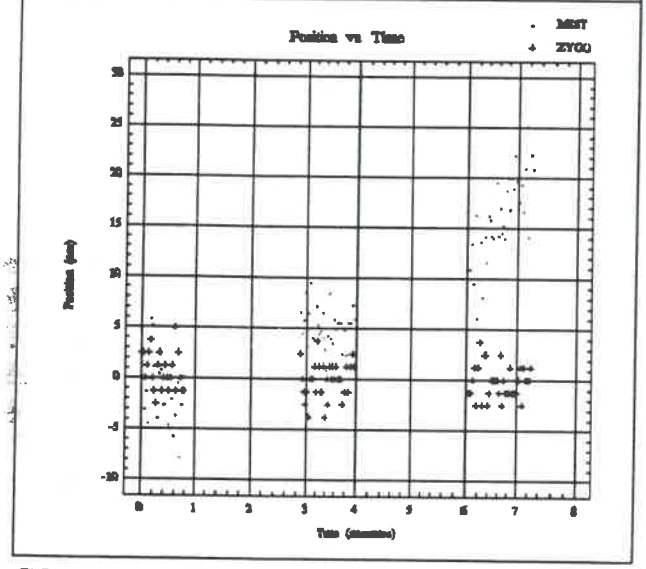

CONCLUSIONS: The following are our conclusions on each of the tests performed.

Step Test: The high degree of correlation between the MIST sensor and the Zygo positions illustrates that resolution and accuracy of the MIST sensor meet our initial objectives of on the order of 10 nanometers. The performance of the MIST sensor clearly exceeds that of the commercially available capacitance sensor, which showed a high degree of dependence on temperature. The MIST ADR was little affected by temperature, a fact which we attribute to the use of low CTE components in it's construction.

Full Range Test: This test showed a functional error in MIST ADR position measurement over it's full operating range of about 10 microns. We believe that this is due to optical aberrations inherent to the beamsplitter cube and mirrors and the extrapolation of fringe position which is used to make the measurement. We believe that we have several viable alternatives which will substantially reduce this error. The error is repeatable, and hence, even if no other approach resolved it, it could be accommodated through calibration.

Drift Test: The constant near linear drift of the MIST sensor is hypothetically attributed to bulk thermal drift of the Nanoform 600 during the course of the test. While the temperature sensed at the MIST sensor had several inflection points, it is more reasonable for the bulk temperature of the Nanoform machine to vary monotonically over the course of the test due to it's substantial thermal inertia. The way we would propose to resolve this problem is to redo this test with the Zygo and the MIST sensor measuring very nearly the same coaxial space, rather than 18 inches apart.

Repeatability of Position Test: This test also showed the same linear drift as the Drift Test. We believe that this test is flawed for the same reason as that one. We propose to establish a low CTE test fixture which will provide a highly stable geometry to test drift and repeat position against.

SUMMARY: In summary, the testing of the MIST ADR at Rank Taylor Hobson showed that our sensor has genuine promise as a competitor to current, commercially available gaging systems. It also showed that a more dedicated test system or modification to machine tool brassboards will be necessary to support efficient development and refinement of the MIST sensor. The basic objectives of our IR & D program have been met, though shortfalls in stability and full range linearity were observed. The nature of the errors observed are an excellent match to the hypotheses we have developed to explain them. Consequently, we are encouraged by the results of this initial test program and MIST will continue to be refined and developed.

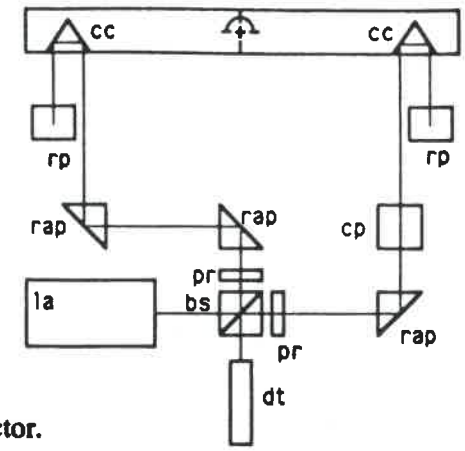

Fig. 1. Polarization sensitive heterodyne angle interferometer. la: laser, dt: detector, bs: polarization sensitive beam splitter, pr: 90 degree polarization rotator, rap: right angle prism, cp: compensation plate, rp: roof prism, cc: corner cube.

and exit beams are displaced. As the corner cube rotates, it also translates across the fixed input beam. The first exit beam from the cornercube also translates across the face of the roof prism while the second exit beam from the corner cube is fixed in space. Thus the exit beams from the two arms can be made to overlap for all angles and to maintain a fixed position on a small detector.

The Michelson interferometer response is a sine curve which is very convenient for up/down counting in order to measure large interferometer motions. However, the sine curve response presents a challenge when it is necessary to measure fractional wavelength path changes. Sensitivities which permit fringe splitting in the 10^{-3} to 10^{-4} range are not trivial to achieve and it is well known that the sine curve may be non-linear. Because of the availability of commercial 2 frequency lasers and phase measuring instruments, our most recent angle measuring interferometers have all used heterodyne encoding. In the next section, three simple heterodyne interferometers that have been tested for linearity are discussed.

III. Simple Heterodyne Interferometers: All of the components of the interferometers which have been tested are commercially available items. The light source is a stabilized Zeeman split He-Ne laser (λ= 633 nm) which emits 2 frequencies separated by 1.8 MHz and orthogonally polarized.[10] Earlier publications on precision interferometry using 2 frequency Zeeman split lasers, reported non-linearities on the order of 0.01 fringes.[11,12] More recent publications on subnanometer metrology have described nonpolarization heterodyne interferometry in which the two frequencies are produced by acousto-optic modulation.[13,14] This technique more cleanly separates the two frequencies and non-linearities < 0.001 fringes have been reported. The simplicity of the 2 frequency Zeeman split laser is the motivation for investing effort to reduce the non-linearity associated with polarization sensitive heterodyne interferometry. The aim of this report is to show that, with care, non-linearity errors associated with polarization sensitive heterodyne interferometry can be reduced to ~0.001 fringes. The phase measuring electronics is a time interval counter[15] capable of measuring the phase difference between two signals with an error of < 0.6 degrees for a frequency of 1.8 MHz (manufacturer's specification). However, independent testing by the NIST electricity division shows phase errors on the order of 0.1 degrees.[16]

The interferometers were tested for nonlinearity by ramping the pressure in a gas cell placed in one arm of the interferometers. The cell was evacuated and slowly filled with dry nitrogen through a needle valve. The fringe number including fraction and the pressure were continuously monitored with approximately 60 values being recorded for a path change of one wavelength in about an hour. A run consisted of 7 to 10 hours of continuous recording in which the pressure increased from 0 to about 7.5 x 10^4 Pa (0.75 atmospheres). After fitting the fringe vs. pressure data with a low order polynomial, the residual non-linearity was determined by substracting the fit fringe values from the measured fringe values. These residuals were Fourier analyzed and fit with a sine function having an initial period of 1 wavelength. The sine function fit primarily estimates the non-linearity at the fundamental frequency (1 wavelength) while the Fourier analysis identifies all frequency components.

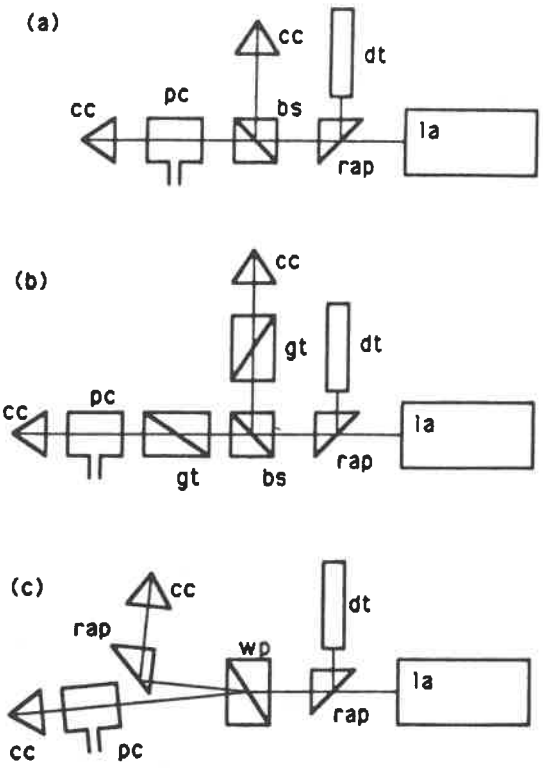

Fig. 2. Test interferometers. a)polarization sensitive beam splitter, b) polarization sensitive beam splitter and Glan Thompson polarizers, c) Wollaston prism. la: laser, dt: detector, bs: polarization sensitive beam splitter, rap: right angle prism, cc: corner cube, pc: pressure cell, gt: Glan Thompson polarizer, wp: Wollaston prism.

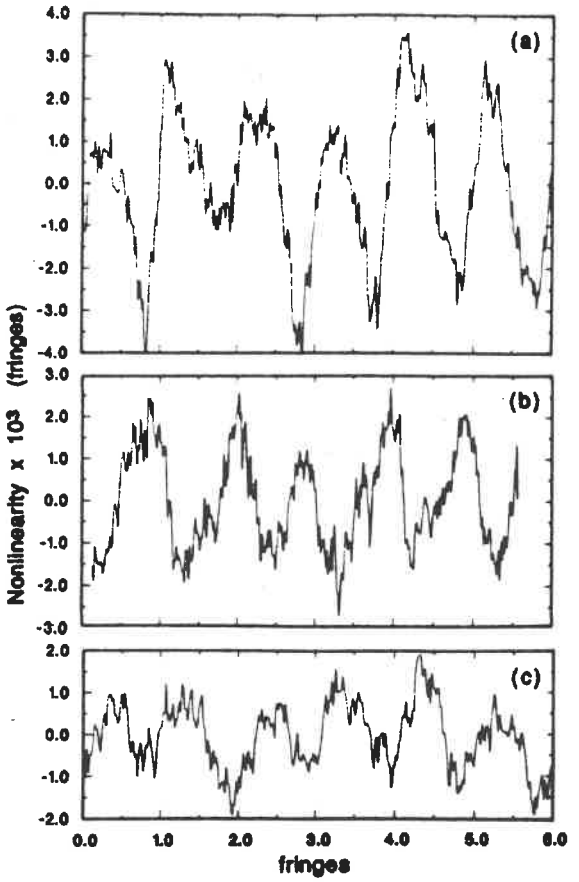

Fig. 3. Deviations from linearity. The absicca is in fringes (derived from pressure) and the ordinate is nonlinearity. a) polarization sensitive beam splitter, b) polarization beam splitter and Glan Thompson polarizers, c) Wollaston prism.

Four nearly identical lasers were available for interferometer testing. The lasers were compared for frequency isolation and orthogonality of polarizations using a beat-note detector and one of the lasers was excluded because of an unusually large residual beat-note. No attempt to modify or adjust the optics internal to the laser in order to improve polarization isolation of the two frequencies was made. For polarization sensitive heterodyne interferometry, single frequency orthogonal polarization states from the laser are essential.

A. Interferometer having polarization sensitive cube beam splitter: In figure 2a the optical layout of this interferometer is shown. The beam splitter is a cube with a polarization sensitive coating. The cube was tipped so that the polarization eigenstates of the splitter and the input beam coincide. This adjustment can be made using a beat-note detector or a polarizer and an intensity detector. In figure 3a typical non-linearity for this interferometer is shown. The measured amplitude of the non-linearity component with a period of 1 fringe is ~0.003 fringes. With an intensity meter and a polarizer, the intensities of the wanted and unwanted frequencies in each of the arms were measured. Using the analysis of Bobroff[12], the expected non-linearity is ~0.008 fringes.

B. Interferometer having polarization sensitive cube beam splitter and Glan Thompson polarizers: Glan Thompson polarizers were introduced into each arm of the previous interferometer (figure 2b). The Glan Thompson polarizers were oriented to suppress the unwanted polarizations and frequencies. In figure 3b, typical non-linearity for this interferometer is shown. The component of non-linearity at the period of 1 fringe is reduced by the polarizers, but significant non-linearity remains.

C. Interferometer having a Wollaston prism beam splitter: In this interferometer (Fig. 2c) the distance between the Wollaston prism and the right angle beam bender was ~15 cm so that the two beams were completely spatially separated. The Wollaston prism was rotated so that the two separated beams were pure polarization states as sensed by a beat-note detector. The behavior of this interferometer was considerably more reproducible than the previous interferometers. The variability of the measured non-linearity amplitude was < 0.001 fringes for several realignments. A typical residual non-linearity scan is shown in figures 3c. The non-linearity amplitude of this interferometer is ~0.001.

IV. Conclusion: Millifringe Michelson interferometry is needed to make precision gamma-ray wavelength measurements. Three polarization sensitive heterodyne interferometers have been tested for non-linearity using pressure scanning. The scans that are shown here are typical of a much larger collection of data that has been recorded. Mixing of frequencies in the interferometer arms contribute to non-linearity. Glan Thompson polarizers reduce the frequency mixing. A Wollaston prism appears to be a significantly superior polarization sensitive beam splitter than a polarization sensitive coating. Non-linearity amplitudes of ~0.001 fringes have been achieved. For double passed retro-reflectors, this non-linearity contributes 0.2 to 0.3 nm to a displacement measurement.

References

1. R.D. Deslattes, E.G. Kessler, W.C. Sauder, and A. Henins, Ann. Phys. (N.Y.) 129 (1980), 378.
2. R.D. Deslattes, in The Art of Measurement, B. Kramer, Ed. Weinheim, Germany: VCH Verlagsgesellschaft (1988), 193.
3. R.D. Deslattes and A. Henins, Phys. Rev. Lett. 31, (1973), 972.
4. R.D. Deslattes et al., Phys. Rev. Lett. 33 (1974), 463.
5. R.D. Deslattes et al., Phys. Rev. Lett. Comm. 36 (1976), 898.
6. R.D. Deslattes and E.G. Kessler, Jr., IEEE Trans. Instrum. Meas. 40 (1991), 92.
7. E.G. Kessler, Jr., R.D. Deslattes, and A. Henins, Phys. Rev. A 19 (1979), 215.
8. E.G. Kessler, Jr., G.L. Greene, R.D. Deslattes, and H.G. Borner, Phys. Rev. C 32 (1985), 374.
9. E.G. Kessler, Jr. et al., AIP Conference proceedings 238, R. Hoff, Ed., (N.Y.) (1991), 199.
10. The lasers that were used were Model 5501 obtained from Hewlett-Packard Corporation, Santa Clara, California.*
11. C.M. Sutton, J. Phys. E, 20 (1987), 1290.
12. N. Bobroff, Appl. Opt. 26 (1987), 2676.
13. M. Tanaka, T. Yamagami, and K. Nakayama, IEEE Trans. Instrum. Meas. 38 (1989), 552.
14. P.G. Charette, I.W. Hunter, and C.J.H. Brenan, Rev. Sci. Instrum. 63 (1992), 241.
15. The phase measuring electronics was model SR620 obtained from Stanford Research Systems, Sunnyvale, California.*

16. We acknowledge Mr. Nile Oldham of the NIST Electricity Division for these measurements.

*Manufacturers of certain items are identified where it was thought that such identification contributed to completeness in description of our apparatus. Such identification does not imply endorsement nor should it be taken to suggest that the identified items are necessarily best suited to the applications in which they are used.

Elimination of Polarization Mixing Errors in Single Frequency Distance Measuring Interferometers

Extended Abstract

Walter Augustyn
CMX Systems, Inc.
130 Research Parkway
Meriden, CT 06450

Paul Davis
Mathematical Sciences Department
Worcester Polytechnic Institute
Worcester, MA 01609

1 Introduction

Helium-neon distance measuring interferometers (DMIs) use either heterodyne detection to sense velocity or fringe counting to sense position directly. In either technology, the target position is ultimately determined by the zero crossings of the ac component of the interference signal. If the ac signals include harmonic distortion, then edge position errors will occur and absolute accuracy will be reduced.

One source of such errors is polarization mixing, which causes a small fraction of the reference frequency to travel over the measurement path and vice versa. Polarization mixing is unavoidable; polarizing beam splitters are characterized by a figure of merit known as the *extinction ratio*. It is the ratio of the intensity of the S polarized light reflected to that of the P polarized light along the S channel. This ratio is applied to the transmission channel as well. Mixing occurs even with extinction ratios as high as 1000:1.

This polarization mixing introduces distortion in the interference signal which can be calculated explicitly. These effects were first described for heterodyne systems by Bobroff [2] and for a single frequency system by the authors [3]. The latter paper showed that the effects of polarization mixing on the accuracy of target position is much smaller in the single frequency system than in the heterodyne system.

The present paper refines that earlier work using a suggestion of V. Beck [1]. With proper calibration, *fringe counting errors can be made totally immune to zero-crossing errors* produced by polarization mixing. The analysis presented here shows that errors in the required calibration have only a small effect on zero-crossing accuracy.

To provide background for that presentation and for the convenience of the reader, the next section briefly summarizes the analysis and conclusions of [3]. The third section implements Beck's suggestion and analyzes its practical limits.

2 Background and previous results

A fringe counting interferometer employs a polarizing beam splitter to create linearly polarized, orthogonal reference and target beams of the same frequency. The position

of the target is established in the fringe counting optical phase decoder by measuring the phase difference d between the two polarized components after they pass through a quarter wave plate. The quarter wave plate is positioned so that the two beams become circularly polarized with opposite parity.

The time-averaged intensity of the two waves before the polarizer is

$$\langle I \rangle = A^2 + B^2 + \alpha^2 + \beta^2 + 2(\alpha B + \beta A)\cos d. \tag{1}$$

Each circularly polarized wave with ideal amplitude A, B has been corrupted by a small out of phase signal, whose amplitude is denoted by the corresponding lower case Greek letter. (The reference arm amplitudes are A, α. The measurement arm amplitudes are B, β. The signals with amplitudes A, β are S polarized before the quarter-wave plate. Those with amplitudes B, α are P polarized before the quarter-wave plate.)

The time-averaged intensity after a polarizer set at $\theta = 0$ is

$$\langle I_0 \rangle = \frac{1}{2}[(A+\alpha)^2 + (B+\beta)^2] + (A+\alpha)(B+\beta)\cos d, \tag{2}$$

and the intensity recorded after a polarizer set at a 45° angle is

$$\begin{aligned} \langle I_{45} \rangle &= \frac{1}{2}(A^2 + B^2 + \alpha^2 + \beta^2) \\ &\quad + (\beta A + \alpha B)\cos d + (AB - \alpha\beta)\sin d. \end{aligned} \tag{3}$$

Combinations of these three time-averaged intensities (1–2–3) then produce the four signals whose zero crossings identify phase values of $d = 0°, 90°, 45°$, and $135°$, respectively.

To eliminate the dc terms arising from the modulation introduced by polarization mixing, construct the signals

$$S_1 = \langle I_{45} \rangle - f_{45}\langle I \rangle ,$$

$$S_2 = \langle I_0 \rangle - f_0\langle I \rangle ,$$

where $f_0 = \dfrac{1}{2} + \dfrac{\alpha A + \beta B}{A^2 + B^2 + \alpha^2 + \beta^2}$ and $f_{45} = \dfrac{1}{2}$ are attenuation factors chosen so that S_1 and S_2 each have zero dc level.

Using these values of the attenuation factors , we obtain

$$S_1 = (AB - \alpha\beta)\sin d,$$

$$S_2 = (AB - \alpha\beta)\frac{1-r}{1+r}\cos d,$$

$$S_1 - S_2 = (AB - \alpha\beta)\left(\sin d - \frac{1-r}{1+r}\cos d\right), \tag{4}$$

$$S_1 + S_2 = (AB - \alpha\beta)\left(\sin d + \frac{1-r}{1+r}\cos d\right), \tag{5}$$

where $r = \dfrac{\alpha^2 + \beta^2}{A^2 + B^2}$.

Cross Polarization Ratio	Single Frequency Phase Angle Error $\delta < \tan^{-1}\epsilon_{\max}^2$	Heterodyne Phase Angle Error $\delta < \tan^{-1} 2\epsilon_{\max}$
0.110	0.58° ($\lambda/1200$)	11.31° ($\lambda/63$)
0.030	0.057° ($\lambda/12000$)	3.62° ($\lambda/200$)

Table 1: Upper bounds on zero-crossing phase-angle error δ for the single frequency interferometer and the heterodyne interferometer.

In [3], we found that the zero crossings of S_1 and S_2 are *error free*: $S_1 = 0$ *exactly* at $d = 0°$ and $S_2 = 0$ *exactly* at $d = 90°$. That is, the accuracy of the 0° and 90° position measurements is not affected by polarization mixing, in contrast to the heterodyne interferometer, whose zero-crossing phase-angle error δ is given in [2] as

$$\tan\delta = \frac{\alpha}{A} + \frac{\beta}{B}.$$

In the single frequency interferometer, the combined signals $S_1 \pm S_2$ provide the 135° and 45° zero crossings. The errors in those zero crossings are [3]

$$\tan\delta = \frac{\alpha^2 + \beta^2}{A^2 + B^2}.$$

Table 1 displays upper bounds on the zero-crossing errors in terms of the maximum cross polarization ratio, $\epsilon_{\max} = \max(\alpha/B, \beta/A)$; $\epsilon_{\max}$ is the square root of the reciprocal of the extinction ratio.

3 Eliminating zero-crossing error

Beck [1] observed that the zero-crossing error in the signals $S_1 \pm S_2$ (see (4–5)) could be eliminated by making the amplitudes of S_1 and S_2 equal. Since the amplitude of S_2 is smaller than that of S_1 by a factor of

$$k = \frac{1-r}{1+r},$$

this adjustment can be achieved by replacing S_1 with the attenuated signal $S_1' = kS_1$. Then (4–5) are replaced by the sum and difference of the equal-amplitude signals S_1' and S_2,

$$S_1' \pm S_2 = k(AB - \alpha\beta)(\sin d \pm \cos d), \tag{6}$$

and these signals exhibit *no zero-crossing error due to polarization mixing.*

In practice, replacing S_1 by S_1', a signal whose amplitude equals that of S_2, corresponds to adjusting a potentiometer while observing the signals on an oscilloscope screen. What is the effect on zero-crossing accuracy of an error in this calibration?

After some analysis, we find that the zero-crossing phase-angle error corresponding to 100η per cent error in setting the amplitude of S_1' equal to that of S_2 is

$$\tan\delta \approx \frac{\eta}{2}. \tag{7}$$

For example, a calibration error of 1% corresponds to a phase-angle error of $\delta = 0.29°$; an error of 0.2% corresponds to an error of 0.06°.

To provide an interpretation of (7), note that $\tan\delta \approx \delta$ for small (radian) values of δ. Converting radians to degrees yields the approximate relation $\delta \approx \eta/115$, where δ is the zero-crossing phase-angle error due to a proportionate miscalibration of η in setting the amplitude of S_1' equal to that of S_2.

4 Conclusions

Earlier work [3] demonstrated the superior tolerance of single frequency interferometers to polarization mixing errors; see table 1. Using Beck's suggestion, a simple amplitude adjustment can reduce even that residual error to zero.

Zero-crossing error due to polarization mixing can indeed be eliminated from the single frequency interferometer, and the necessary amplitude adjustment is quite resistant to calibration error.

Acknowledgment

The authors thank Vernon Beck for suggesting the amplitude adjustment described in this paper.

References

[1] V. Beck, private communication

[2] N. Bobroff, Residual errors in laser interferometry from air turbulence and nonlinearity, *Appl. Opt.* **26**(13) (1987), 2676-2681

[3] W. Augustyn and P. Davis, An analysis of polarization mixing errors in distance measuring interferometers, *J. Vac. Sci. Technol. B* **8**(6-Nov/Dec) (1990), 2032–2036

Research on Laser Length Standards in the Precision Engineering Division, NIST

Jack A. Stone*, Shen Zushan, and Alois Stejskal*****

*National Institute of Standards and Technology, Gaithersburg, Md 20899.
**Shanghai Institute of Metrological Technology, 1227 Chang Le Road, Shanghai, China.
***Institute of Scientific Instruments, Brno, Czechoslovakia.

Introduction: The Dimensional Metrology Group of the Precision Engineering Division, NIST, is involved in several projects developing new laser sources to serve as practical length standards. In this paper we report on one project nearing completion-- a new design for an iodine stabilized 633 nm He-Ne laser-- and will present preliminary results from a second project-- a new method of stabilization for a commercial green He-Ne laser. The first project was carried out by Jack Stone (NIST) and Shen Zushan (Shanghai Institute of Metrological Technology). The second project is a collaboration between Alois Stejskal (Institute of Scientific Instruments) and Jack Stone.

The Iodine Stabilized Laser: The iodine stabilized He-Ne laser operating at 633 nm has become the *de facto* standard for realization of the meter in the visible spectrum. It is used either directly for ultra-precise interferometric length measurements or, more commonly, as a standard for calibrating the vacuum wavelength of other types of stabilized He-Ne lasers (such as Zeeman stabilized lasers) that are used in commercially available interferometer systems. We have redesigned the iodine stabilized laser and integrated it into a system for automated wavelength calibration of other He-Ne lasers. The motivation here is to produce a system that is reliable and easy to use, and thus to promote more widespread use of this fundamental standard.

Our new design is based closely on a previous NIST design[1]. We have added a computer to automate operation and to replace a storage oscilloscope used previously to display the absorption spectrum, and we have redesigned the mechanical structure of the laser resonator. The basic signal processing electronics are unaltered except for updating of a few integrated circuits, and the optical arrangement is similar to the old design. A detailed description of the old design can be found in reference 1.

The mechanical structure of the laser cavity has been redesigned to make it as rigid and stable as possible without significantly increasing the difficulty of fabrication. It has performed well thus far. Only very minor re-adjustments of the alignment have been required to optimize power. The laser maintains its lock well in moderately noisy environments and need not be operated on an optical table. The optical length of the (Super

Invar) cavity increases by 3 parts in 10^7 per °C increase in ambient temperature. The servo can accomodate a temperature change over a range of roughly 4°C without the need for re-locking.

Operation of the laser is significantly enhanced by computer control. The primary purpose of the computer is to automatically lock to one or a series of the seven iodine absorption lines within the tuning range of the laser. In addition to automatically locking to a selected hyperfine transition, the computer maintains or enhances the diagnostic capabilities and flexibility of operation of previous designs. The program provides an intuitive graphical user interface for control of the laser. It performs a number of functions-- display of the absorption spectrum, automatic identification of lines and locking, diagnostic displays, monitoring for error conditions such as loss of lock, and control of a frequency counter to provide fully automated calibrations of other He-Ne lasers. A 20 MHz lap-top computer is entirely adequate for these tasks.

We have developed a robust algorithm for identifying and locking to selected iodine absorption peaks. We have found that the automatic peak identification algorithm is significantly more reliable than is manual operation used with previous designs, particularly for locking to lines in the middle of the multiplets (i, f, or e). We have carried out well over 1000 locks and misidentified a line on only one occasion. Improper setup of the laser can sometimes result in a failure of the locking algorithm to unambiguously identify a particular absorption line; this may cause the program to halt and issue an error message but it will not result in an erroneous line identification. Ample diagnostics are provided so that any problems with peak identification will be immediately discovered if an operator is present to observe the locking process.

The ability to detect a failure in the locking system and initiate appropriate corrective action is a valuable convenience when working in a noisy environment, where the servo lock may occasionally jump from one line to a neighboring line or the lock may be lost altogether. These problems are detected in our design by checking for sudden changes in servo voltage to the PZT. Reading of the servo level is accomplished by a background DMA process, leaving the computer free most of the time to perform other functions such as control of a frequency counter or other instruments.

The laser is primarily used as a standard for determining the frequency and thus the vacuum wavelength of other lasers via heterodyne comparison. With the addition of a GPIB-controlled frequency counter, the automated control is a great convenience for long studies of laser stability; if lock is lost for any reason, the laser automatically re-locks to the proper line before continuing to monitor the heterodyne beat frequency. In addition, the ability of the laser to alternate lock repeatedly between two lines is a useful feature for frequency calibrations. Any faults in the frequency comparison become obvious if the beat frequency between the two lasers is measured twice, locking first to one line and then to another. By measuring the frequency repeatedly while locking alternately to two lines, the test can detect errors in the frequency counting even if they are significantly smaller than frequency drifts of the laser under test.

Stabilization of a 543 nm He-Ne Laser: We are studying possible methods for stabilization of commercially available green He-Ne lasers with internal mirrors. In recent years these lasers have been stabilized by a variety of techniques[2], but here we are investigating an alternate method that may be well suited to commercially available green lasers, which typically operate with three TEM_{00} modes simultaneously lasing. A single-frequency beam can be isolated from the output using a polarizer.

It is well known that the frequency separation of adjacent modes depends on the position of the modes under the gain curve, due to frequency pulling. The intermode beat can therefore be used to stabilize a laser. With three modes lasing, two beat signals between adjacent modes are produced, and it is possible to generate a signal at the difference in frequency between these two beats; an inexpensive photodiode views light from the rear laser mirror, and the signal from the diode is mixed with itself to obtain the difference signal. The difference signal is typically on the order of a few kHz and varies in a complex manner as the laser length is tuned through 1 order. Figure 1 shows the variation in the difference signal frequency as the laser is cooled, causing the length of the cavity to decrease by about 2 orders. (In some regions no difference signal was recorded either because only two modes had significant intensity or because the frequency was too high to be passed by an amplifier in the system.)

Stabilization is achieved by servoing the length of the laser so as to keep the difference signal frequency equal to a constant reference frequency. The two frequencies are compared by using an up-down counter in conjunction with a circuit that eliminates simultaneous up and down pulses. The output of the counter is fed into a DAC and high-voltage amplifier to drive a PZT glued to the exterior of the laser tube.

The stabilization method described above produces an unmodulated output. If a small frequency modulation of the output is acceptable, it is also possible to stabilize the laser by applying a modulation to the PZT and locking to a local extremum of the curve in figure 1.

We have achieved a tight servo lock with potentially good wavelength stability of the output. Under closed loop control the difference signal frequency fluctuates about the reference frequency by about 4 Hz (1 second Allan variance). The corresponding variations in the laser vacuum wavelength, as inferred from the open-loop response of the system, would be on the order of a few parts in 10^{10}. We have not yet made a direct measurement of the actual wavelength stability, which may be significantly worse than the value indicated by the servo response. Additional studies in progress will be required to determine if this stabilization method is a viable alternative to methods already in use.

Acknowledgements: Development of the iodine stabilized laser was funded in part by the Lockheed Corporation. We would like to thank Dr. Howard Layer for many useful discussions in the early stages of the project.

References:

1. Howard P. Layer, IEEE Transactions on Instrumentation and Measurement, **IM-29**, 358 (1980).

2. H. Simonsen and O. Poulsen, Appl. Phys B **50**, 7 (1990) and references therein; J. M. Chartier, S. Fredin-Picard, and L. Robertsson, Optics Communications **74**, 87 (1989) and references therein; Jow-Tsong Shy and Chun-Ru Yang, Appl. Optics **28**, 4977 (1989).

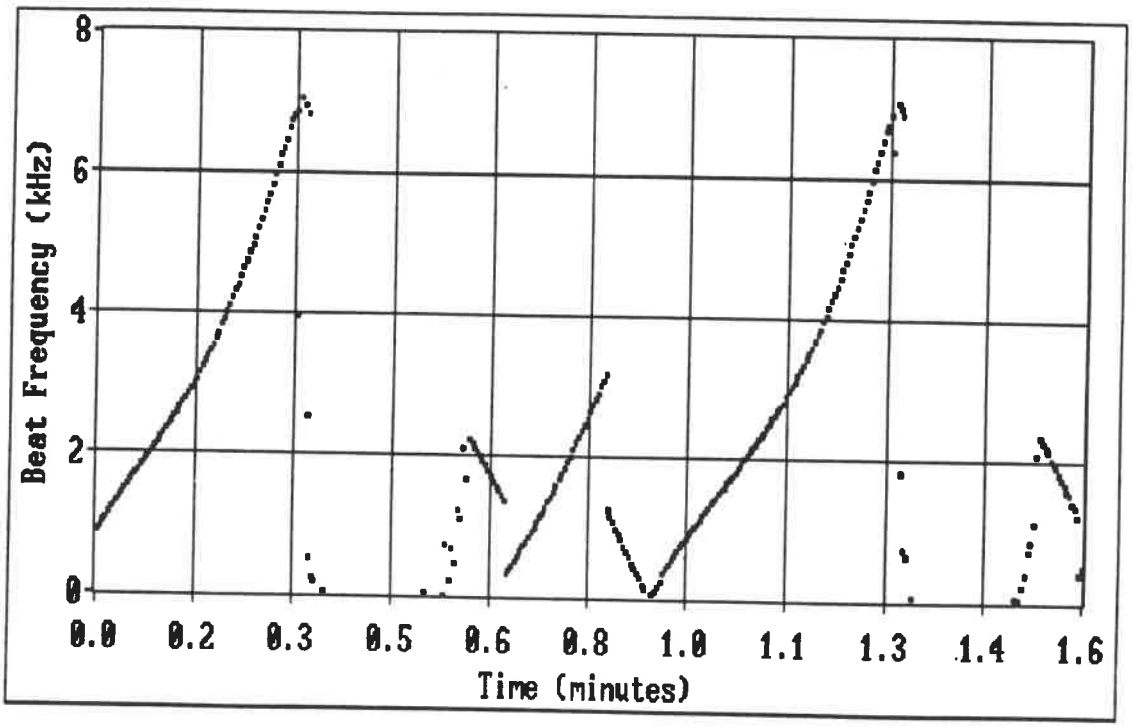

Figure 1. Frequency of the difference signal as a function of time, as the cavity is cooled and thus decreases in length.

INTERFEROMETRIC MEASUREMENT OF ROTATING TEST-PIECES

Anthony E Gee

School of Industrial & Manufacturing Science (Bldg 40)
Cranfield Institute of Technology
Cranfield, Bedford, MK43 0AL, UK

1 Introduction

To orientate test pieces on a high-accuracy spindle (of a single-point diamond turning machine) without the need for a datum facing cut, measurement of out-of-true running of the face-plate and workpiece was required. Methods considered included techniques such as capacitance micrometry[1] at three points around an outer annulus of the chuck face-plate but optical interferometry offered the facility to monitor the full aperture and the form of the work-piece from a convenient stand-off distance.

An axially mounted interferometer was employed to provide in-process monitoring and dynamic measurements of the spindle/work-piece run-out in three extraneous degrees of freedom contributing to axial motions[2].

When a test-piece is rotated about an axis close to the optical axis of the interferometer, in general it is observed that the resulting fringe patterns rotate at non-constant rate, manifesting cyclic changes of pitch. Fringe pattern rotations may be full- or part- revolutions, in the latter case, oscillating between pro- and contra- rotation.

2 Interferogram Dynamics: Analytical Aspects

Interferometry with a static test-piece may be readily visualised from the inclination between recombined wavefronts from the test-piece and reference surface. The general mutual inclination of the wavefronts generates an overall fringe spatial carrier-frequency and, superimposed upon this, local changes of slope cause modulation of the frequency and orientation of the fringes. The direction of the wavefront slope is indicated by the 'fall-line', the vector of maximum slope (orthogonal to the fringe-alignment). In static interferometry the fall-line is invariant for a particular setting and may be adjusted by changes of tilt; with the test-piece rotating, the pattern generally rotates also.

It was found that understanding of the dynamic interferometry of a rotating test-piece and adjustment of the interferometer were aided considerably by visualising the interferogram as being generated by the inclination of the wavefront normals, describing vectors defining the wavefront surfaces; on these the effect of the (spindle) axis of rotation could then be superposed. Further, the motions of the wavefront normal vectors could be seen to prescribe the motion of the point spread functions generated by their respective beams in the focal plane.

3 Special Cases of Interferogram Dynamics

Before analysing the general dynamic case, there are several special cases which lend themselves to understanding by application of static interferometry. A start-point is the case of normal adjustment of a plane-mirror interferometer with its axis aligned with that of the spindle.

Taking this as Special Case 1, fringes of infinite width will be generated and, across the finite width of the instrument aperture, uniform intensity will be observed, the intensity level being dependent on the relative phase relation occurring at wavefront recombination in the interferometer. When the spindle rotates, (ie about a constantly aligned axis), the effect will be to rotate the plane test-mirror about its normal, causing no change in optical conditions and thence no change in the interferogram.

If now the interferometer reference beam is inclined with respect to the spindle which carries the test-piece (ie to Special Case 2), parallel equispaced fringes will be observed but rotation of the spindle will cause no further optical change and so the observed fringes remain stationary.

Reverting to Case 1, from the all-normal alignment condition, Special Case 3 may be set-up. This arises where the test-piece is tilted so that its normal is now inclined with respect to the (parallel) axes of the spindle and of the interferometer reference beam. Since the test-piece tilt is made on-board the spindle, when the latter rotates the inclination vector does likewise and so rotating fringes of constant pitch will be observed.

Special Case 4 is a combination of cases 2 and 3 and is illustrated in Figure 1. Here, both the spindle and test-piece are independently tilted by the same angle, so that at one point in the rotation of the spindle [Figure 1(a)], the two will cancel causing infinitely wide fringes. At 180° arc spindle rotation from this [Figure 1(c)]), the two tilts will sum and so fringes of twice the inclination and half the pitch will be observed. At the intermediate (90° and 270°arc) positions (Figure 1(b) and 1(d)], the vectors describing the tilt of the spindle and of the test-piece will be at 90°arc to each other and, summing them, they will together cause a tilt of $1/\sqrt{2}$ of the maximum tilt [in (c)]. The resultant fringe angle will be the median of the equal contributing tilts ie $\pm$45°arc either side of the maximum tilt condition (c).

4 General Interferogram Dynamics

To describe the general case, where the fringe-pattern both changes pitch and rotates (either fully or partly), it is useful to consider the actions of the optical point spread functions at the focal plane[3], with respect to the spindle axis as shown in figures 2 and 3.

The spindle axis intersects the focal plane at A (symbol o), the reference wave at R (symbol +) and the test-wave at T (symbol x). Vector **AR** is the static offset tilt of the interferometer reference axis with respect to the spindle. **AT** defines the instantaneous magnitude and direction of tilt of the test-piece with respect to the spindle axis and so rotates with the spindle. The third (resultant) vector **RT** has the direction and magnitude of the tilt of the test-piece axis with respect to the reference axis and so defines the observed fringe pattern.

Viewed axially as in Figure 3, if R lies within the circular locus of T about A as shown in Figure 3(a), **RT** will rotate continuously in the same direction as the spindle but with cyclically varying angular rotation-rate and length, with corresponding effects on the rotation and spatial frequency of the fringe pattern. If, however, R lies outside the circular locus of T about A as shown in Figure 3(b), then **RT** and the fringe-pattern will oscillate, between some maximum values of angle θ with respect to the median (and, incidentally, causing the fringe-pattern to contra-rotate with respect to the spindle for half of each spindle-revolution).

The foregoing may be used to explain the special cases derived in section 3, (identifiable with conventional static interferometry). Case 1 in Section 3 is that where A, R and T coincide; the test-piece fringe pattern tilt vector **RT** is then zero for any rotational position. In Case 2, only T and A coincide, **RT** is finite but T does not move. Case 3 causes R and A to coincide, so **RT** rotates with constant length. Case 4 causes R to lie on the circular locus of T, [eg at T_a in Figure 3(a)] so infinitely wide fringes are observed when T coincides with R there, [the condition of Figure 1(a)] and closest-spaced fringes at 180° arc motion from this (when T is at T_c) as in Figure 1(c). At the 90°arc and 270°arc rotational points, (when T is at T_b and T_d, **RT** will be at $\pm$45°arc with fringes likewise inclined, as in Figures 1(b) and 1(d).

5 Application-modes

Dynamic rotating interferometry may be used to set-up surfaces to be machined, to metrologically qualify rotating spindles and to test and centre the form of rotating artefacts.

With a suitable reference surface and light-source optics, rotating conic-section test-surfaces may also be tested; motions in radial degrees of freedom are then also manifest. Provision must be made for tilt and centring adjustment of the rotating test-surface as appropriate.

6 Acknowledgements

This paper arose as part of a programme of research into fine machining in collaboration with Prof Keith Puttick of the Dept of Physics, University of Surrey, Guildford, UK. Support for realising instrumental concepts and which led to this paper was provided by the Paul Instrument Fund administered by the Royal Society of London. Professor Robert C Spragg of the School of Industrial and Manufacturing Science, Cranfield Institute of Technology, is acknowledged for helpful advice on machine monitoring and roundness metrology.

References

1 R V Jones and J C S Richards, J Phys E:Sci Instrum vol6 pp589-600 (1973)

2 A E Gee, S G McCandlish and K E Puttick, Proc SPIE vol1015 pp74-80 (1988)

3 A E Gee, in J C Dainty (ed), "Applied Optics Digest" (Proc Conf on Applied Optics and Optoelectronics, Nottingham, Sept 1990) pp109-110, IOP, Bristol (1990)

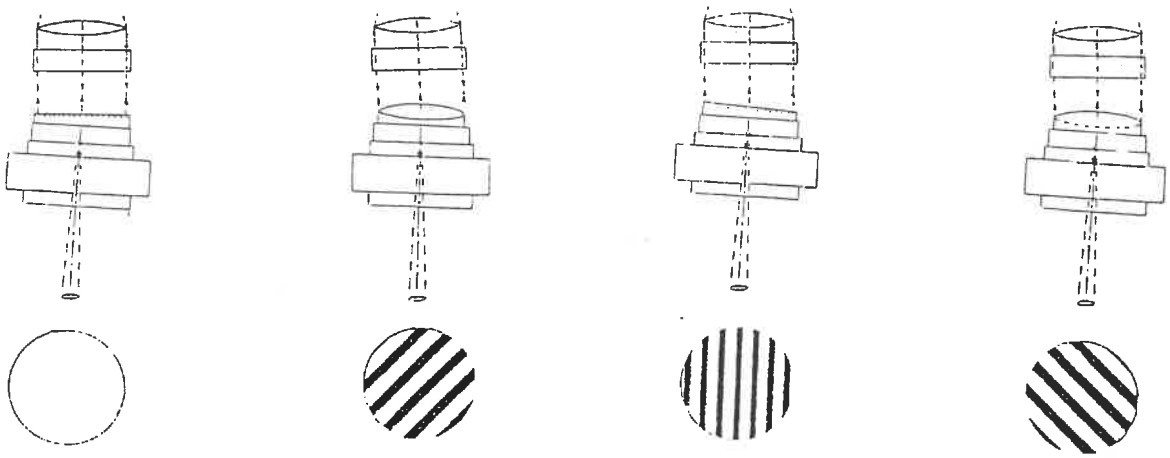

(a) @0 deg arc Rotation

(b) @90 deg arc Rotation

(c) @180 deg arc Rotation

(d) @270 deg arc Rotation

Figure 1 'Special Case 4': Equal Inclinations of Spindle and Workpiece

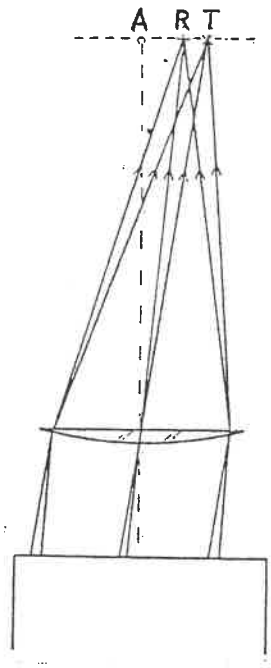

Figure 2: Interferometer Beam Focussing, (offset from Spindle Axis)

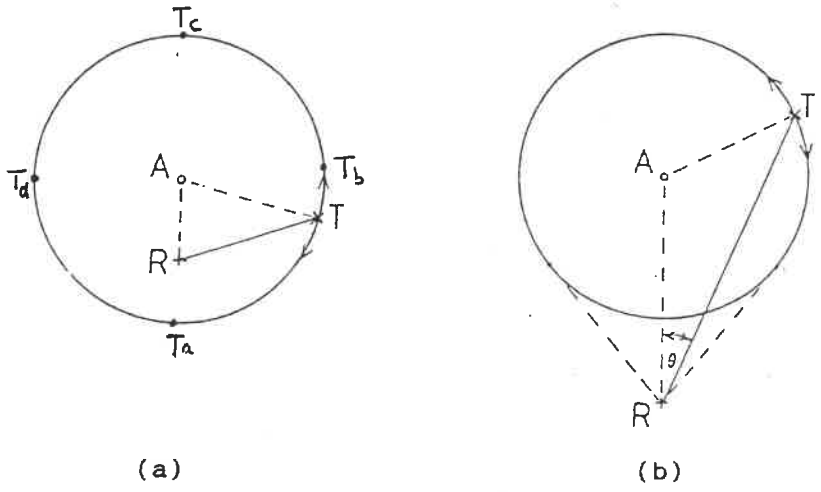

Figure 3 Locus of Offset Interferometer Foci with respect to Spindle Axis

Differential Interferometry for On-Process Aspheric Metrology*

L. Curt Maxey
Optics MODIL, Oak Ridge National Laboratory
Oak Ridge, TN 37831

Introduction

Various methods exist for certifying the figure quality of precision aspheric mirrors. Traditionally, null testing configurations, such as the autocollimating test for paraboloids and the Hindle test for hyperboloids, are employed whenever possible. More demanding applications often require the construction of a carefully designed corrective optical system (or "null lens") employing refractive, reflective [1], and/or diffractive [2] optical elements.

The use of specialized test systems and the need for precision multiaxis alignment control usually confine aspheric figure measurements to a dedicated metrology laboratory. However, on-process aspheric metrology is sometimes needed in more challenging environments. For example, the task that prompted this interest in differential measurements will require on-process metrology of aspheric optical surfaces during final figuring in an ion milling vacuum chamber. The usual methods for applying aspheric metrology in the laboratory are often very difficult to set up and align for on-process measurements and may use resources that cannot be committed to a specific task.

As an alternative, less sophisticated systems can be used to accurately measure the change in figure of an optic with little attention to the absolute figure quality. When the figure change (rather than the absolute figure) is the quantity of interest, or when the figure can be initially characterized off-line, this alternative can be an effective solution to on-process measurement problems. In addition, extraneous aberrations introduced by viewing windows, self-weight distortion, or fixturing effects can usually be stored as a part of the reference measurement and (for an equilibrated system) do not appear in the differential measurement data. Three differential measurement strategies are being considered for on-process metrology at the Optics MODIL.

Measurement Concept and Methods of Implementation

Depending upon the measurement requirements, differential interferometric measurements can be implemented using phase map subtraction, interferogram subtraction, or holographic interferometry. In each case, the asphericity is partially compensated, and a combination of interferometric and/or image processing techniques are applied to measure the change in the optic. Partial aspheric compensation is achieved by using a simple null lens system so that the optic can be observed interferometrically from its center of curvature. The null compensator designs are based on standard null lens concepts but do not require the level of effort necessary to develop and align an accurate null lens. In preliminary experiments using singlet designs based on the Dall corrector, paraboloids as fast as f/2.3 have been compensated within one wave with only moderate attention to alignment.

*Research sponsored by the Strategic Defense Initiative Organization, through the Industrial and Operational Interfaces Directorate, Producibility and Manufacturing Division, under Interagency Agreement No. 1855-1562-A1 under Martin Marietta Energy Systems, Inc., contract DE-AC05-84OR21400 with the U.S. Department of Energy.

Phase map subtraction - The simplest method of applying differential interferometric measurements is through the algebraic subtraction of individual phase maps generated using interferogram analysis software. The difference map will reveal any figure change along with any alignment shift or other aberrations introduced between the acquisition of the two data sets. In principle, the measurement resolution should be limited only by the repeatability of the interferometer.

In this implementation, the differential change in the optic is not revealed until the phase maps are subtracted. For complex surfaces, it can be very difficult to intuitively interpret the change in the optic until the phase maps have been subtracted. For applications requiring rapid, intuitive feedback of figure change information, this implementation is probably not suitable. Lack of intuitive feedback also makes alignment shifts difficult to detect and correct prior to phase map generation. Subtraction of alignment errors in software may introduce secondary error sources [3].

Interferogram subtraction - Unlike phase map subtraction, interferogram subtraction provides live video monitoring of changes in the figure or the alignment of the test optic. The resulting differential interferogram can be visually interpreted or further processed for computer analysis.

Differential measurements are obtained by first storing a reference interferogram that contains a large tilt component. The tilt component serves as a carrier that can be removed later. This reference is subtracted from subsequent interferograms, revealing any change in the optic. Unless changes are present, the result is a perfect null interferogram, regardless of the actual figure of the optic. Any change in the figure or alignment of the optic produces interference fringes. The fringes that are obtained, although synthesized by the image processing operation, can be treated as true interference fringes in every respect. Phase shifting techniques can be applied by subtracting the stored reference from subsequent phase-shifted interferograms.

The tilt carrier is removed before computer analysis of the differential interferogram by spatially filtering the image. Uncompensated aberrations in the optic cause variations in the spatial frequency of the interferogram, making the carrier more difficult to remove. Thus far, the filtering achieved through Gaussian convolution of the image has worked well with uncompensated aberrations of one or two waves. More sophisticated image processing may be required if several waves of aberration remain in the interferogram.

In interferogram subtraction experiments to date, the results have been limited by a noise floor of about a tenth of a wave in what should be null phase maps. Efforts to identify the sources contributing to this noise floor are currently under way.

Holographic interferometry - The degree of aspheric compensation required for differential measurements is substantially reduced if the reference interferogram is recorded holographically rather than electronically. In this implementation, an interferometer is being configured so that the amount of tilt in the reference arm of the interferometer can be increased to several degrees and a holographic record of the test arm wavefront can be preserved. This allows the reference wavefront to be diffractively reproduced and interfered with the test arm wavefront to reveal any changes in the test optic. The presence of several waves of uncompensated aberrations are not expected to compromise the differential measurements.

Holographic interferometry requires accurate alignment of the diffracted wavefront reference with the test arm wavefront. A prototype system is being developed using a thermoplastic recording camera that allows the hologram to be processed in situ. The holographic interferograms may be phase shifted and processed using conventional phase analysis algorithms to achieve high-resolution differential measurements. By enabling the immediate measurement of figure change

without additional image processing techniques this approach offers the most direct approach to differential figure metrology, reducing the number of intermediate processes that might erode the measurement resolution.

Discussion

Our differential interferometric figure measurement research is initially being limited to the measurement of conicoids, which can be initially characterized in the metrology lab using null testing configurations. The aspheric experiments conducted thus far have been limited to concave paraboloids, as they are relatively easy to compensate using the Dall compensator. The Offner compensator and other designs are under study for the measurement of other conicoids. Convex optics mandate the use of large auxiliary optics that, for on-process differential measurements, need not be of the quality required for accurate null testing.

Because of its simplicity and lack of intermediate image processing steps, the direct subtraction of phase maps, is an approach that will be used for some on-process measurement applications. Efforts to maintain alignment integrity between data acquisitions will be emphasized to reduce the number of secondary error sources.

Interferogram subtraction can be implemented using a primitive interferometer and simple image processing techniques. The live video feedback achieved with this simple approach make it useful for applications such as on-process monitoring to avoid distortion due to part fixturing. It also provides a method for verifying alignment integrity during phase map subtractions.

Despite the complexity of the hardware, holographic interferometry has compelling advantages for measuring figure change during ion milling processes. In particular, it is expected to reduce the precision required in the aspheric compensation (which must include the effects of the viewing port) and the alignment of the test optic. Reducing the quantity and the complexity of positioning systems required in the vacuum vessel, helps contain the cost and improve the reliability of the ion milling apparatus.

References

1. Optical Shop Testing, Ed. Daniel Malacara, John Wiley and Sons, New York, 1978.

2. S. M. Arnold, "How to test an asphere with a computer generated hologram", in *Holographic Optics: Optically and Computer Generated*, SPIE Vol. 1052, pp. 191-197 (1989).

3. C. J. Evans and W. T. Estler, "Some observations on the performance of commercial phase measuring (Fizeau) interferometers used in surface figure metrology", *Proceedings from ASPE 1991 Annual Conference*, ASPE Vol. 4, pp. 54-57 (1991).

Precision Figure Metrology For Fabrication Of The AXAF Mirrors

D.A. Zweig
Hughes Danbury Optical Systems, Inc.
100 Wooster Heights Rd.
Danbury, CT 06810

Introduction

The Advanced X-Ray Astrophysics Facility (AXAF) is the next telescope in NASA's Great Observatories Program. The x-ray telescope contains six pairs of paraboloids and hyperboloids; each pair constructed as a Wolter Type I grazing incidence telescope. Each element in the telescope is approximately 35 inches long and ranges in diameter from 592 to 1225 millimeters. The focal length of the assembled telescope is 10 meters.

The cylindrical geometry of the optics combined with their long focal lengths require the use of nonconventional metrology techniques. HDOS has demonstrated the ability to generate two dimensional surface maps by combining profilometry in the axial direction with profilometry in the circumferential direction. This paper will described the metrology strategy and operation of the Precision Metrology Station which is used to measure the axial figure of the AXAF optics.

Axial Figure Metrology

The measurement of axial figure is performed by the Precision Metrology Station (PMS) This station is designed to measure sag and figure errors with spatial frequencies in the range of 0.001 to 1 cycle per millimeter. The requirement for measurement uncertainty over the spatial bandwidth of operation is less than 38 Å RMS. The distribution of errors as a function of spatial frequency is described in a power spectral density function with is shown in Fig. 1. The requirement for a measuring sag is an uncertainty of less than 222 Å.

The measurement technique employed by the Precision Metrology Station is analysis of the interference pattern produced in a scanning Fizeau interferometer which is shown schematically in Fig. 2. The optic under test is placed in close proximity to a reference surface and illuminated with a collimated laser beam. The illumination is partially reflected at both the reference surface and the surface under test. The reflected light is imaged onto a detector which measures the change in intensity resulting from the interference between the two beams. The laser illuminator and the detector are mounted on an air bearing assembly which travels the length of the reference surface (approximately 40 inches) measuring the optical path difference between the test surface and the reference surface. By placing a wedge between the two surfaces a nearly periodic fringe pattern is produced. The deviation from a truly periodic pattern is a measure of the deviation between the surfaces. The measured fringe pattern is analyzed to determine the true surface of the optic under test.

Fringe Pattern Analysis

A new fringe-pattern analysis algorithm was developed for use with the Precision Metrology Station. The algorithm is fast, accurate and efficient in its use of data. The concept behind this algorithm is to treat the interference pattern as a frequency modulated signal encoded into a carrier. In the case of an interference pattern the carrier is the fringe pattern generated by tilting the test optic with respect to the reference surface. The algorithm makes use of the property that the Hilbert transform of a quasi-sinusoidal function is the phase quadrature function. The ratio of the Hilbert transform of the measured intensity and the measured intensity is the arctangent of the optical path difference between the test optic and the reference optic.

The Hilbert transform algorithm has a number of advantages over the more classical fringe location techniques. The most significant advantage demonstrated is the accuracy with which optical path differences are reconstructed from the fringe pattern. Computer simulations demonstrate sub-angstrom level reconstructions over large spatial frequency bandwidths. Angstrom level repeatability has been experimentally demonstrated using the Hilbert transform algorithm.

A second advantage of the Hilbert transform algorithm over fringe location techniques is that unlike fringe location techniques, the Hilbert transform produces the same number of surface values as intensity measurements with the same data spacing. This property eliminates the need for interpolation and yields reconstructions with high sampling rates.

Calibration Strategy

The metrology strategy employed in measuring the axial figure of the AXAF optics is to construct and calibrate a toroidal reference surface. The reference surface is constructed from Zerodur and its radii of curvature are designed to accommodate all 12 AXAF optics. The calibration is performed with the reference surface mounted *in situ* using the Precision Metrology Station to perform the measurement. The *in situ* calibration incorporates all systematic, repeatable error sources associated with the Station. The master reference surfaces for this calibration process are a set of three 10 inch diameter Zerodur flats. The flats are calibrated by a three-flat test using a fringe-scanning interferometer which was developed for the Technology Mirror Assembly (TMA) program (the technology demonstration which preceded the fabrication of the AXAF optics). The three-flat test results in the absolute figure measurement along a line for all three flats, two of which are used for calibration of the toroidal reference surface.

The toroidal reference surface, which is 40 inches in length, is calibrated against a reference flat over 8 inch sub-apertures. The 10 sub-aperture measurements, each of which overlaps the neighboring sub-apertures by four inches, are stitched together to produce a full-length calibration of the toroidal reference surface. The measurements are repeated for the reference surface pitched at different angles with respect to gravity. The different pitch angles of the reference optic are

necessary to bring it close proximity with the full array of AXAF optics which vary in cone angle between 0.45° and 2.57°. From the ensemble of measurements a calibration file is calculated which accounts for the gravitationally-induced figure changes.

Verification Strategy

The accurate calibration of the Precision Metrology Station is essential for the successful fabrication of the AXAF optics. The accuracy is limited by the accuracy with which the station is calibrated. The ensemble of calibration measurements are analyzed for self-consistency and for consistency with models of the reference surface under a gravitational load. In addition a number of independent cross checks are employed to verify the station calibration. As a coarse cross check of low frequency accuracy, the figure of an AXAF optic is measured on the Precision Metrology Station and the Mechanical Profilometry Station (MPROS). (The Mechanical Profilometry Station is used for course measurement of the AXAF optics during grinding and early stages of polishing.) The accuracy of the Mechanical Profilometry Station is an order of magnitude worse than that of the Precision Metrology Station, however, this comparison can identify gross errors in the calibration of low frequencies and sag.

A more accurate cross check of low and mid-frequency calibration is obtained through a shear test. The shear test involves two separate measurements of an AXAF optic. For the initial measurement the optic is located in its nominal position in relationship to the reference surface. For the second measurement the AXAF optic is shifted along the axis by some distance. In differencing the two measurements the systematic error of the Station in each measurement cancels with itself leaving the optic surface subtracted from an offset optic surface, which is an estimate of the derivative of the optic surface. Integrating the difference of the two measurements results in a measure of the AXAF optic which is independent of the Station calibration measurement. The results of the shear test are then used to assess the accuracy of the calibration of the Station. The noise characteristics of the shear test limit its use to the measure of low and mid-frequency figure and precludes its use for the measurement of sag.

A third cross check which is employed is a flip test in which an AXAF optic is measured in both orientations with respect to the reference optic. Differencing the two measurements eliminates the systematic error of the Station yielding the figure of the AXAF optic subtracted from itself rotated 180 °. This differencing results in the canceling of even function optic surface errors and the doubling of odd function optic surface errors. The results of the flip test are also independent of the calibration of the Station and thus serve to assess its accuracy.

Results

The Precision Metrology Station has been used in the fabrication of the largest parabola and hyperbola (P1 and H1) of the AXAF telescope. The predicted figure uncertainty as measured by the Station is described by the power spectrum plotted in Fig. 1. The measurement uncertainty over the bandwidth of 0.001-1.0 mm^{-1} is less than 16 Å RMS -- far better than the 38 Å RMS requirement especially at low spatial frequencies. The predicted sag uncertainty of the Station is

less than 220 Å which consistent with its requirement of 222 Å. The calibration of the Station has been verified by the three cross-check methods described previously.

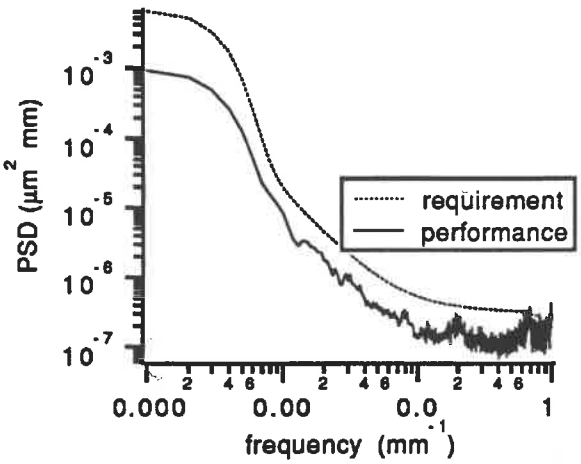

Fig. 1. Precision Metrology Station accuracy requirement defined by the power spectrum of allowable errors.

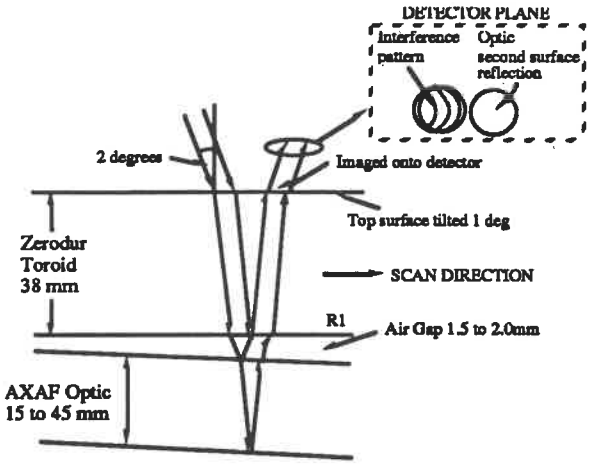

Fig. 2. Schematic of the scanning Fizeau interferometer.

Environmental Effects in the Testing of Large Astronomical Mirrors

H. M. Martin, J. H. Burge, S. C. West
Steward Observatory
University of Arizona
Tucson, AZ 85721

1. Introduction

We describe the optical testing of a 3.5-m f/1.5 parabolic primary mirror using phase-measuring interferometry from the center of curvature. A 2-element refractive null lens corrects the 250-micron peak-to-valley asphericity of the mirror. Measurements are made from a vibration-isolated tower which can accommodate mirrors with focal lengths up to 12 m. The thermal environment is controlled to reduce seeing and thermal figure distortions. The measurement accuracy, limited by vibration and seeing, is better than 10 nm rms surface error. We analyze the measurement accuracy in terms of the surface structure function (a measure of surface error as a function of spatial scale), the same quantity used to specify the figure error.

2. Status of Mirror Figure

The mirror specification is given by a surface structure function, the mean square difference in surface error between random points as a function of their separation in the aperture. The structure function is also used to describe the wavefront aberrations induced by the turbulent atmosphere (seeing) above the telescope. The specification for the 3.5-m mirror corresponds to 1/8-arcsecond FWHM image size.

Measurements were made with a commercial phase-measuring interferometer system. The final data are shown as a simulated interference pattern in Figure 1. The overall rms surface error is 21 nm.The directly measured interference patterns are subject to errors due to misalignment, imperfect illumination, vibration and seeing that are unrelated to the actual mirror figure. These are reduced by averaging in the final phase map, which is an average of 48 maps. An example of a directly measured interference pattern is shown in Figure 2.

The structure function was calculated from the phase map over the full measured aperture. The measured rms surface difference is plotted in Figure 3 along with the specification. The measured rms difference is less than the specification by at least a factor of 1.4 at all separations.

3. Environmental errors

Any single phase map contains random errors due to local air turbulence (seeing) and vibration. We have taken measures to reduce these effects, but at small levels they affect the measurement. Since the phase errors due to seeing and vibration are random, they are reduced by taking many

Figure 1. Wavefront reflected by the 3.5-m mirror, displayed as a simulated interference pattern calculated from the final surface map.

phase maps and averaging them together. A study has been performed to determine the magnitude of the random measurement errors.

The measurement of the random test uncertainties, like the figure specification, is expressed in terms of a structure function. The statistics of a representative sample of 16 phase maps (which were used in the final average) were analyzed to determine the effective structure function of the measurement errors. The calculated structure function based on this analysis is given in Figure 4. This plot, which shows the calculated effective structure function of a single phase measurement, corresponds to 28 nm rms surface error. Since this error is uncorrelated between maps, and since errors in the measured structure function add linearly rather than in quadrature, the error is reduced in proportion to the number of maps averaged.

Work is in progress to understand the sources of vibration and turbulence in the test tower.

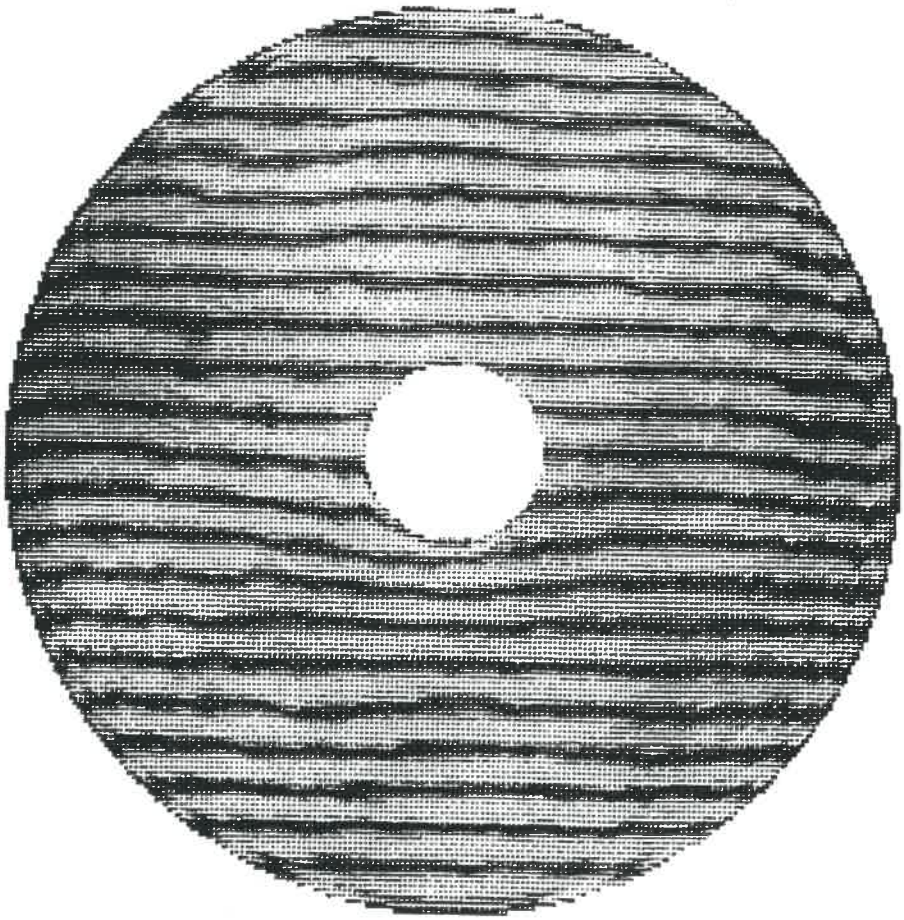

Figure 2. Measured interference pattern from the 3.5-m mirror. In addition to actual figure errors, this measurement is sensitive to errors of alignment, illumination, vibration and seeing.

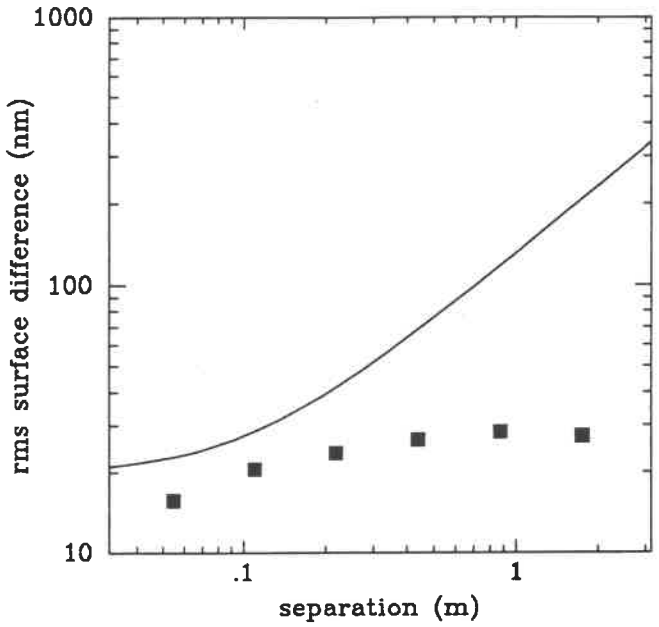

Figure 3. Square root of the surface structure function for the finished 3.5-m mirror (squares) and specification (curve). This quantity is the rms difference in surface height between random points as a function of their separation.

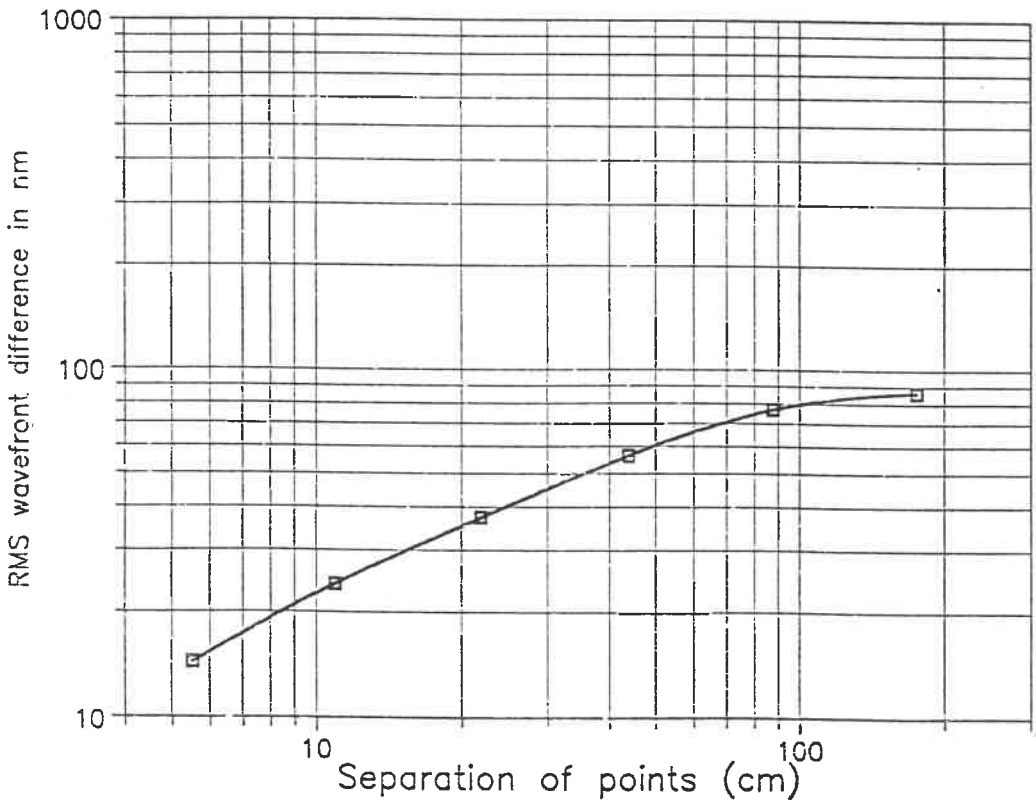

Figure 4. Square root of the wavefront structure function for testing errors in a single measurement.

Analysis of Cone Error in Off-axis Optics

Robert E. Parks* and Lianzhen Shao**

Introduction

It is common in diamond turning to incorrectly set the cutting tool position at the beginning of a cut. This tool set error introduces a conical figure error into the part being turned. The conical error is easily recognized and appropriate corrections are readily made when dealing with rotationally symmetric parts.

Diamond turning is particularly well suited for making off-axis optics as a part of a parent or rotationally symmetric piece. It is, however, just as easy (or even easier) to make a tool setting error with this geometry but more difficult to recognize the effect of the resulting cone error in the off-axis part. In this paper, we derive the shape of the cone error over the off-axis aperture for the case of a perfectly aligned part. It is shown that the cone error is a function of the tool offset, the distance to the center of the off-axis aperture, the diameter of the aperture and the vertex radius of the part.

We go on to show by what amount the tool must be adjusted laterally to remove the cone error during the next tool pass. Finally we show that the technique of recognizing cone error may be applicable to the optical testing of secondary mirrors in large astronomical telescopes. The technique would permit the use of a subaperture test while guaranteeing there is no significant cone error in the secondary mirror. The subaperture test would be many times less expensive to perform than a full aperture test.

Derivation of Cone Error

If the turning tool is not started (or does not finish) on the axis of rotation of the part, the center of curvature of the part being turned, instead of being a point on the axis, will be a circle concentric with the axis whose radius is equal to the offset of the start of the tool from the axis. The effect of this offset on the figure of the part is shown by expanding the first term of the series representing a (a)spherical part, namely,

$$z = \frac{(\rho \pm \delta)^2}{2R} + \cdots = \frac{\rho^2}{2R} \pm \frac{\delta\rho}{R} + \cdots$$

$$= \frac{\rho^2}{2R} \pm \alpha\rho + \cdots = \frac{x^2+y^2}{2R} \pm \alpha\sqrt{x^2+y^2} + \cdots \qquad (1$$

*Optical Sciences Center, University of Arizona, Tucson, AZ 85721
**Tucson Optical Research Corp., 210 S. Plumer, Tucson, AZ 85719

where α is the angle of the cone error, δ is the tool set error or offset and R is the vertex radius. Notice $\delta = \alpha R$.

While this cone error is easily recognized in rotationally symmetric parts, it is less obvious over an off-axis section of such a part. Consider the off-axis aperture of a rotationally symmetric part as shown in Fig. 1. When the base sag is removed, the coordinate system shifted to the center of the off-axis aperture and renormalized over that aperture, the figure is given by[1]

$$z_{cone} = \alpha\sqrt{x'^2+y'^2} = \alpha\left[(ax+h)^2+(ay)^2\right]^{1/2}$$

$$= \alpha h\left[1+\frac{a^2}{h^2}(x^2+y^2)+\frac{2ax}{h}\right]^{1/2} \qquad (2$$

where a is the radius of the aperture and h is the distance from the axis of the symmetric piece to the center of the off-axis aperture.

Since a and h are about the same magnitude in most cases, the last 2 terms in the brackets are not less than 1 and thus the radical cannot be easily expanded in series. However, the function in Eq. 2 may be evaluated over a uniform mesh and those height values fit with a 2-dimensional polynomial fitting routine such as FRINGE[2] to determine the form of the figure in terms of functions familiar to optical engineers. When this is done a figure such as that shown in Fig. 2 is obtained where the tilt and focus terms have been removed. The only non-zero terms are those asymmetric terms involving the cosine. The cosine 3θ term (3 cornered hat) is particularly evident and is symptomatic of cone error over an off-axis aperture.

To use this method for finding the cone error in off-axis optical parts, substitute values for a and h in Eq. 2 and evaluate the expression over a regular grid of points. Then determine the 2-dimensional polynomial coefficients representing the cone error over this grid. In a least squares sense, subtract this set of coefficients from the measured figure over the normalized off-axis aperture using α as a scaling factor. The figure of the part after the cone error has been removed is represented by the difference in the coefficients. The value of α times the vertex radius, R, give the tool offset, δ, necessary to physically correct the cone error.

Cone Error in Secondary Mirror Tests

Secondary mirrors for astronomical telescopes are normally tested using an optical null test named for Hindle. In this test that makes an aspheric secondary mirror look like a perfect sphere

requires a concave spherical mirror about the diameter of the primary mirror in the telescope and with a radius of curvature half that of the primary. For a large aperture telescope with a fast primary, this test optic can be as big and costly an undertaking as making the primary mirror itself.

On the other hand, a sphere about 3 times smaller in diameter could be used if the secondary were tested over an off-axis aperture that covered the region from the shadow of the obscuration to the edge of the secondary. This test that could save an order of magnitude in cost is seldom used because it has been believed to be insensitive to cone error. If a secondary were made that had cone error of magnitude α, the angular effect on the image quality of the telescope can be shown to be 4(pri dia/sec dia)α. Since 4(pri dia/sec dia) is about 1, the angular image error is about the same as alpha.

Using the analysis above, it can be shown that for typical large telescope geometries, the 3 θ error term is approximately equal to $\alpha a^3/8h^2$. Thus if the off-axis or subaperture Hindle test were sensitive to errors in this 3 θ term on the order of 20 nm, alpha could be determined to 1 microradian and thus the image quality degraded by no more than that due to cone error.

Of course, in performing the off-axis test, the secondary may not be aligned perfectly with the test optics. This misalignment will also produce error terms similar to those produced by cone error but in different ratios. For the same lateral offset, the 3 θ term increases about 100 times faster for cone error than for misalignment for typical f/#'s. Thus the cone error is easily separable from error due to misalignment.

Conclusion

We have illustrated a method of recognizing the effect of cone error (or tool set error) in diamond turned, off-axis optics. The magnitude of the tool set error is easily calculated. We have also shown that the sensitivity of the method is sufficient to preclude leaving performance degrading cone error in secondary mirrors tested using an off-axis Hindle test.

Acknowledgements

This work was performed under contract to NIST. One of us (REP) would like to acknowledge many useful discussions with Chris Evans while working at NIST.

References

1) R. E. Parks, Alignment of Off-axis Conic Mirrors, OF&T Workshop Notebook, Optical Society of America.
2) D. Anderson, FRINGE Manual, Optical Sciences Center, Univ. of Arizona, Tucson, AZ 85721.

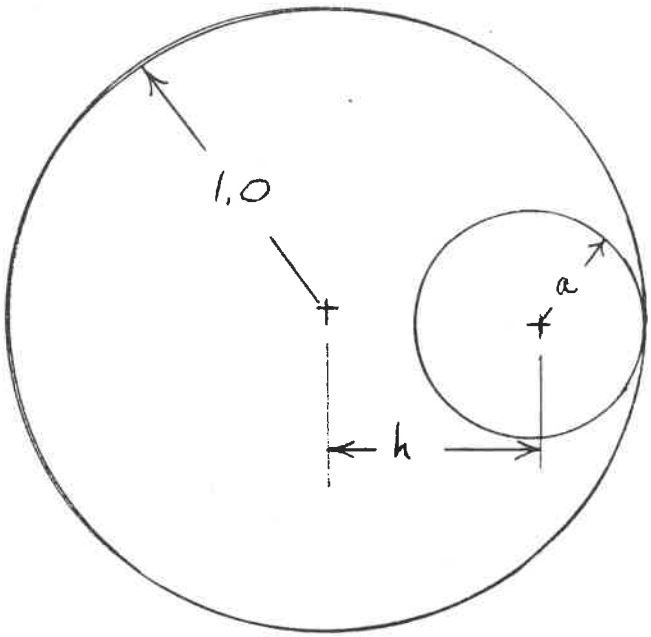

Fig. 1 Geometry of off-axis aperture relative to symmetric aperture

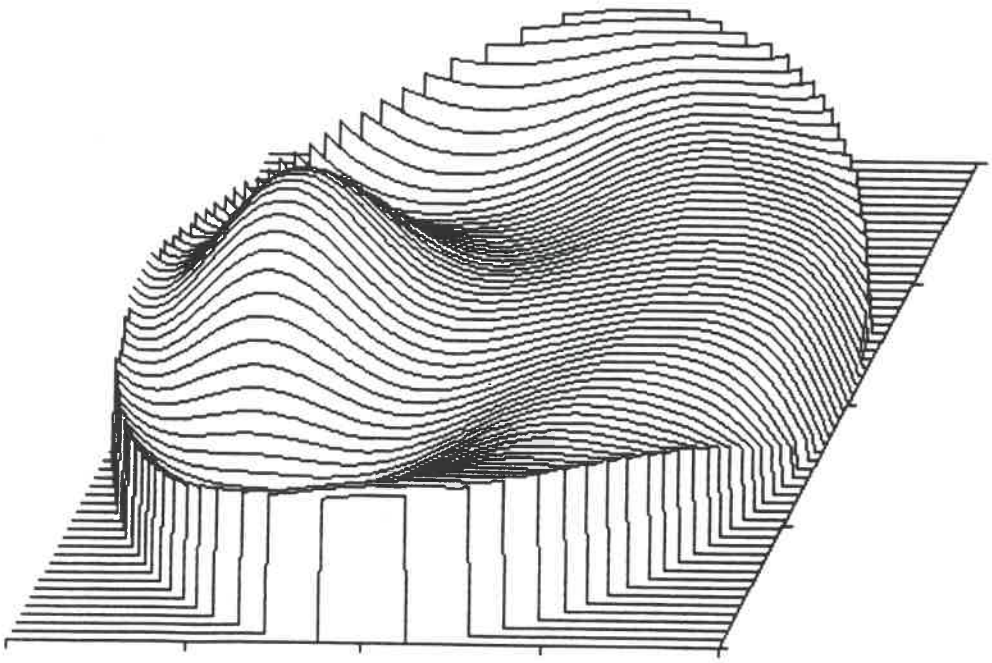

Fig. 2 Isometric view of figure due to cone error over an off-axis aperture. The axis of the symmetric aperture is to the left. The 3rd order astigmatism and coma have been removed to emphasize the 3 θ character of the remaining error.

TESTING CYLINDRICAL SURFACES: ALIGNMENT CONSIDERATIONS

Katherine Creath
Optical Sciences Center, University of Arizona
Tucson, AZ

and James C. Wyant
WYKO Corporation, Tucson, AZ

Cylindrical optical surfaces are hard to test because a cylindrical reference wavefront is necessary. A high-quality cylindrical wavefront can be generated using a grating designed so that an incident plane wave produces the appropriate cylindrical wavefront in the first diffracted order. An implementation of this technique for use in a collimated beam was presented by Hirst.[1] Figure 1 shows the setup for this technique. Interference fringes can be viewed on the screen. Both beams are diffracted from the grating. The test beam is diffracted by the grating and then reflected off the test surface and the grating. The reference beam is diffracted into the opposite order from the test beam. This technique is easy to implement in a shop; however, it can not provide quantitative data.

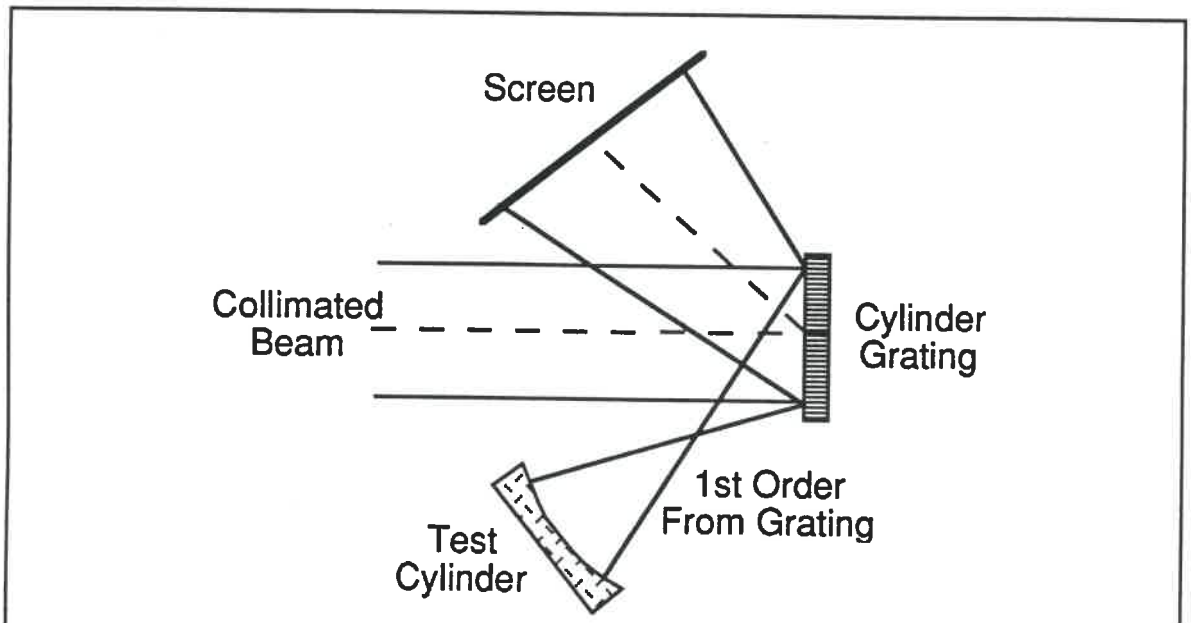

Figure 1. Hirst method for cylinder testing.

A phase-measuring Fizeau interferometer with a flat reference surface can be used to quantitatively test cylindrical surfaces. A reflective (or transmissive) grating is placed in the test beam to produce a cylindrical reference wavefront (see Fig. 2). Because a reflective grating will reflect the zero-order beam directly back into the interferometer, the grating needs to be designed so that it will produce a good cylindrical wavefront when tilted out-of-plane to remove the zero-order beam (see Fig. 3). The ideal shape for the grating lines may not be straight. Many lens design packages have the capability to design these kinds of gratings. Because the test beam is diffracted twice by the reference grating, any errors in the fabrication of the grating will be doubled.

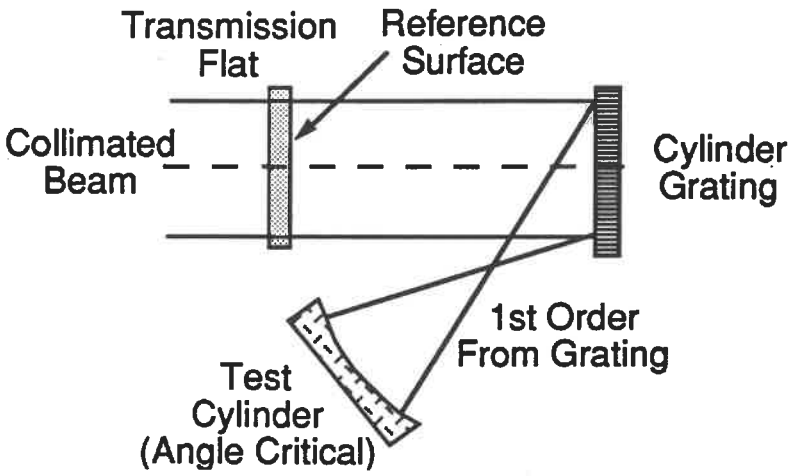

Figure 2. Cylinder testing using a Fizeau interferometer and cylinder grating.

The alignment of the grating is critical to produce a good cylindrical wavefront. There are two critical angular degrees of freedom for the alignment of the grating and one for the alignment of the cylindrical test surface. These degrees of freedom are shown in Fig. 3. The out-of-plane angular alignment of the grating (rotating about an axis perpendicular to the grating lines) is the least sensitive and is the best way to remove the zero-order reflection from the test beam. In-plane rotation (about an axis parallel to the grating lines) introduces coma. This alignment is critical; 1/20° misalignment will introduce 0.8λ of coma. The clock-angle alignment of the test surface is even more sensitive than the grating alignment. A misalignment of the cylinder axis relative to the grating lines introduces astigmatism. 1/20° clock-angle misalignment will introduce 2λ of astigmatism. Astigmatism and coma can still be present even if all the surfaces are perfectly aligned. Astigmatism may be present if there is a cylinder error in the test surface, and an imperfect grating can easily introduce coma.

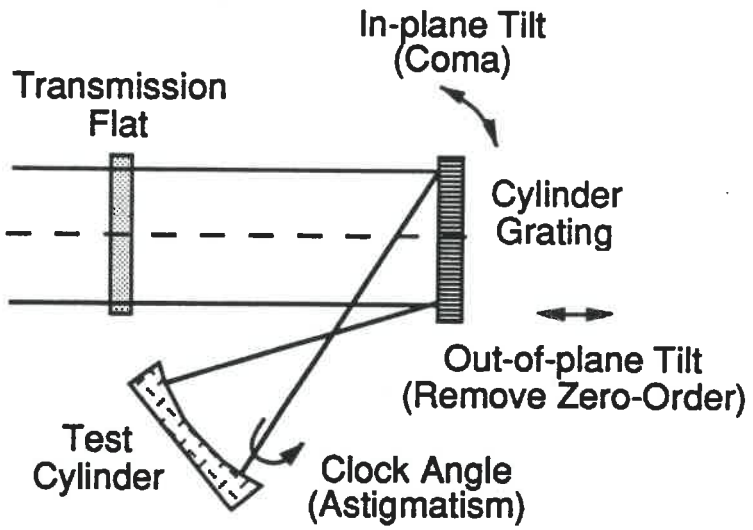

Figure 3. Cylinder testing alignment degrees of freedom.

To minimize alignment errors, the angular orientations of the optics in the test beam must be carefully adjusted. After the transmission flat is aligned relative to the interferometer, the grating needs to be aligned relative to the reference surface. The grating is then rotated out-of-plane to remove the zero-order reflection. Next, the test surface is aligned relative to the grating. The clock angle can be adjusted by rotating the cylinder to minimize the astigmatism in the measurement. Because the diffraction efficiency of the grating will not be perfect, the test surface will probably need to be coated to provide high contrast fringes.

The quality of the grating can be measured by placing a flat at the focus of the first diffracted order. However, it should be noted that this flips the beam so that the measured wavefront error is magnified. Errors in grating line spacing and variations in diffraction efficiency across the grating are evident in this test. The grating should have an error less than $\lambda/10$ to provide a reasonable test. Errors in the measurement due to the grating can be subtracted from the measurement using techniques developed for the absolute testing of spherical surfaces.

References

1. George Hirst, "Method and Apparatus for Optically Testing Cylindrical Surfaces," U. S. Patent #4606640 (August 19, 1986).

AN INTERFEROMETER FOR ASPHERIC TESTING: CALIBRATION AND ERROR COMPENSATION

Steven M. Arnold

APA Optics, Inc.
2950 N.E. 84th Lane, Minneapolis, Minnesota 55434

EXTENDED ABSTRACT

APA Optics has developed a phase measuring interferometer for testing of general aspherics using electron-beam written computer generated holograms as null compensators. Aspheric departures of up to several hundred waves are measured using only standard accessories; deeper aspheres may be tested using simple auxiliary optics.

The interferometer configuration is depicted in the figure below and has been described more completely elsewhere [1]. It is a Twyman-Green interferometer which uses polarization optics to separate the test and reference paths. The test beam is reflected by a first beamsplitter cube, enters the test arm, and returns through a 150-mm travel afocal telecentric relay system which images the test optic onto a 20-mm diameter computer generated hologram (CGH) located just after the second beamsplitter cube. Meanwhile, the collimated reference beam is transmitted by the first beamsplitter cube and undergoes four reflections by the second beamsplitter cube and the two reference mirrors before striking the CGH at an off-axis angle. The test beam and the diffracted reference beam form a nominally null interferogram which is spatially filtered and reimaged onto a diffuser glass by an afocal telescope. The image on the diffuser is then viewed by a video camera and zoom optics.

Because of 8 reflections and 8 double-pass air-glass interfaces unique to either the test or reference paths, the interferometer is not expected to achieve diffraction-limited performance without error compensation. Our approach has been to incorporate the system error compensation into the design of each CGH null compensator. In this manner, we can compensate known imperfections of the interferometer and accessory optics while presenting the user with a nominally null interferogram.

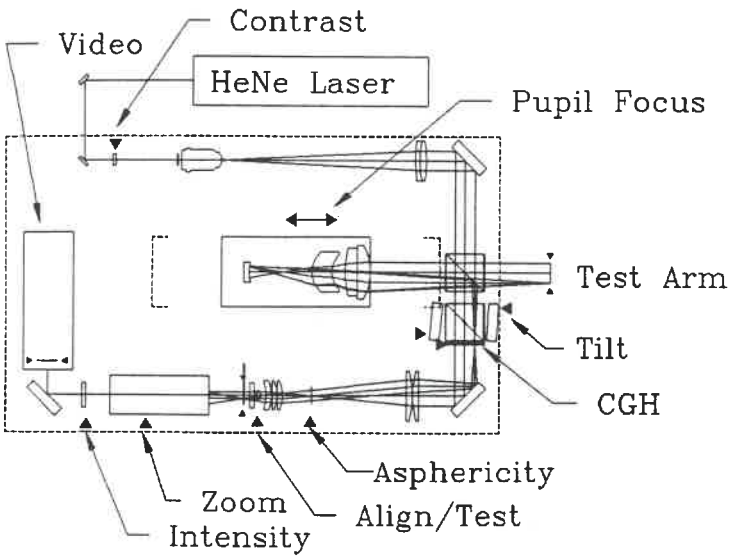

Several measures have been taken to assure that the interferometer alignment remains invariant from source arm pinhole to CGH. The front of the interferometer includes a kinematic bayonet mount for the attachment of various accessories. The removable CGH null compensator is also mounted kinematically. The laser collimator and the pupil relay optics are both designed to remain focused through a range of temperature. The positions of the pupil relay slide and the reference mirror tilt are displayed to the user and are to be set per the CGH design data. The optics following the CGH are common to both test and reference paths and therefore do not influence a null interferogram.

Calibration of the instrument is accomplished by attaching test fixtures to the accessory bayonet mount and inserting corresponding CGHs. The three test fixtures consist of a 500 mm radius concave mirror, a 500 mm radius convex mirror, and a variable tilt plano mirror. We find it useful to express the tilt angle of the plano mirror as an interferogram spatial frequency at the CGH (lpmm $= 2\,\lambda^{-1}\sin\theta$). Each fixture can be mounted to the bayonet in three orientations differing by 120 degree increments. The plano fixture alone samples the entire range of possible rayslopes over the full CGH aperture. The concave and convex fixtures provide a sensitive measure of centration and some redundancy.

The 13 calibration CGHs are of three types. The concave and convex configurations use off-axis CGHs with a carrier frequency of 300 lpmm. The tilted plano configurations use triple crossed binary gratings comprised of equilateral triangles. These CGHs work for all three bayonet orientations and no off-axis carrier is required since the test beam is itself tilted. A third CGH group consists of 7 linear gratings used to map the reference beam path with the untilted plano fixture in the test beam.

The figure below shows the expected interferograms resulting from the 18 test arm configurations. The leftmost column includes the concave, convex, and untilted plano

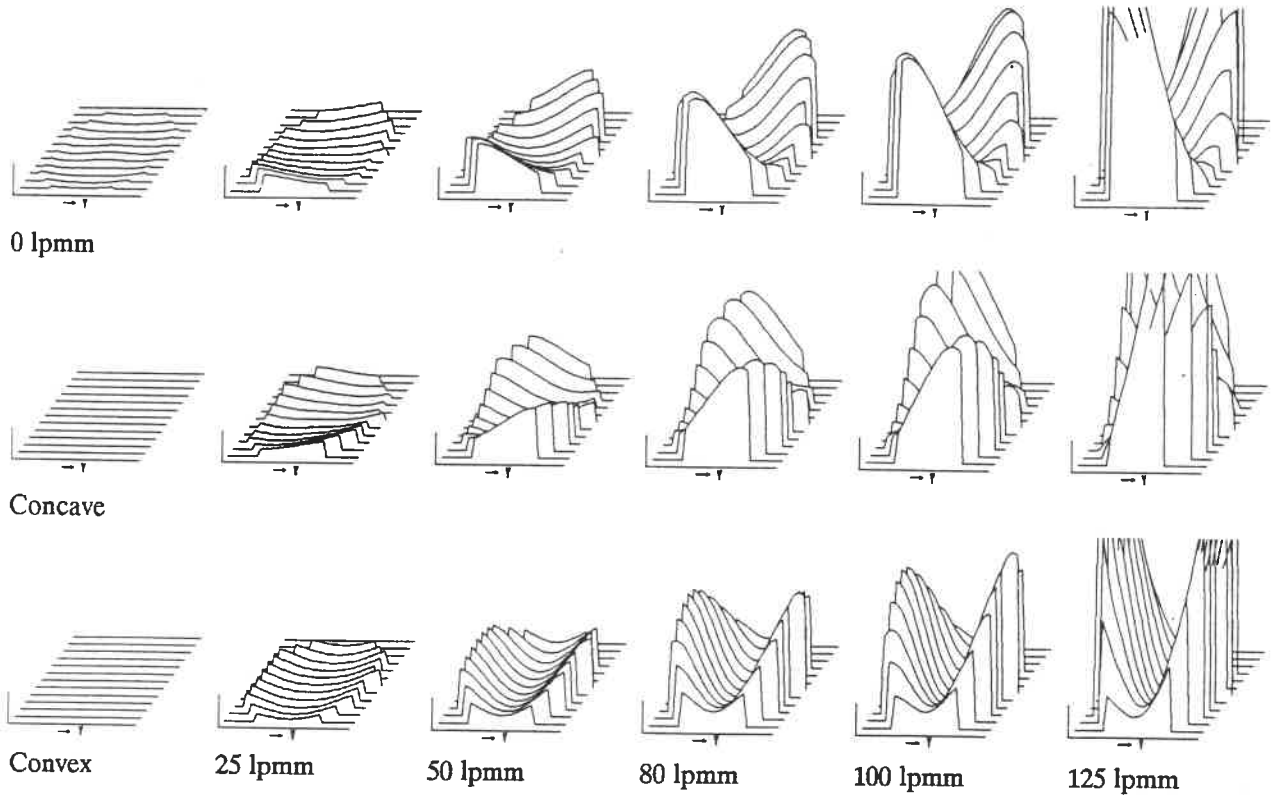

configurations. Additional columns represent increasing plano tilts of 25, 50, 80, 100 and 125 lpmm with each row being a different bayonet orientation (0, 120 and 240 degrees). The vertical scale is indicated by a bar representing two waves of OPD. The hardware calibration process consists of recording these 18+7 phase measured interferograms along with the system serial number and a date stamp. The process is simple enough to be performed in the field.

The flowchart diagram outlines the complete hardware and software calibration processes. After the 18+7 calibration interferograms are recorded to floppy disk, the data is ported to the OSLO raytrace program so that reverse optimization may be used to deduce the imperfections in the actual interferometer.

The WYKO DOS/RTI® software package is used to fit the interferogram data with 36 Zernike polynomials and a stand-alone program then converts the Zernike coefficients to an OSLO® diffractive surface (type DFX) described by a polynomial in x and y. This multi-configuration diffractive surface, located just after and coincident with the CGH phase function, acts to collimate the observed inteferogram wavefronts. Separate raytrace models are maintained for the test and reference paths. With the Zernike representation, we have effectively 18×36 = 648 optimization targets for the test path model and 7×36 = 252 optimization targets for the reference path model. Orthogonal Zernike polynomials are well suited to describing the expected decentering, tilting, focusing, and radius errors [2]. A 6-ring and 6-spoke rayset is now used, although we expect to identify a better rayset over which the Zernike polynomials are orthogonal [3]. The optimization operands then consist of OPD maps for each test configuration. Operands are inversely weighted by rayslope.

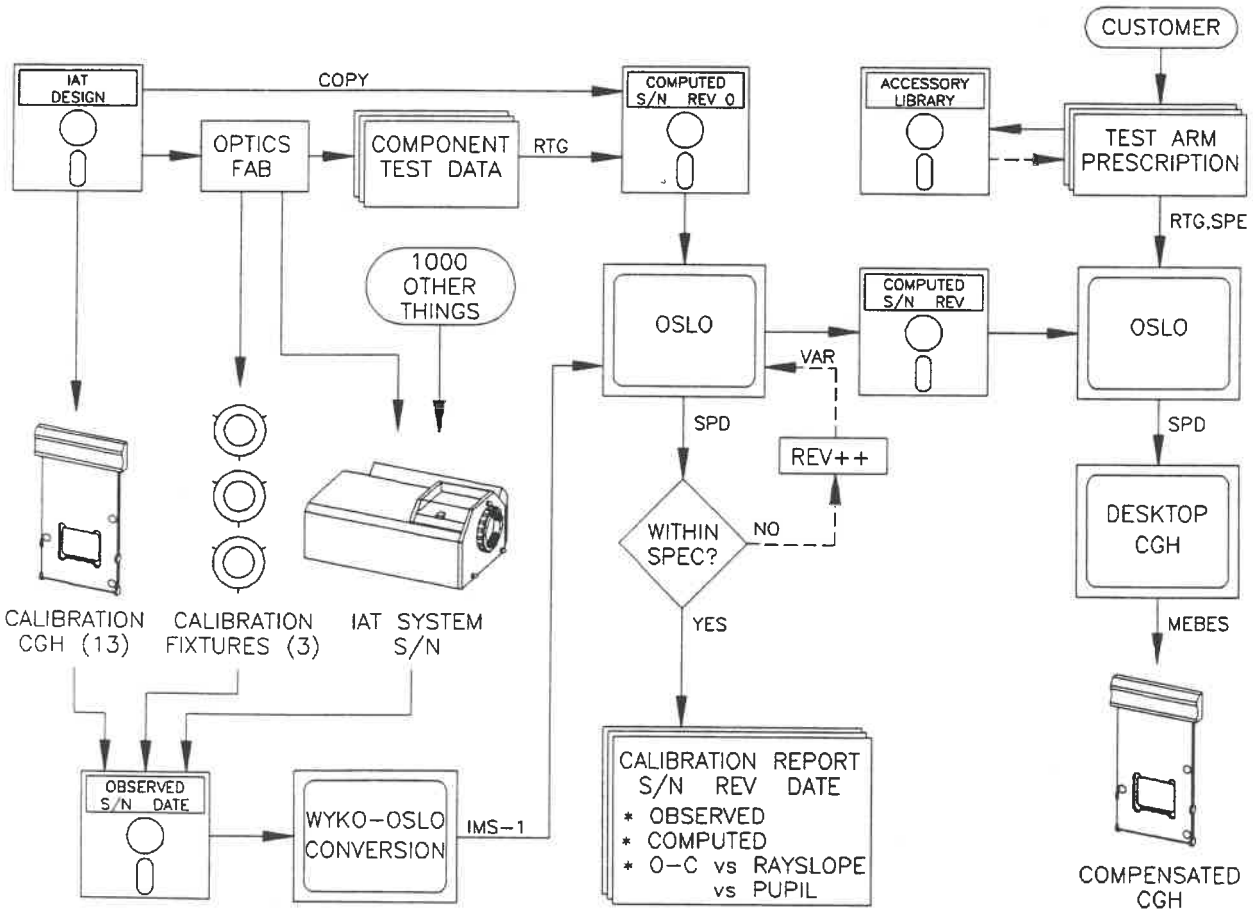

A question could be raised as to which optimization variables are legitimate. Clearly the 5 discrete tilt settings of the plano calibration fixture are valid optimization variables. Other key variables include the relative orientations of the bayonet, the test arm relay, and the CGH mount with respect to the optical axis (18 variables). Collimator and test relay focus are 2 additional variables. Decenter of the smaller half of the test relay doublet and tilt, decenter and airspace of the meniscus add another 7 variables. We therefore have at least 32 legitimate parameters. Some parameters will act as compensators for others, so the solution obtained may not be unique.

Another modeling approach is to sidestep questions of what constitutes a legitimate parameter and instead use whatever ad-hoc model best reproduces the observed interferogram data with a reasonable number of free parameters. This is what we have done with the reference path which has only a one-dimensional space of accessible configurations (*i.e.* tilt). For the test path, we have thus far opted for a strictly physical raytrace model in order to better understand the hardware. However, we would claim that the test arm space is sufficiently sampled by the 18 test configurations to justify the insertion of one or more fictitious phase surfaces if these are found to significantly reduce the residuals.

Accessory optics such as diverger lenses and an afocal beam expanding telescope are similarly modeled by recording their double-pass interferograms versus field angle. This requires no special CGHs or fixturing and can be accomplished using a conventional Fizeau interferometer.

Two principle outcomes of the interferometer calibration process are: 1) a report detailing the residual system error versus pupil coordinate and versus rayslope, and 2) a raytrace model which can be used in designing CGH null compensators.

We plan to present initial calibration data from one of our interferometers.

REFERENCES

1. S.M. Arnold and A.K. Jain, "An interferometer for testing of general aspherics using computer generated holograms", SPIE Vol. **1396** (1990).

2. B. Dörband and H. J. Tiziani, "Testing aspheric surfaces with computer-generated holograms: analysis of adjustment and shape errors", Appl. Opt. **24**(16), 2604-2611 (1985).

3. D. Malacara, J.M. Carpio-Valadéz and J.J. Sánchez-Modragón, "Wavefront fitting with discrete orthogonal polynomials in a unit radius circle", Optical Engineering **29**(6), 672-675 (1990).

Aspects of Scale Encoders Based on Grating Interferometer Technology

Arnold Teimel
DR. JOHANNES HEIDENHAIN GmbH
D-8225 Traunreut (Germany)

1. Introduction

Increasing requirements on the positioning accuracy of precision equipment in recent years, such as for the production of optical surfaces or in semiconductor technology, have resulted in a stronger demand for scale encoders with resolutions in the sub-micrometer range.

The accuracy of He-Ne laser interferometers is determined to a large extent by the accuracy with which the refractive index of air can be determined [1], [3]. A mathematical compensation, such as the Edlén formula, is often utilized [4]. Despite the sophisticated sensor equipment used, measuring accuracy is often unsatisfactory.

Scale encoders offer the advantage of a stable measuring standard with known thermal behavior. Due to the good repeatability systematic errors can be corrected by scale calibration. By appropriate selection of the scale carrier material, the thermal expansion coefficient can be optimized for individual applications. The measuring uncertainty due to insufficient accuracy of the temperature measurement can thus be significantly reduced.

Due to diffraction effects the grating period of conventional photoelectric encoders is limited to about 10 µm. With grating interferometers, these diffraction phenomena - particularly the phase shift of a diffracted light wave on a scale grating moving relative to the light source - are used for generating the measuring signal. This allows relatively large scanning gaps and gap tolerances as well as grating periods of less than 10 µm.

2. Operating Principle of Grating Interferometers

While He-Ne laser interferometers generate the measured value by interference of a working beam of variable length and a reference beam of constant length and by evaluation of the phase difference between these two beams, grating interferometers produce the measured value by the interference of two light beams diffracted on the scale grating, and subsequent evaluation of the phase difference.

For a relative displacement x between a scale with the grating period g and the diffracted beam, the phase shift Ω of the order of diffraction k is determined by the following equation:

$$\Omega = \frac{k \cdot 2\pi \cdot x}{g} \qquad (2.1)$$

It should be noticed that the wavelength of the light source has no influence on the phase shift.

The interference signal is produced by superimposing two diffracted wave trains. If the full amplitudes of the two waves are set to 1, the complex amplitude of the sum of the two waves is given by

$$U = U_1 + U_2 = e^{i\Omega_1} + e^{i\Omega_2}. \qquad (2.2)$$

For $\Omega = \Omega_1 = -\Omega_2$ the intensity is derived by the conjugated complex multiplication of the sum of the amplitudes:

$$I = U \cdot U^* = 2(1 + \cos 2\Omega). \qquad (2.3)$$

For a relative movement between the scale grating and the diffracted beam of one grating period, interference of the +1st with the -1st order of diffraction (fig. 1) creates two signal periods. If the second orders of diffraction were superimposed, there would even be four signal periods per grating period.

By selection of the orders of diffraction which are made to interfere the ratio of the phase grating period to the period of the interference signal can be varied. Since the intensity of diffraction decreases rapidly with increasing order k, in practice this is limited to order numbers $k \leq 3$. Another possible method for reducing the period of the interference signal is multiple diffraction at the scale grating. The phase shifts resulting from each diffraction can then be added.

The generation of the phase-shifted signal necessary for the recognition of direction and for interpolation can be achieved by means of a specially-dimensioned phase grating, or - using polarized, monochromatic illumination - by means of optical polarizing elements.

The scales with phase grating required for grating interferometers can be manufactured lithographically or holographically. One advantage of lithographically manufactured scales is the feasibility of longer measuring lengths, while holographically manufactured scales are limited to less than 250 mm due to stringent requirements on the optical equipment.

3. Grating Interferometers with Coherent Light Sources

A coherent light source allows simple optical configurations of grating interferometers. The acceptably-priced laser diodes which have recently become available on the market have given new impulses to the development of interferometric encoders.

These semiconductor lasers can be devided into multi-mode and single-mode types. Typical coherence lengths are 100 to 300 µm for multi-mode laser diodes but may reach up to several meters for single-mode laser diodes under certain operating conditions. Despite their longer coherence length, which allows larger manufacturing and mounting tolerances, single-mode laser diodes are less suitable for use in grating interferometers because of their discontinous wavelength-temperature characteristics. The center wavelength of the emission spectrum of laser diodes is dependent on temperature and operating current. A change of the laser diode temperature or current therefore causes measurement errors if the optical pathes of the interfering diffraction orders differ in length.

Interferential encoders using laser diodes as light source are being offered now. The grating periods are usually very small (1 to 2 µm), so that the desired order of diffraction can easily be isolated for generation of the interference signal. The modulation signals are thus free of higher-order harmonics and can be utilized for interpolation. Signal periods of 400 nm and below and resolutions down to 1 nm have already been realized over measuring lengths of 100 to 200 mm.

4. Grating Interferometers with Incoherent and Nonpolarized Light Sources

There are, however, grating interferometer configurations which can be realized with a simple light-emitting diode as light source. In this case the difference between the optical paths of the interfering wave trains must be kept within a few micrometers. An example of this is the interferential encoder LIP from HEIDENHAIN described below. The encoder consists of a steel scale (glass or ZERODUR scales are also available), with a reflection-type phase grating. Scales with 8 µm and 4 µm grating periods are produced. The grating consists of rectangular steps with a height of approximately 0.2 µm, alternating with gaps of the same width. The entire grating structure is produced by vapor deposition of chromium (DIADUR) and is thus very hard and wear-resistant. The scanning signals are generated in a scanning head which contains a transmitted-light phase grating (index grating) with the same grating period as the scale, an LED as light source, a condenser and three solar cells (fig. 1a).

The optical configuration of the grating interferometer is depicted in fig. 1b, greatly simplified but with the beam paths

shown "unfolded". The light source, the condenser and the solar cells are not shown. The plane wave produced by the LED and the collimator as well as the refracted waves are represented by light beams perpendicular to the wave front. A plane wave of wavelength λ is assumed, which falls perpendicularly onto the index grating.

The interaction of the illustrated components will now be explained. While passing through index grating G_1, the wave is mainly diffracted in the three directions -1, 0 and +1. The index grating is designed such that the phase of the beam of the

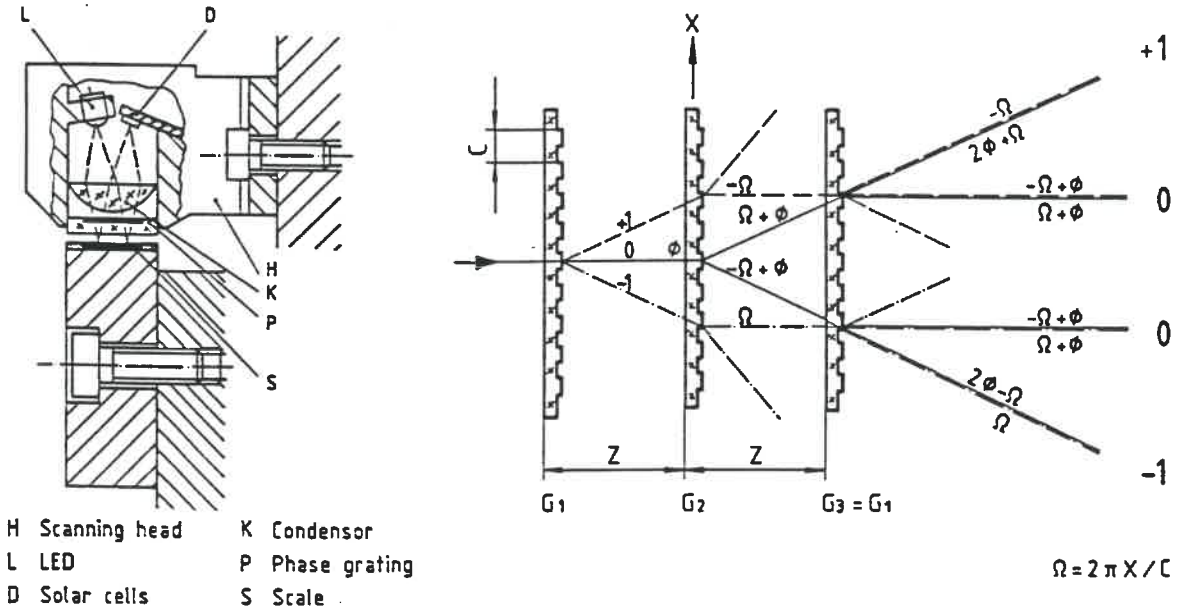

Fig. 1: Linear Encoder LIP 101 (HEIDENHAIN) - Left: design scheme; right: operating principle

zero order lag the beams of the ± 1st order by the amount Φ. As the beams strike the scale G_2, they are each diffracted in two directions of the order ±1. The scale is designed such that no zero order diffraction exists. When the scale is moved relative to grating 1 (= grating 3), the beams of the +1st (k = +1) order diffracted on the scale are phase-shifted - proportional to the displacement x - by the amount Ω, while the beams of the -1st order (k = -1) are phase- shifted by the amount $-\Omega$.

While passing through grating G_3, the light waves are diffracted and phase-shifted again. Waves of the same direction and the same optical path length interfere. The phases of the interfering waves result from the sum of the phase shifts of the individual beams. With illumination by non-monochromatic and spatially incoherent light sources, only the interfering waves in the direction +1, 0, -1 contribute to formation of the signal.

At the output of the grating system in the direction indicated by +1, a wave with phase $-\Omega$ interferes with a wave with the phase $2\Phi + \Omega$.

If the full amplitude of the waves is set to 1, the resulting complex amplitude U of the sum of both waves is

$$U = e^{-i\Omega} + e^{i(2\Phi+\Omega)}. \qquad (4.1)$$

The intensity is derived from conjugated complex multiplication of the amplitudes:

$$J_1 = U \cdot U^* = 2\,[1 + \cos(2\Omega + 2\Phi)]. \qquad (4.2)$$

For the direction indicated by 0, waves of the phases $-\Omega + \Phi$ and $\Omega + \Phi$ interfere.

The resulting intensity is

$$J_0 = 4\cos^2\Omega = 2\,(1 + \cos 2\Omega). \qquad (4.3)$$

Similar considerations lead to the intensity for the direction -1:

$$J_{-1} = 2\,[1 + \cos\,(2\Omega - 2\Phi)]. \qquad (4.4)$$

The intensities of these three interference signals are in each case detected in the focal plane of the collimator by the corresponding solar cell.

Movement of the scale (G_2) causes formation of signals with a period of g/2 which are phase-shifted to each other by 2Φ. A phase shift 2Φ of 120° has proven suitable. This is attained through the geometric configuration of the index grating G_1 and G_3 [3]. The three solar cells transform the phase and modulation of the interference signal into equivalent currents from which two sinusoidal output signals phase shifted with respect to each other by 90° are derived by an interface electronics. The amplitude and the 90° phase shift of the scale/scanning head system are individually adjusted in the interface electronics.

What advantages does this measuring system offer?
The strict symmetry of the optical path lengths prevents shifts of the LED emission spectrum by aging or temperature-dependent variations from influencing measurement. Thus the encoder is ready for use immediately after switch-on.

The length of the scanning field which contributes to the measurement signal of approximately 1500 grating periods assures reliable operation of the encoder, even if the scale is locally contaminated. The phase detected by the solar cells corresponds to the mean value of the phase of the waves which are diffracted over the entire length of the scanning field. Minor fluctuations

of the scale grating period are thus filtered out by integration over the length of the scanning field. The integrating effect and the short paths in air, from the splitting into various orders of diffraction to interference at the index grating, which amounts to only 1 to 2 mm, are important factors in the stability of the measuring signal. Resolutions of 10 nm for an encoder with an 8 µm grating period or 5 nm with a 4 µm grating period are thus entirely reasonable.

The arrangement of the system as reflected light grating encoder allows relatively large mounting tolerances since the distances G_2G_1 and G_2G_3 are always equal (fig. 1b).

The scales are presently produced with an 8 µm grating period in lengths up to approximately 1000 mm and with a 4 µm grating period up to 220 mm.

Figure 2 shows the interferential encoder LIP 101 R with a steel scale which has an 8 µm grating period and is furnished with a reference mark. After power interruption the position can be reproduced within one measuring step by means of this reference mark. Figure 3 shows a calibration chart of such a system. The total error is less than ± 0.2 µm for a measuring length of 420 mm.

Based on this technology also high precision rotary encoders and devices for 2D-measurement have been realized and will be discussed in the presentation.

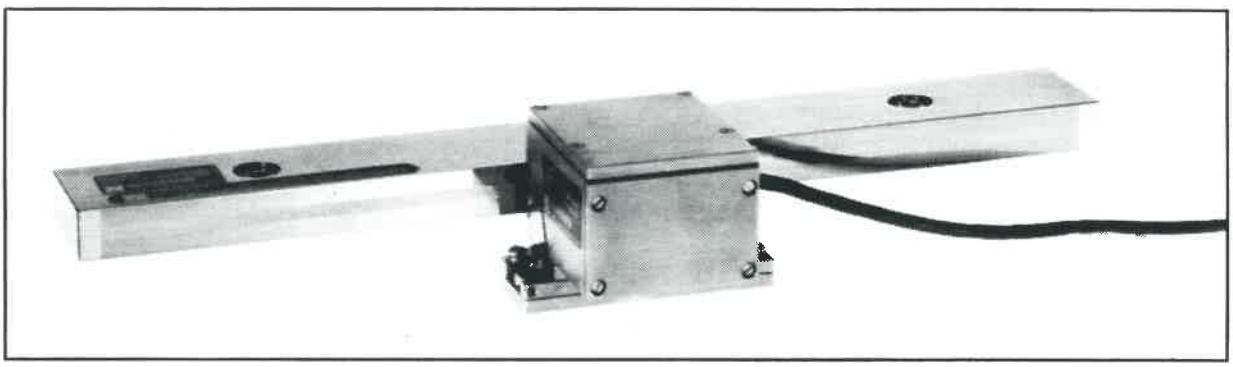

Fig. 2: Interferential Linear Encoder LIP 101R (HEIDENHAIN) with steel scale, grating period 8 µm and reference mark.

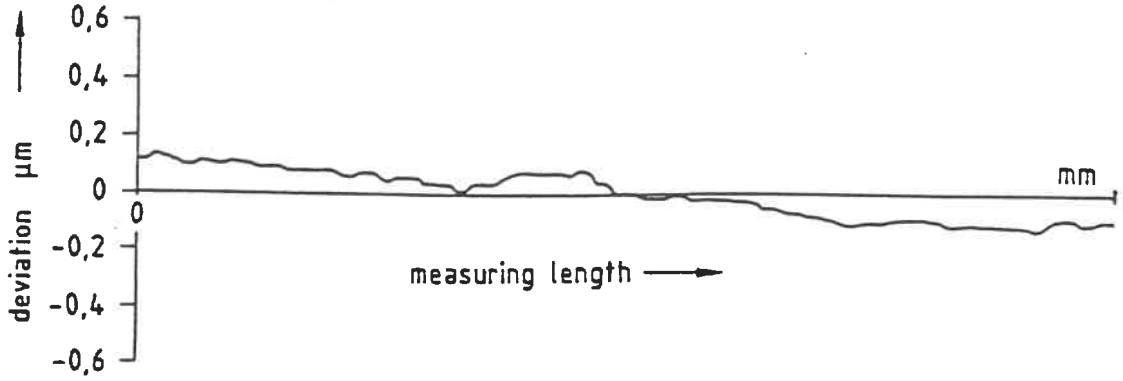

Fig. 3: Calibration chart of an interferential linear encoder, measuring length 420 mm, reference temperature 20.0° C.
(Reference: laser interferometer in vacuum)

Literature:

[1] **C.R. Steinmetz:** Sub-micron position measurement and control on precision machine tools with laser interferometry. Precision Engineering January 1990.

[2] **Alfons Spies:** Längen in der Ultrapräzisionstechnik messen. Feinwerktechnik & Meßtechnik 98 (1990).

[3] **W. Tyler Estler:** High-accuracy displacement interferometry in air. Applied Optics 24, No. 6 (March 1985)

[4] **Edlén, B.:** The refractive index of air. Metrologia 2 (1966), 71-80.

PRECISION MEASUREMENT OF PARTICLE SIZE USING BRIGHT FIELD INTERFEROMETRY

J. S. Batchelder, M. A. Taubenblatt
T. J. Watson Research Center
IBM Research Division
Yorktown Heights, NY 10598

Introduction

Contamination particles less than a micron in diameter are the single largest yield loss in semiconductor manufacturing. Instruments to detect and size these particles have traditionally utilized darkfield light scattering. Because of deficiencies in these instruments, such as mistaking bubbles for particles and sizing drift from light scattered from the flow cell windows, we have developed a technology that measures the phase shift and extinction of a focused laser beam due to light scattering in the forward direction by particles[1, 2]. This technology utilizes brightfield interferometry, and is embodied today in a commercial sensor from TSI Inc. that is employed in a number of manufacturing lines. The design of the sensor is basically a Nomarski-like transmission microscope such that the fluid of interest flows parallel to and within a Rayleigh range of the plane of focus.

Interferometry with Focused Beams

The instrument described above determines the size of sub-wavelength particles by measuring the phase shift and extinction induced in a focused laser beam. It succeeds in accurate (sub-nanometer) measurement of individual particles in part because the optical system produces more information that just a peak phase shift. Since chances are that liquid born particles will not pass exactly through the center of the plane of focus, it is necessary to determine the particle's trajectory from the details of the observed signals before determining the particle's size. Combining information from the entire trajectory plus analysis of the behavior of a beam near focus allows trajectory corrections to be made to the observed signals to correct for the variations due to off-axis and out-of-focus trajectories. The technique also becomes a sensitive test of the Gaussian beam formalism near focus.

At first glance the technique would appear to be inoperable, because the light emitted from very small scatterers (dipoles) is in phase with the exciting field, producing no net phase shift in the sum of the transmitted and scattered field. The phase shift signal occurs because of the extra phase retardation that occurs in a focused beam, known as the Gouy shift[3]. A focused beam undergoes an extra phase retardation of $\pi/2$ from the incident side of focus to the focal plane, and again from the focal plane to the far side of focus. A particle placed at focus radiates a spherical wave in phase with the incident field at that point. But, in the far-field, the outgoing incident field has lost $\pi/2$ in phase over the spherical wave from the particle originating at focus. Since the the incident wave (which in the far field has a spherical wave front) and the scattered wave from the particle are in quadrature, a phase shift is produced.

The Gouy shift may be understood as arising from the phase difference between a geometrical ray passing through focus (identical to a plane wave) and that of the diffracted wavefront, which traverses a shorter phase path and gives rise to the finite beam waist at focus[4]. It is a property of all wave-like focused beams. It is mathematically evident, however in the paraxial equations for a focused gaussian beam (i.e. a TEM_{00} laser beam). The field of a gaussian beam is given by[5]

$$E(r, z) = \frac{\omega_o}{\omega(z)} \exp\left[- r^2/\omega^2(z) - i \tan^{-1}(z/z_r) + ikr^2/2R(z)\right] \exp[ikz] \qquad (1)$$

where $\omega^2(z) = \omega_o^2(1 + z^2/z_r^2)$, $R(z) = z(1 + z_r^2/z^2)$, $\omega_o = \lambda/\pi(\mathrm{NA})$, $z_r = \lambda n/\pi(\mathrm{NA})^2$, and r, z are distances from the optical axis and the focal plane respectively. The beam has a plane wave phase dependence (exp [ikz]) modified by a gaussian amplitude factor, the $\tan^{-1}$ term arising from the Gouy shift, and a term accounting for the curvature of the beam. The phase shift is

due to the $-\pi/2$ factor arising from the behavior of $\tan^{-1}(z/z_r)$ between z = 0 and z = ∞. When the particle trajectory is out of focus ($z \neq 0$) and/or off-axis ($r \neq 0$) then the other terms must be taken into account in order to correctly derive the particle size by first determining its trajectory and correcting for it. This will be discussed in detail below.

The nature of a focused beam also has consequences for the more conventional use of interferometry to measure distances[6, 7]. Near focus the $\tan^{-1}$ term can be approximated by z/z_r, and has the effect of modifying the effective wavelength of the laser employed. In addition, since the beam has a radial curvature, if the entire beam is detected (rather than just r = 0) then this effect must also be taken into account. This has been calculated to be[7]:

$$k_{eff} = k - \frac{\lambda}{2\omega_o^2}\left[1 + \frac{\mu_o}{\exp(\mu_o) - 1}\right] \tag{2}$$

where $\mu_o = 2r_o^2/\omega_o^2$ and r_o is the detector aperture. The effective fractional change is wavelength is then given by $\lambda^2/4\pi^2\omega_o^2 = (NA^2)/4$, where NA is the numerical aperture of the optical system. For a weakly focused beam (100μm diameter, at 0.6328 μm wavelength) with full beam detection, this amounts to a wavelength correction of one part in 250,000, while for a more strongly focused beam (1 μm) this amounts to one part in 100.

Trajectory correction

As shown in Fig. 1, the sensor is composed of two parallel orthogonally polarized beams that are focussed in the flow cell. The emerging light is merged into a single beam (which is circularly polarized in the absence of a particle) and is subsequently split twice. The first non-polarizing beam splitter directs about half the light to a Wollaston oriented to mix the light from the two beams at two detectors, and the other half of the light to a different Wollaston that measures the individual transmissions of the two beams at a second two detectors. The difference between the first two sensors creates the differential phase signal; the difference between the the second two sensors creates the differential extinction signal. If a particle of diameter a and refractive index n is placed in a gaussian beam with a numerical aperture, NA, and a wavenumber k, the complex phase shift, ϕ produced on the beam by a particle at (x, y, z) is[1, 2]:

$$\phi = \left(\frac{NA}{m}\right)^2 \frac{S\omega_0}{\omega(z_r)} \exp\left[\frac{i\pi}{2} + i\tan^{-1}\left(\frac{z}{z_r}\right) - \left(i\frac{z}{z_r} + 1\right)\frac{r^2}{\omega^2(z_r)}\right] \tag{3}$$

where the laser propagates from -z to z, the focus of the beam is at the origin, the ratio of the complex index of the particle to the liquid is *m*, S is the is the Mie scattering matrix function in the forward direction[8], $S = S_1(0^\circ) = S_2(0^\circ)$. The real part of ϕ corresponds to the phase shift and the imaginary part to the extinction. From the above equation the differential phase and extinction signals for a particle in the two beam system can be computed.

There are several possible orientations of the optical beams with respect to the flow direction of the fluid. Having the two optical axis lie along the same flow line has the unfortunate result that in-focus signals from the same size particles have a constant shape as the off-axis distance increases, though the peak phase shifts and extinction signals decrease; there is no information to indicate that off-axis trajectories are causing particle sizing errors. The right geometry is to displace one optical axis from the flow line that intersects the other optical axis by a distance compatible with the signal to noise of the measurement (about a third of a beam waist the in sensors we designed) so that particles that are off-axis will have asymmetrical waveforms. Based on the Gaussian beam relations described earlier, off-axis correction look-up tables are calculated ahead of time that indicate the likely trajectories of particles as a function of their observed asymmetry. These tables also allow the observed peak heights to be corrected.

In a similar manner we can correct the signals for the distance the particle's trajectory had from the plane of focus. The temporal spacing between the peaks is determined by the flow

velocity if the peaks are separated by considerably more than a beam waist. As the trajectory becomes more out of focus, the widths of the individual peaks becomes larger with respect to the spacing between the peaks. The relationship between the widths and the spacing between the peaks then establishes the out of focus distance.

Experimental results

We will first show the sensor qualification data that demonstrates the sensor's accuracy and long term stability. We then will show results from simultaneous measurements of phase and extinction of individual particles, allowing the complex refractive index of an individual particle to be estimated along with its size. We will end with an estimate of the accuracy and resolution that next generation sensors based on this technique should be able to achieve.

References

[1] J. S. Batchelder and M. A. Taubenblatt, "Interferometric Detection of Forward Scattered Light from Small Particles," Appl. Phys. Lett. **55**, 215 (1989).

[2] M. A. Taubenblatt and J. S. Batchelder, "Measurement of the Size and Refractive Index of a Small Particle using the Complex Forward-Scattered Electromagnetic Field," Appl. Opt. **30**, 4972 (1991).

[3] A. E. Siegman, *Lasers*, (University Science Books, 1986).

[4] R. W. Boyd, "Intuitive Explanation of the Phase Anomaly of Focused Light Beams," J. Opt. Soc. Am. **70**, 877 (1979).

[5] A. Yariv, *Quantum Electronics*, (John Wiley and Sons Inc., 1975).

[6] N. Bobroff, private communication.

[7] J. P. Monchalin, M. J. Kelly, J. E. Thomas, N. A. Kurnit, A. Szöke, F. Zernike, P. H. Lee, and A. Javan, "Accurate Laser Wavelength Measurement with a Precision two-beam scanning Michelson Interferometer," Appl. Opt. **20**, 736 (1981).

[8] C. F. Bohren and D. R. Huffman, *Absorption and Scattering of Light by Small Particles*, (John Wiley and Sons, New York, 1983).

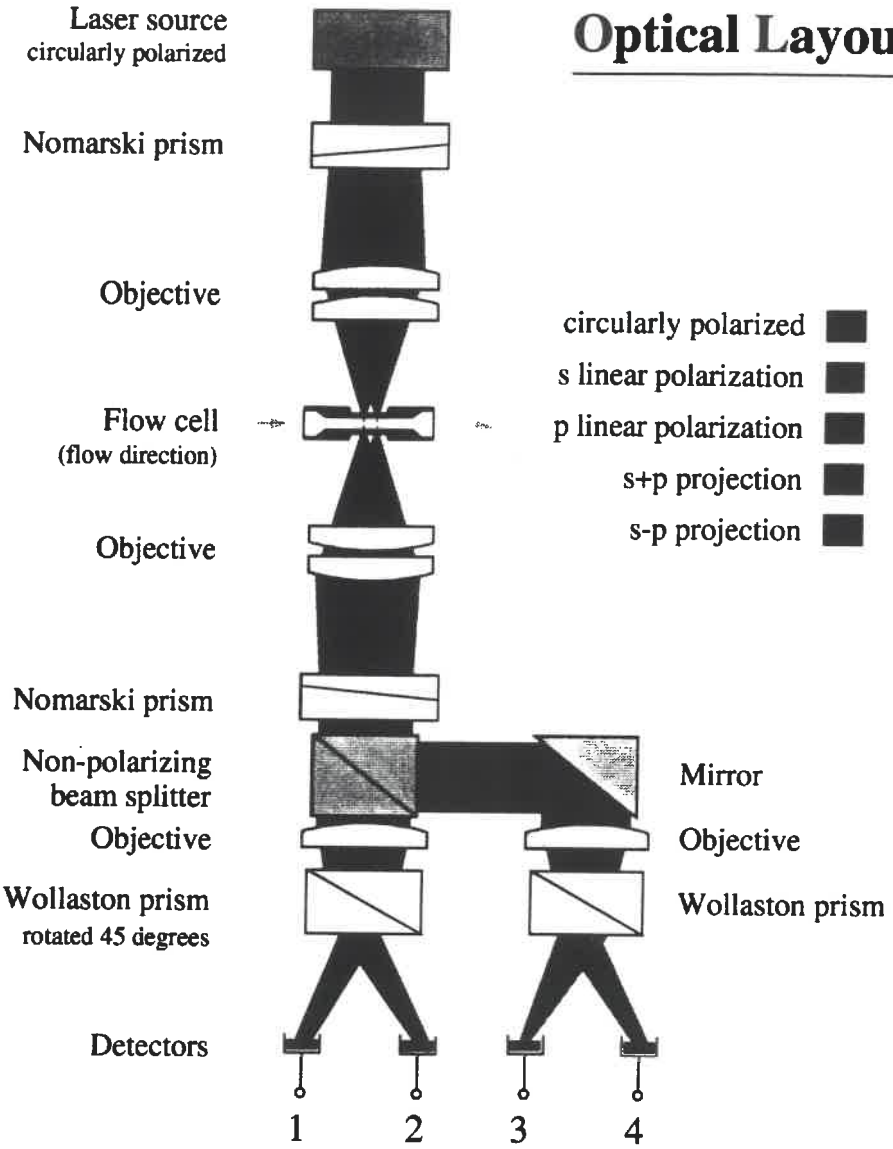

Figure 1. Optical diagram for a bright-field interferometer for the sizing of particles in liquids The instrument measures both the phase shift and extinction of a focused laser beam due to a particle passing through the beam.

Authors Index

Arnold, S. M. 83
Augustyn, W. 53
Batchelder, J. S. 94
Blum, J. D. 31
Buckman, A. B. 18, 22
Burge, J. H. 72
Creath, K. 80
Davis, P. 53
Elings, V. B. 11
Estler, W. T. ..... *
Evans, C. J. ..... *
Ferrara, C. F. 31, 35
Field, A. H. 40
Gee, A. E. 61
Gershman, M. 35
Giulianelli, L. C. 22
Grosso, R. P. ..... *
Hercher, M. 27
Kessler, Jr., E. G. 49
Martin, H. M. 72
Maxey, L. C. 65
Meiling, J. A. 7
Parks, R. E. 76
Rodgers, M. R. 11
Sebring, T. A. 35
Seltzer, A. J. 18
Shao, L-Z. 76
Shao, M. 5
Stejskal, A. 57
Stone, J. A. 57
Teimel, A. 87
Taubenblatt, M. A. 94
Tyrone, Jr., B. H. 18
Wang, C. P. 14
West, S. C. 72
Wilkening, G. 44
Wyant, J. C. 80
Wyntjes, G. 27
Youden, D. 35
Zernike, F. ..... *
Zushan, S. 57
Zweig, D. A. 68

*Paper not available at press time.